PALEOREGOLITH AND UNCONFORMITY-TYPE URANIUM MINERALIZATION AT BEAVERLODGE LAKE, GREAT BEAR MAGMATIC ZONE, NORTHWEST TERRITORIES

A Thesis Submitted to the College of Graduate Studies and Research in Partial Fulfillment of the Requirements for the Degree of Masters of Science in the Department of Geological Sciences
University of Saskatchewan
Saskatoon, Saskatchewan, Canada

By: PAUL H. SHAKOTKO

PERMISSION TO USE

In presenting this thesis in partial fulfillment of the requirements for a Postgraduate degree from the University of Saskatchewan, I agree that the Libraries of this University may make it freely available for inspection, I further agree that permission for copying of this thesis in any manner, in whole or in part, for scholarly purposes may be granted by the professor or professors who my thesis work in their absence, by the Head of the Department or the Dean of the College in which my thesis was done. It is understood that any copying or publication use of this thesis or parts thereof for financial gain shall not be allowed with my written permission. It is also understand that due recognition shall be given to me and to the University of Saskatchewan in any scholarly use which may be made of any material in my thesis. Requests for permission to copy or to make use of material in this thesis in whole or part should be addressed to:

Head of the Department of Geological Sciences
University of Saskatchewan
114 Science Place
Saskatoon, Saskatchewan S7N 5E2
Canada

OR

Dean
College of Graduate Studies and Research
University of Saskatchewan
107 Administration Place
Saskatoon, Saskatchewan S7N 5A2
Canada

ABSTRACT

During the Paleoproterozoic Era (ca. 2.5 Ga to 1.6 Ga), Earth underwent dramatic changes to its tectonic and atmospheric parameters. These changes included: the formation and breakup of the supercontinent Nuna (Columbia) and the gradual rise in atmospheric oxygen levels. The gradual rise in atmospheric oxygen, referred to as the Great Oxidation Event (GOE), altered the behaviour of silicate mineral weathering, and permitted the formation of new types of economic uranium deposits. Beaverlodge Lake, Northwest Territories (NT), allows for the study of a weathering profile and uranium mineralization post GOE.

At Beaverlodge Lake, NT, a regolith is preserved in a rhyodacitic porphyry of the ca. 1.93 Ga Hottah plutonic complex, which is unconformably overlain by the ca. 1.9 Ga quartz arenite of the Conjuror Bay Formation. Coincident with the unconformity is a past-producing uranium deposit (called the Tatie U deposit), which was mined out in the 1930s. Other uranium showings have been discovered at Beaverlodge Lake including the Bee showing. The initial purpose of this project was to examine the regolith through field, petrography, electron microprobe analysis (EMPA), whole-rock geochemistry, and mass balance calculations. The weathering profile shows an increase in Al_2O_3, $Fe_2O_3^T$, K_2O, P_2O_5, Ba, and Rb, a loss in SiO_2, Na_2O, MgO, and Sr, and constant and low abundance of CaO. Titanium remains constant in the weathering profile. Rare earth element (REE) analysis reveals remobilization of light REE (LREE) on a micrometer scale, but no cerium anomaly is preserved in the weathering profile. The weathering profile displays characteristics similar to other post GOE paleoweathering profiles developed on felsic parental material.

The timing of uranium mineralization at Tatie and Bee was constrained by in-situ U-Pb uraninite dating by Secondary Ion Mass Spectrometer (SIMS), which yielded two variably discordant ages of 1370.2 ± 7.9 Ma and 407 ± 21 Ma. In addition, REE contents of uraninite were determined by in-situ Laser Ablation Inductively Coupled Plasma Mass Spectrometry (LA-ICP-MS). Results revealed two types of uraninite mineralization are

preserved at Beaverlodge Lake and they consist of synmetamorphic at Bee and basement-hosted unconformity-type at Tatie similar to those in the Athabasca Basin. The ca. 1370 Ma uraninite (Tatie) is characterized by an asymmetric bell-shaped REE pattern centered on Tb to Er where LREEs are depleted compared to heavy REEs (HREE). The ca. 407 Ma uraninite at Bee has low La concentrations and a flat to slightly negative REE pattern. The Mesoproterozoic age is similar to a Pb loss age of ca. 1400 Ma found in the Athabasca Basin. The younger Devonian age may be related to meteoric fluids cycling and uranium remobilization during the Phanerozoic.

ACKNOWLEDGMENTS

TABLE OF CONTENTS

LIST OF FIGURES

x

LIST OF TABLES

LIST OF ABBREVIATIONS

Wt.%: weight percent
MSWD: Mean square weighted deviation
NT: Northwest Territories
GOE: Great Oxidation Event
Ga: Giga Annum or Billion years
Ma: Mega Annum or Million years
HFSE: High Field Strength Elements
μ: Micro
ε: Strain of an immobile element
τ: Mass transport coefficient of a mobile element
GBmz: Great Bear Magmatic Zone
WFZ: Wopmay Fault Zone
EMPA: Electron Microprobe Analysis
SIMS: Secondary Ion Mass Spectrometer
LA-ICP-MS: Laser ablation Inductively Coupled Plasma Mass Spectrometry
CIA: Chemical Index of Alteration
CIA – K: Chemical Index of Alteration minus Potassium
PIA: Plagioclase Index of Alteration
REE: Rare Earth Elements
LREE: Light Rare Earth Elements
HREE: Heavy Rare Earth Elements
IOCG (U): Iron-Oxide Copper Gold (Uranium)

CHAPTER 1
INTRODUCTION

The Paleoproterozoic Era (2.5 Ga to 1.6 Ga) was a time of profound change in Earth's evolution. These changes included shifts in the Earth's tectonic and atmospheric parameters. The assembly (ca. 2.1 Ga to 1.8 Ga) and eventual break-up (ca. 1.5 Ga to 1.4 Ga) of the supercontinent Nuna (Columbia) may represent the first complete supercontinent cycle (Zhao et al., 2002 and 2004). Following the assembly of Columbia, major orogenic events ceased and Columbia transitioned to a period of subduction-related growth via accretion along continental margins (Zhao et al., 2004). Assembly and growth allowed for the formation and preservation of large and economically important sedimentary basins such as the Athabasca and Thelon basins. The uranium deposits associated with these basins might not have formed if it were not for the rise in atmospheric oxygen during this time.

Rye and Holland (1998) were the first to suggest a gradual rise in atmospheric oxygen between ca. 2.5 and 1.9 Ga often referred to as the Great Oxidation Event (GOE). Rye and Holland (1998) studied fifteen definite paleosols (fossil soils) and observed that in paleosols prior to GOE, there was progressive loss of iron (Fe) going from unweathered parent to weathered equivalent. In profiles post-GOE, there is retention of Fe in the weathering profile. The oxidation of Fe^{2+} to Fe^{3+} allowed for the retention of Fe in weathering profiles. The timing of GOE at ca. 2.2 Ga, first estimated by Rye and Holland (1998), has been refined and is now understood to have occurred at ca. 2.4 Ga (Bekker et al., 2004; Holland, 2009). The underlying cause of GOE remains unknown; however, the preeminent theory suggests that the cause of GOE was due to the rise in photosynthetic organisms such as cyanobacteria. Another theory suggests that the depletion in oceanic nickel killed methane-producing organisms (methanogens), allowing for the emergence of photosynthetic organisms (Konhauser et al., 2009). Another theory suggests a gradual change in the composition of volcanic volatiles as responsible for GOE (Holland, 2002).

This rise in atmospheric oxygen allowed for the diversity in mineral species (e.g.

oxide minerals including uraninite: UO_2), which led to changes in the type of economic mineral deposits. Prior to GOE, uraninites were derived from magmatic processes (high Th) and U deposits were detrital in origin. For example, economic paleoplacer deposits such as Elliot Lake and Witwatersrand typically contain large tonnage and low-grade uranium resources (Hazen et al., 2009). After GOE, uranium, in the upper crustal environment, was able to oxidize from U^{4+} to U^{6+}, be transported in hydrothermal solutions as uranyl, and be deposited to form new economic deposits including vein-type, unconformity-type (Australia and Canada), and natural nuclear reactors (Gabon) (Hazen et al., 2009).

At Beaverlodge Lake, Northwest Territories (NT; not to be confused with Beaverlodge Lake in the Beaverlodge district in northern Saskatchewan), a recently identified unconformity under the 1.90 Ga Conjuror Bay Formation quartz arenite has been confirmed. Below the unconformity, a paleoregolith is preserved in a ca. 1.93 Ga rhyodacitic porphyry. Coincident with the unconformity is a past-producing uranium showing (called the Tatie showing) that was mined out in the 1930s. As such, Beaverlodge Lake, NT provides a natural laboratory to study a weathering profile and uranium mineralization post-GOE.

Beaverlodge Lake, NT is approximately 300 km northwest of Yellowknife and 150 km south of Port Radium. It is located on the western side of the Slave craton and comprises part of the larger Wopmay orogen. Previous work in the Beaverlodge Lake area was part of large-scale regional mapping programs and it has been mapped at various scales (Kidd, 1936; Henderson, 1949; McGlynn, 1979; Hildebrand and Roots, 1985; Jackson and Ootes, 2012). In addition, several geological reports regarding the uranium mineralization were generated with varying degrees of detail (Hargreaves, 1935; Henderson, 1949; Grady, 1955; Byrne and Smith, 1955; Baykal, 1967). Approximately 1.5 tonnes of U_3O_8 were extracted from the Beaverlodge Lake area at grades upwards of 50% (Henderson, 1949). A few of the reports allude to a possible unconformity at Beaverlodge Lake, but none reference the paleoregolith. It was not until mapping by Jackson and Ootes between 2009 and 2012 that the paleoregolith and unconformity were

2

recognized and confirmed. This MSc project was initiated to better understand the unconformity and its significance in the evolution of the Hottah Terrane and paleoweathering at ca. 1.9 Ga.

Purpose and Scope of the Project

The initial purpose of this project was to carry out a detailed study of the paleoregolith (paleosol) found at Beaverlodge Lake, NT through fieldwork, petrography, whole-rock geochemistry, and electron microprobe analysis (EMPA). As the project progressed, work was also undertaken to understand the uranium showings (Tatie and Bee) at Beaverlodge Lake. In addition to the above, Secondary Ion Mass Spectrometer (SIMS) and Laser Ablation Inductively Coupled Plasma Mass Spectrometry (LA-ICP-MS) were used to characterize uraninites from Tatie and Bee.

Research Objectives

Regarding the paleoregolith
- Determine the nature of alteration preserved in the paleoregolith.
- Compare the paleoregolith at Beaverlodge Lake to other Paleoproterozoic paleoregoliths developed on felsic parents as well as modern-day weathering profiles.
- Determine if the paleoregolith preserves any details about the state of atmospheric oxygen ca. 1.9 Ga.

Regarding the uranium showings
- Determine the type of uranium deposit preserved at Beaverlodge Lake: unconformity-type, IOCG (U), or something else.
- Compare the Tatie and Bee showings to other U showings in the Great Bear magmatic zone (GBmz).
- Compare the Tatie and Bee showings to world-class U deposits such as those in the Athabasca Basin.

Thesis Structure

       The two main chapters (Chapters 3 and 4) of this thesis were written as manuscripts intended for publication. The senior author is responsible for all the fieldwork, data analysis, and thesis preparation. Chapter 2 provides an overview of the regional geology of the Wopmay orogen and general stratigraphy of the Hottah Terrane and Great Bear magmatic zone. Dr. John Ketchum of the Northwest Territories Geoscience Office provided reviewer comments on Chapter 3. Chapter 4 has not yet been submitted as a manuscript. Chapter 5 is a brief summary of the conclusions from Chapters 3 and 4. References for both chapters 3 and 4 can be found at the end of Chapter 5, as there is extensive repetition between both chapters. Analytical appendices follow chapter 5 and include analytical techniques, whole-rock geochemistry, supporting data, and EMPA data. Both chapters deal with different subject matters; however, both share the same study area (Beaverlodge Lake, NT).

CHAPTER 2
REGIONAL GEOLOGY AND GREAT BEAR STRATIGRAPHY

Wopmay orogen

The Wopmay orogen is a Paleoproterozoic orogenic belt located on the western side of the Slave craton (Figure 2.1). The tectonic components of the Wopmay orogen from east to west include the Coronation margin and its Archean basement, the Wopmay Fault Zone (WFZ), the Great Bear magmatic zone (GBmz), and the Hottah Terrane. The Coronation margin is separated from the Hottah Terrane and GBmz by the WFZ. The WFZ corresponds to the eastern limit of the GBmz and the Hottah Terrane and western limit of the Archean Slave craton.

The Coronation Margin consists of 2.01 Ga rift-related Melville Group, 1.97 Ga passive margin-related Epworth Group, and 1.88 Ga foredeep-related Recluse Group (Hoffman et al., 2011). The Hottah Terrane consists of >1960 Ma metasupracrustal rocks and ca. 1.93-1.91 metaplutonic rocks that are unconformably overlain by the ca. 1.91-1.89 Ga Bell Island Bay Group (Reichenbach, 1991; Ootes et al., 2012). The youngest exposed part of the Hottah Terrane is the <1.88 Ga Treasure Lake Group (Gandhi and van Breemen, 2005). The GBmz is a calc-alkaline magmatic arc built on Hottah Terrane (Bowring and Grotzinger, 1992; Gandhi et al., 2001; Hildebrand et al., 2010a and b; Cook, 2011). It formed between 1.88 Ga and 1.85 Ga in response to eastward-dipping subduction and the eventual collision of Hottah Terrane with the western Slave craton (Bowring and Grotzinger, 1992; Gandhi et al., 2001; Hildebrand et al., 2010a and b; Cook, 2011). Two stages of magmatic activity have been recognized during the development of the Great Bear magmatic arc. The first stage consisted of volcanic rocks of the McTavish Supergroup, specifically the LaBine, Dumas, and Faber groups, which erupted between 1868 Ma and 1872 Ma (Bowring, 1984; Hildebrand et al., 1987; Goad et al., 2000; Gandhi et al., 2001; Hildebrand et al., 2010b; Ootes et al., 2012). The second stage consisted of extensive plutonism between 1855 Ma and 1866 Ma coincident with the eruption of the Sloan Group (Bowring, 1984; Gandhi et al., 2001; Bennett and Rivers, 2006; Ootes et al., 2012).

In the north, the Coppermine Homocline unconformably overlies the Wopmay orogen and is composed of sedimentary and volcanic rocks (Baragar and Donaldson, 1973). Part of the Coppermine Homocline is the Hornby Bay Basin, which consists of the Hornby Bay and Dismal Lakes groups. The Hornby Bay Basin is considered correlative to the Athabasca and Thelon basins and hosts the Mountain Lake U showing (Kerans et al., 1981; Ross, 1983; Rainbird et al., 1994; Irving et al., 2004). The Mountain Lake U showing is hosted in the quartz arenites and conglomerates of the LeRoux Formation and has been classified as sandstone-type (Bell, 1996). The timing of mineralization is poorly constrained. Davis et al. (2008) suggested an age of ca. 1284 Ma for the formation of apatite and xenotime cements, which formed approximately at the same time as the uranium. This age is similar to the 1270 Ma Mackenzie igneous event (Lecheminant and Heaman, 1989) that affected both the Athabasca and Thelon basins (Kotzer and Kyser, 1995; Renac et al., 2002). To the west, the Wopmay orogen is unconformably overlain by Paleozoic platformal strata (Ootes et al., 2013). It is likely that the Coppermine Homocline strata may occur under this platform (Ootes et al., 2013).
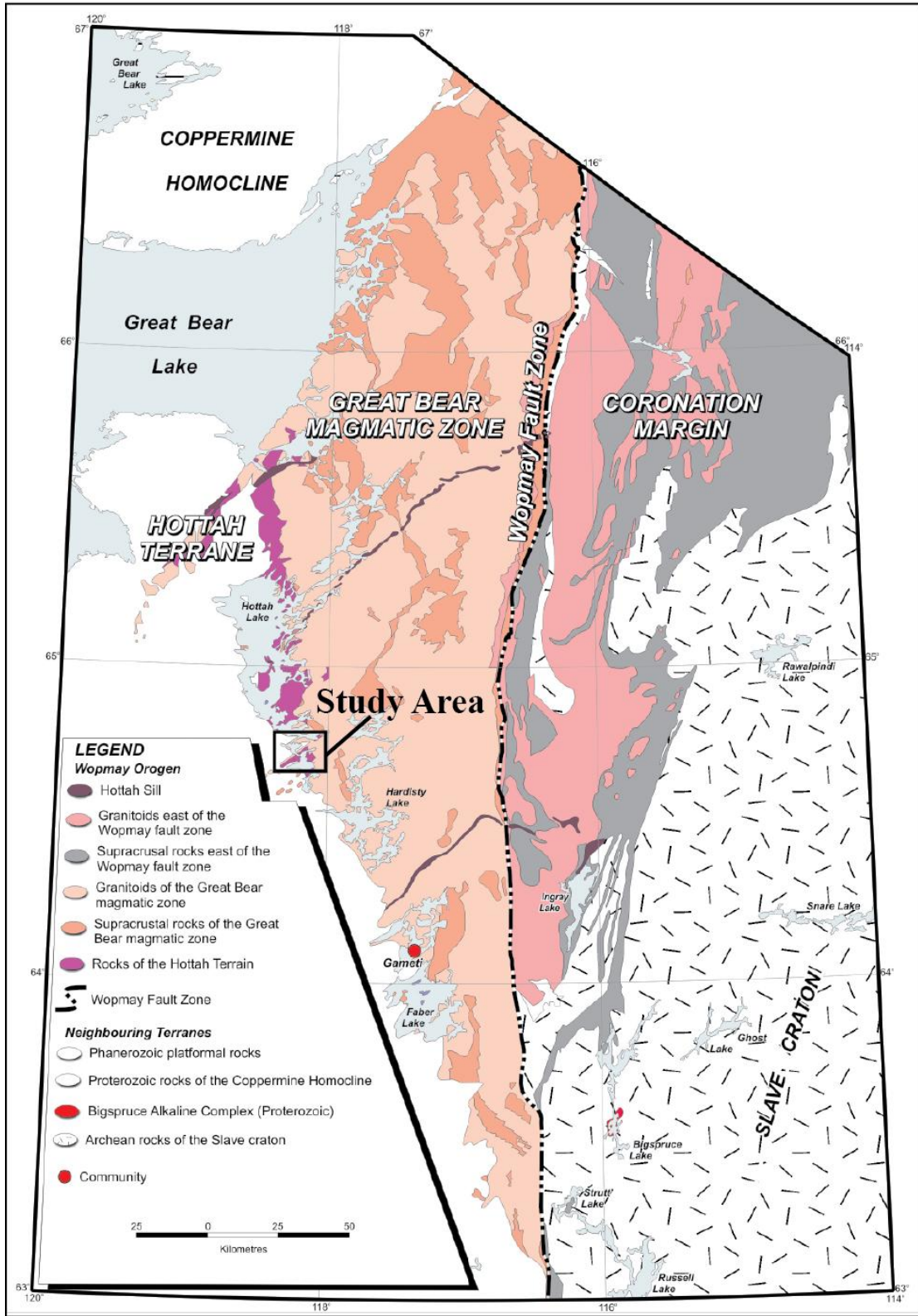
Figure 2.1 Regional map of the Wopmay orogen. The study area at Beaverlodge Lake is identified.

Hottah Terrane and Great Bear Stratigraphy

The oldest identified bedrock lithologies of the Hottah Terrane are the <1.97 Ga metapelites and metavolcanic rocks of the Holly Lake Metamorphic Complex (HLMC; Hildebrand et al., 1983; Hildebrand and Roots, 1985; Ootes et al., 2012). The HLMC was deformed and metamorphosed before or at ca. 1.93 Ga when it was intruded by granite, tonalite, and diorite of the ca. 1.91-1.93 Ga Hottah plutonic complex (Ootes et al., 2012). Exposure of the HLMC and Hottah granitoid rocks is not extensive, but where exposed, they are typically unconformably overlain by the Beaverlodge Lake sandstone, Zebulon Formation, or Conjuror Bay Formation of the Bell Island Bay Group (Reichenbach, 1991; Ootes et al., 2012). The Beaverlodge Lake sandstone is a fining-upward, basal conglomerate to sandstone with volcanic and granitic clasts (Reichenbach, 1991). The Zebulon Formation consists of ca. 1.905 Ga rhyolite, lesser basalt, and minor andesite. The Zebulon Formation is unconformably overlain by ca. 1.90 Ga (detrital zircon age) quartz arenite and overlying siltstone of the Conjuror Bay Formation (Reichenbach, 1991; Ootes et al., 2012). The Conjuror Bay Formation is intruded by Fishtrap gabbro dykes that fed overlying pillowed Bloom basalts (Reichenbach, 1991; Ootes et al., 2012). At a few localities, quartz arenite of the Conjuror Bay Formation directly overlies HLMC (such as at Conjuror Bay) or the Hottah plutonic complex (such as at Beaverlodge Lake, the location of this study).

The Treasure Lake Group is a sedimentary sequence that is assigned to the Hottah Terrane (Gandhi and van Breemen, 2005), although it is never observed in direct contact with the strata described above. The Treasure Lake Group is assigned to the Hottah Terrane as it was deformed and metamorphosed prior to the onset of ca. 1.87 Ga Great Bear volcanism (Goad et al., 2000; Gandhi and van Breemen, 2005). The volcanic rocks of the GBmz are assigned to the McTavish Supergroup and are subdivided according to their location (Hildebrand et al., 1987; Gandhi et al., 2001; Hildebrand et al., 2010; Ootes et al., 2012). Figure 2.2 summarizes the distribution of sequences west of the WFZ. Relevant to this study is the unconformity between the Hottah plutonic complex and overlying Conjuror Bay Formation quartz arenite at Beaverlodge Lake.
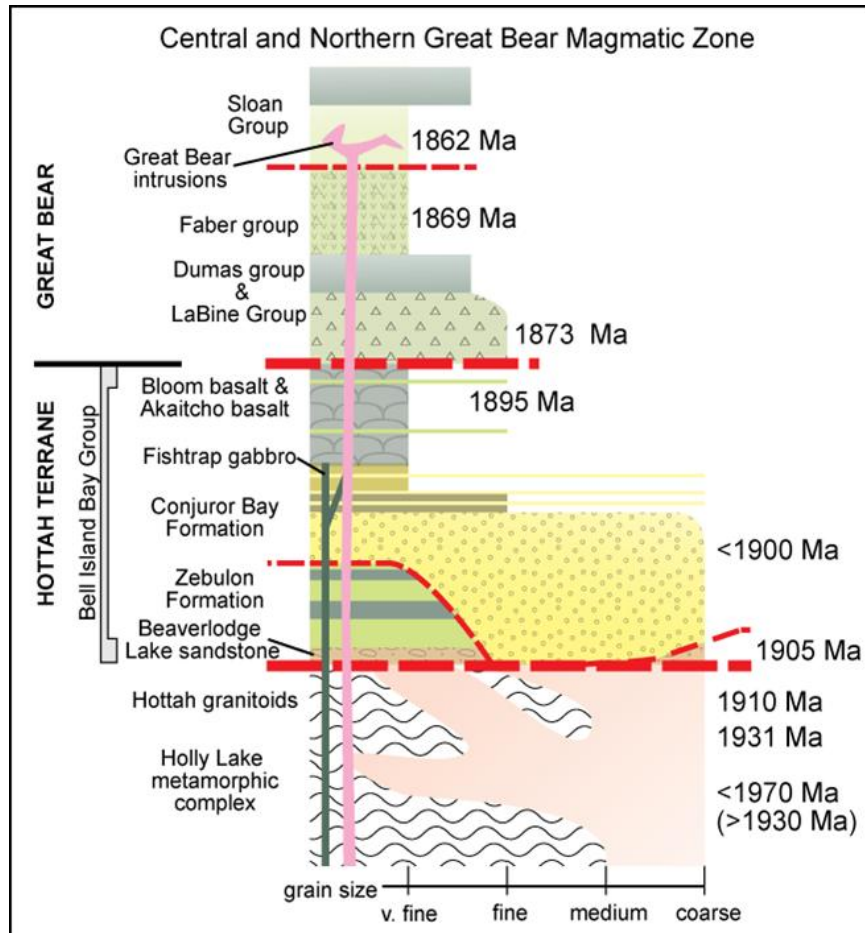
Figure 2.2 Simplified stratigraphy of the area west of the Wopmay Fault Zone (WFZ). This study is focused on the unconformity between the Conjuror Bay Formation and underlying Hottah plutonic complex. Red dashed lines indicate unconformities. The age data is from Bowring (1984), Reichenbach (1991), Gandhi et al., (2001), Gandhi and van Breemen (2005), and Ootes and Davis (unpublished data).

CHAPTER 3
A PORPHYRY – WEATHERED PORPHYRY – QUARTZ ARENITE SUCCESSION AT BEAVERLODGE LAKE, NORTHWEST TERRITORIES: MASS BALANCE APPROACH TO A PRECAMBRIAN REGOLITH

Chapter 3 "A Porphyry – Weathered Porphyry – Quartz Arenite Succession at Beaverlodge Lake, Northwest Territories: Mass Balance Approach to a Precambrian Regolith" provides a detailed study of the regolith at Beaverlodge Lake, NT. A combination of fieldwork, petrography, EMPA, and whole-rock geochemistry demonstrate, through mass balance calculations, that the Beaverlodge Lake regolith is similar to other regoliths developed on felsic parental material post-GOE. The research for the paper was conducted by the author with writing and editing assistance from Dr. Yuanming Pan and Luke Ootes. This paper will be published through the Northwest Territories Geoscience Office as an Open Report.

Abstract

Paleoweathering and alteration events are often preserved along unconformities. At Beaverlodge Lake, south of Great Bear Lake, NT, a regolith is preserved in a ca. 1930 Ma quartz-feldspar porphyry of rhyodacitic composition, which is unconformably overlain by a quartz arenite. Bedrock mapping, whole-rock geochemical analyses, and mass balance calculations have been undertaken to investigate the mobility of various elements during alteration. The following trends are observed: Al_2O_3, $Fe_2O_3{}^T$, K_2O, P_2O_5, Ba, and Rb increase going from least-altered parent to weathered equivalent; SiO_2, Na_2O, MgO, and Sr decrease; and CaO remains low and near constant throughout the weathering profile. Titanium remains constant. Uranium, Th, and Th/U also remain constant throughout the profile. There is also an increase in LREE going from least-altered parent to weathered equivalent. Presence of secondary monazite grains in and around fluorapatite grains suggests LREE remobilization occurs at least on a micrometer scale. Alteration indices maximum values of CIA = 77, CIA – K = 99, and PIA = 98 indicate advanced weathering during the formation of the Beaverlodge Lake regolith. This is consistent with tropical weathering conditions and is further supported by published paleomagnetic data.

In post-GOE weathering profiles, positive Ce anomalies are typically present in upper more oxidized soil zones of the weathering profile. The absence of a Ce anomaly in the Beaverlodge Lake regolith suggests removal of the upper oxidized soil zones by erosion. Absence of a Ce anomaly does not suggest low O_2 conditions during regolith formation as other regoliths approximately the same age as the Beaverlodge Lake regolith preserve positive Ce anomalies. Elevated levels of K_2O, observed in the geochemistry and in the partial to complete replacement of plagioclase and K-feldspar by sericite, are common in Precambrian paleosols and are best explained by late K-metasomatism, specifically diagenesis of overlying sediments. The timing of K-metasomatism of the Beaverlodge Lake regolith relative low-grade metamorphism is difficult to constrain.

Introduction

A Paleoproterozoic regolith was identified at Beaverlodge Lake, NT, while investigating a reported giant quartz vein occurrence and coincident uranium mineralization (Byron, 2010). This occurrence was further investigated during regional bedrock mapping of the Paleoproterozoic Wopmay orogen by Valerie Jackson and Luke Ootes between 2009 and 2012. The regolith is preserved in a 1.93 Ga rhyodacitic porphyry that is unconformably overlain by ca. 1.9 Ga (detrital zircon age) quartz arenite of the Conjuror Bay Formation. Coincident with the unconformity is a past-producing uranium occurrence, which was mined out in the 1930s. This project examines the altered porphyry through field and petrographic observations, electron microprobe analysis and whole-rock geochemistry with the following questions: What is the nature of the alteration being observed in the quartz-feldspar porphyry? How is the regolith at Beaverlodge Lake similar to other known Precambrian regoliths? What, if anything, can be said about atmospheric conditions at ca. 1.9 Ga?

Background

Previous work on regoliths

There is abundant scholarly work pertaining to regoliths and paleosols. Most paleoweathering studies are aimed at reconstructing the ancient atmosphere at the time of paleosol formation. The Beaverlodge Lake regolith preserved in a 1.93 Ga rhyodacite porphyry, post-dated GOE at ca. 2.4 Ga (Rye and Holland, 1998). In general, attention is given to regoliths that formed around 2.4 Ga and thereafter.

Rye and Holland (1998) were the first to suggest a change in the retention of Fe in Precambrian paleosols around 2.2 Ga. They noted that in soils older than ca. 2.2 Ga, Fe^{3+} was progressively lost going upward in the regolith profile from fresh parental material to weathered equivalents, whereas in soils younger than 2.1 Ga, Fe^{3+} was largely retained. They suggested the retention of Fe in these weathering profiles was due to a rise increase in atmospheric oxygen (pO^2) after 2.1 Ga. The increase in pO^2 is further supported by a concomitant change in the style of uranium deposits in the sedimentary record, a

transition from placer-type to unconformity- and roll-front-type ore (Retallack, 1990). Subsequent studies have placed GOE at an earlier time, around 2.4 Ga (Bekker et al., 2004; Holland, 2006).

The literature regarding Precambrian paleosols most typically describes the investigation of element mobility in basaltic parents, rather than felsic parents. For example, these include studies on the ca. 2.22 Ga Hekpoort paleosols (Rye and Holland, 2000) and on the ca. 1.85 Ga Flin Flon paleosols (Holland et al., 1989; Pan and Stauffer, 2000). Studies on felsic protoliths include on the ca. 2.5 Ga Ville Marie paleosol (Panahi et al., 2000) and on the ca. 2.45 Ga Pronto paleosol (Nedachi et al., 2005).

Near Ville Marie, Québec, a ca. 2.5 Ga granite is unconformably overlain by Paleoproterozoic sedimentary rocks of the Lorrain Formation (Panahi et al., 2000). The unconformity is estimated to have formed between ca. 2.38 to 2.21 Ga (Rye and Holland, 1998). The basement granite is a coarse-grained equigranular alkali biotite-granite. Geochemically, Na_2O, CaO, and Sr decrease in the profile from fresh granite to the saprolith due to the destruction plagioclase feldspar; TiO_2, Nb, Th, Zr, Hf, and Ta remained immobile during alteration; K_2O, Rb, and Ba were added by K-metasomatism after the granite was buried by sediments of the Lorrain Formation. With respect to rare earth elements (REE), the Ville Marie saprolith has $20 - 40\%$ lower concentration of REE in the saprolite than in the protolith, suggesting REE mobilization during pedogenesis (Panahi et al., 2000).

A second example of felsic igneous regoliths is the ca. 2.45 Ga Pronto paleosol near Elliot Lake, Ontario. Volcanic rocks of the Whiskey Lake Greenstone Belt are intruded by the 2.4 to 2.7 Ga "Algoman granites" and are unconformably overlain by Huronian sedimentary rocks. The Pronto paleosol is preserved in the "Algoman granites." Above the unconformity are uraniferous conglomerates of the Matinenda formation, the lowest formation of the Huronian Supergroup (Nedachi et al., 2005). In the regolith profile, TiO_2, Zr, and Hf remained immobile during soil formation; SiO_2, CaO, and Na_2O were lost and may correlate with the destruction of plagioclase feldspar, whereas MgO

and K_2O were enriched, most likely due to later metasomatism after deposition of the overlying Matinenda formation (Nedachi et al., 2005).

In northern and western Canada, the Proterozoic Athabasca and Thelon sedimentary basins have characteristics that are relevant to the present study. These basins also host some of the largest uranium deposits in the world. Regoliths, in both basins, are developed on heterogeneous parent materials, which are unconformably overlain by conglomerate to sandstone. The ca. 1.72 Ga Thelon Formation in the Thelon Basin has a paleosol that was developed on four different protoliths: granitoid gneiss, granite, pelitic gneiss, and semi-pelitic gneiss (Gall, 1994). Gall (1994) demonstrated that the mobility of major and trace elements differs amongst the various protoliths, but the general trends from fresh parent material through the paleosol to the unconformity include: 1) increased reddening of the paleosol due to hematization; 2) increased dissolution of feldspars due to the loss of CaO, Na_2O, K_2O, Ba, Sr, and Rb; and 3) an increase in the chemical index of alteration (CIA). The retention of Fe in the weathering profile and the increase in ferric iron-hematite support that the Thelon paleosol formed under oxidizing conditions (Gall, 1994).

Macdonald (1980) examined the regolith underlying the ca. 1.75 Ga Athabasca Formation (Raemakers et al., 2007) (at that time estimated at 1.51 Ga) in the Athabasca Basin and described four-colour zones: 1) bleached zone, 2) hematite zone, 3) white zone, and 4) green/red zone. These zones were thought to be equivalent to major horizons recognized in present-day laterites. The presence of a well-developed 1 to 5 metre thick red zone (oxidized horizon) in the sub-Athabasca regolith is consistent with a regolith that formed under oxidizing conditions.

Previous work around Beaverlodge Lake

On the north side of the east arm of Beaverlodge Lake, NT, there is a prominent 18-km long ridge with bedrock exposures of Hottah plutonic complex, overlying Zebulon Formation volcanic rocks, and Conjuror Bay Formation quartz arenite and overlying siltstone (Figure 3.1; Jackson and Ootes, 2012). Here, Conjuror Bay Formation

unconformably overlies both the Zebulon Formation and the older Hottah plutonic complex. Previous work in the Beaverlodge Lake area includes regional mapping programs at various scales (Kidd, 1936; Henderson, 1949; McGlynn, 1979; Hildebrand and Roots, 1985; Jackson and Ootes, 2012). Uranium was extracted from Beaverlodge ridge during the 1930s (called the Tatie occurrence; Henderson, 1949), likely for radium to be used in medicinal applications during that period. A number of mineral exploration reports have been generated for this area since the 1930s with a focus on uranium mineralization. A few of these reports allude to a possible unconformity, but it was not until reconnaissance work by L. Ootes, S. Gleeson, and S. Byron (Byron, 2010), who discovered a possible unconformity. This was followed by a field excursion (L. Ootes, V.A. Jackson, H. Sandeman, and S. Byron) to confirm the unconformity and led to SHRIMP U-Pb detrital zircon dating of the Conjuror Bay Formation quartz arenite in 2009 and CA-TIMS U-Pb zircon dating of the underlying porphyry in 2010 (L. Ootes and W.J. Davis, personal communication).
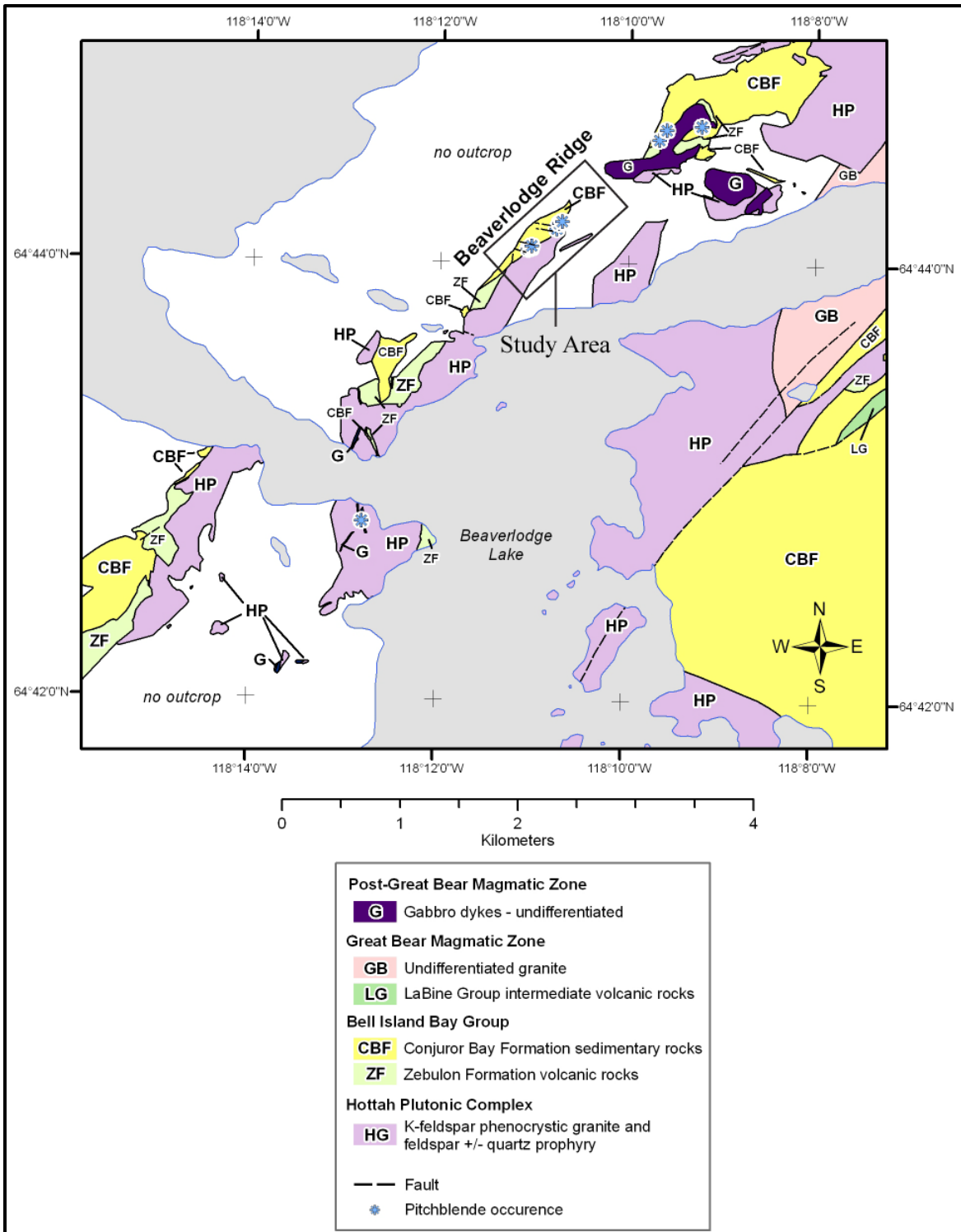
Figure 3.1 Distribution of sequences and uranium occurrences along Beaverlodge ridge. Modified after Henderson (1949), McGlynn (1979), Hildebrand and Roots (1985), and Jackson and Ootes (2012).

Local Geology

The senior author conducted a detailed field study in 2011 with follow-up in 2012. Five detailed traverses across 160 metres in total were completed with an average distance of 50 metres between traverses. Figure 3.2 provides a sketch of the regolith from the least-altered sample through the regolith to the unconformity with the quartz arenite of the Conjuror Bay Formation. The whole sequence has been overprinted by greenschist grade regional metamorphism. All five traverses yielded the same general features as one approaches the unconformity with the overlying quartz arenite.
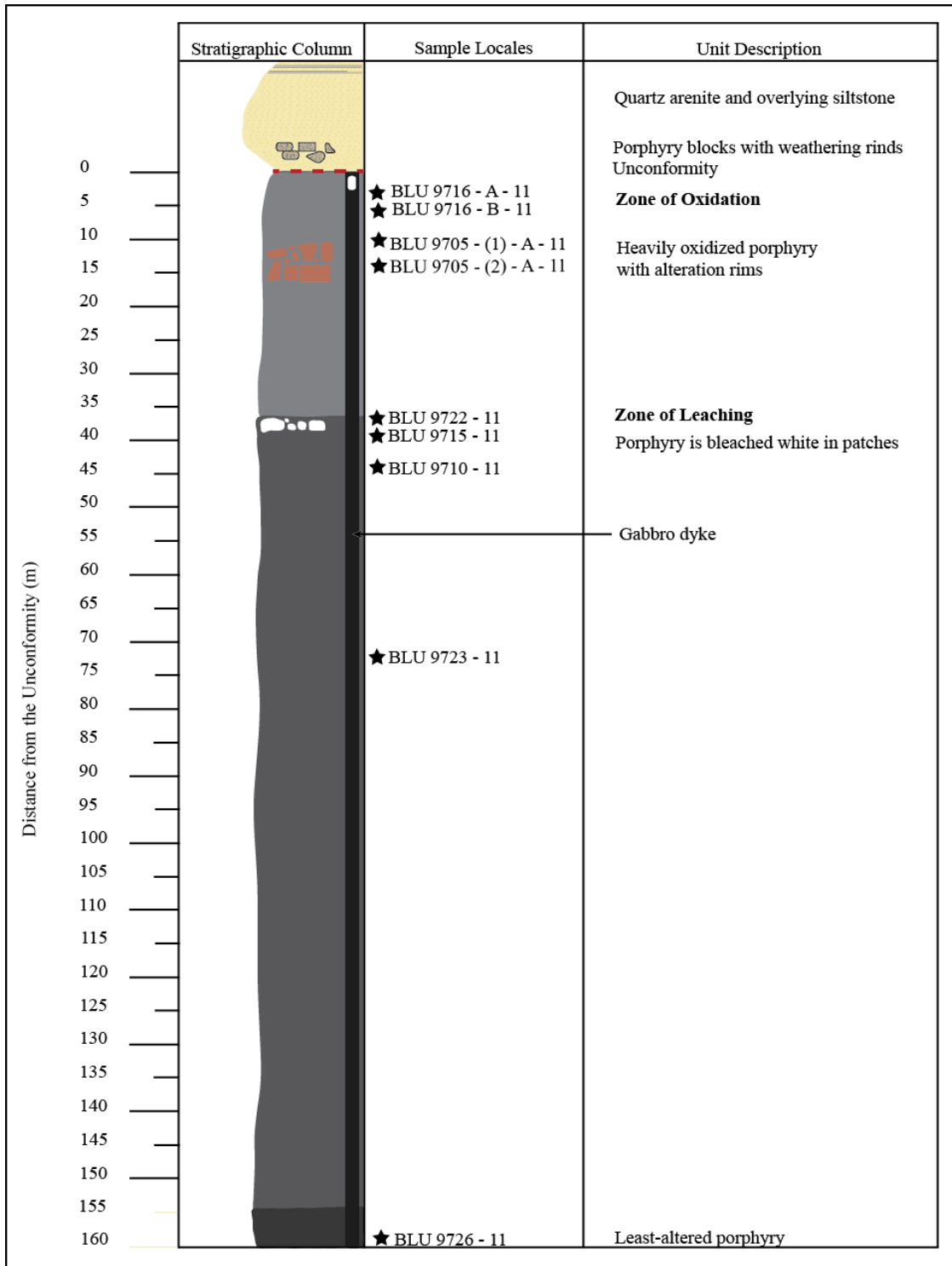
Figure 3.2 Schematic graphic log through the Beaverlodge ridge regolith.

At the base of Beaverlodge ridge, least-altered porphyry of the ca. 1.93 Ga Hottah plutonic complex has a dark gray to purple groundmass and contains phenocrysts of plagioclase feldspar and quartz (Figures 3.2 and 3.3.A). Up the ridge toward the unconformity, the porphyry becomes variably altered and appears fragmental. Overlying the least-altered porphyry is a "zone of leaching" where heavily altered porphyry appears to be bleached white in patches whereas areas adjacent to bleached porphyry remain dark gray to dark green (Figures 3.2 and 3.3.B). The bleached patches range in size from 2 to 15 cm. The adjacent porphyry is less altered but still heavily altered and is of similar composition to the bleached porphyry. Overlying the "zone of leaching" is a "zone of oxidation," where the heavily altered porphyry colour changes to salmon pink/orange in some places and the less altered but still heavily altered porphyry is light gray (Figures 3.2 and 3.3.C). The feldspar phenocrysts in the heavily altered porphyry have been altered to clay or weathered out. The less altered but still heavily altered porphyry adjacent to heavily altered porphyry is of similar composition to the heavily altered porphyry. The less altered but still heavily altered porphyry contains abundant hematite and chlorite. Several small quartz, hematite, and chlorite veins cut the heavily altered porphyry. Within a few metres of the unconformity in the "zone of oxidation," alteration rims were observed around the heavily altered porphyry (Figures 3.2 and 3.3.D). These heavily altered porphyry and alteration rims range in size from 4.5 to 60 cm. The alteration rims around heavily altered porphyry range between 1.5 and 3 cm. From the base of the ridge to the unconformity with the Conjuror Bay Formation, there is an overall increase in fracturing, hematite and clay alteration, and dissolution of feldspars. Overlying the "zone of oxidation" is a pure white quartz arenite of the Conjuror Bay Formation. The quartz arenite displays cross bedding and ripple marks. At the base of the Conjuror Bay Formation, porphyry clasts with weathering rinds are preserved (Figures 3.2 and 3.3.E). These clasts range in size from 10 to 35 cm and the weathering rinds are 0.5 mm to 1 cm thick. The porphyry clasts' angularity ranges from angular to sub-rounded. At the top of the ridge, quartz arenite is interbedded with siltstone and then gives way to predominantly siltstone.
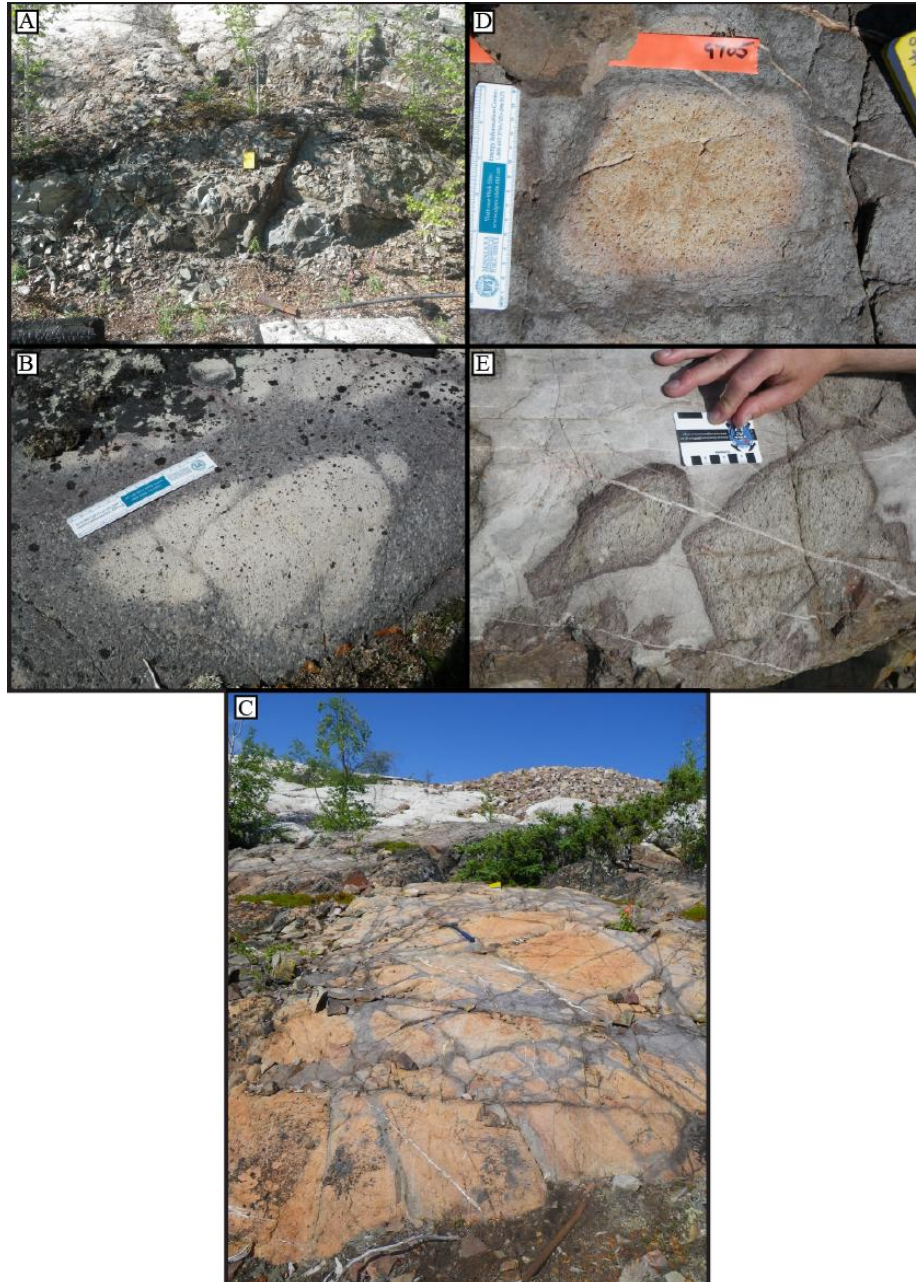
Figure 3.3 (A) Least-altered rhyodacite porphyry has a dark gray groundmass with phenocrysts of quartz and plagioclase feldspar at the base of Beaverlodge ridge. (B) Bleached porphyry in the zone of leaching. Porphyry is bleached white in patches and heavily altered. Adjacent to bleached porphyry is less altered but still heavily altered porphyry. (C) Heavily oxidized porphyry below the unconformity. Heavily altered porphyry is salmon pink to orange in patches and has abundant hematite. Adjacent to oxidized porphyry is less altered but still heavily altered porphyry. (D) Alteration rims around oxidized porphyry in the zone of oxidation. (E) Porphyry clasts with distinct weathering rinds at the base and within the quartz arenite.

20

<center>**Results**</center>

Petrography and Electron Microprobe Analysis

Thirteen samples exhibiting various states of alteration were examined petrographically and Table B.2 summarizes the observations. The sample assigned as the least-altered porphyry contains phenocrysts of quartz and plagioclase feldspar, with the latter showing minor sericite alteration (Figure B.2.A). The groundmass of the least-altered porphyry consists of K-feldspar (microcline), plagioclase feldspar, quartz, chlorite, and hematite (secondary). Minor amounts of late chlorite and quartz veins are also present in the least-altered sample.

No thin sections were made for samples collected from the "zone of leaching" therefore all geochemical profiles remove those samples, as there is no context. Plagioclase feldspar phenocrysts in the less altered but still heavily altered porphyry in the "zone of oxidation" are abundant, but are partly to completely replaced by sericite (Figure B.2.B). Plagioclase relicts are rarely preserved. The size of the relict plagioclase feldspar phenocrysts (approximately 3 mm) is similar to those found in the least-altered porphyry sample. The heavily altered porphyry from the "zone of oxidation" feldspar phenocrysts have been altered to clay minerals ± sericite (Figure B.2.D). Quartz phenocrysts appear unaltered (Figure B.2.C). Grain boundaries between phenocrysts and the surrounding groundmass are diffuse. The groundmass around the phenocrysts in this zone is entirely altered except for a few quartz grains. Where the groundmass is recognizable, it consists of altered alkali feldspars, plagioclase feldspars, and abundant chlorite and hematite. The destruction of alkali feldspars is not as severe as the destruction of the plagioclase phenocrysts. Ferromagnesian minerals have been completely destroyed and replaced by chlorite and oxides. Abundant late quartz and chlorite as well as secondary Fe-oxides veins occur. The alteration rims observed around the heavily altered porphyry in the "zone of oxidation" consist primarily of quartz.

Quartz arenite consists predominantly of detrital quartz grains with minor amounts of altered feldspars, sericite, hematite, chlorite, and zircon and is well sorted.

<center>21</center>

Quartz grain size ranges from 0.3 to 0.4 mm. In one sample, the quartz arenite is heavily fractured and filled with late quartz and hematite veins (Figure B.2.E). Porphyry clasts, within the base of the quartz arenite, have weathering rinds that consist of Fe-oxides, chlorite, and plagioclase feldspars phenocrysts that are completely replaced by sericite. The upper siltstone consists primarily of fine-grained quartz, sericite, and chlorite.

Several accessory minerals were identified in least-altered and most altered porphyry samples including Fe oxide, Fe-Ti oxides, fluorapatite, monazite, and zircon on the electron microprobe. The zircon crystals in the altered porphyry appeared to sub- to euhedral and remained intact during alteration (Figure 3.4.A) whereas Fe-Ti oxides have been partially replaced by chlorite (Figure 3.4.B). Fluorapatites displayed fine scale oscillatory zoning and appeared sub- to euhedral (Figure 3.4.B).

As described above, different rates of weathering were observed in the Beaverlodge regolith. Minerals such as plagioclase feldspar and Fe-Mg minerals were completely replaced by sericite and chlorite, respectively whereas minerals such as quartz, microcline (in the groundmass), and zircon remained relatively intact during alteration. The volume of the regolith therefore is equal to the sum of three components: volume of secondary minerals (sericite ± clay minerals), volume of resistant minerals (zircon and quartz), and volume due to porosity of the regolith (Velbel, 1990; Nahon, 1991; White, 1995). This suggests weathering of the Beaverlodge regolith occurred isovolumetrically therefore the volume of the regolith is equal to the volume of the least-altered sample. Isovolumetric weathering would result in the preservation of the rock's texture, structure, and fabric (Panahi et al., 2000). Because the porphyry's texture is preserved, it is interpreted that the volume of the Beaverlodge regolith has been maintained.
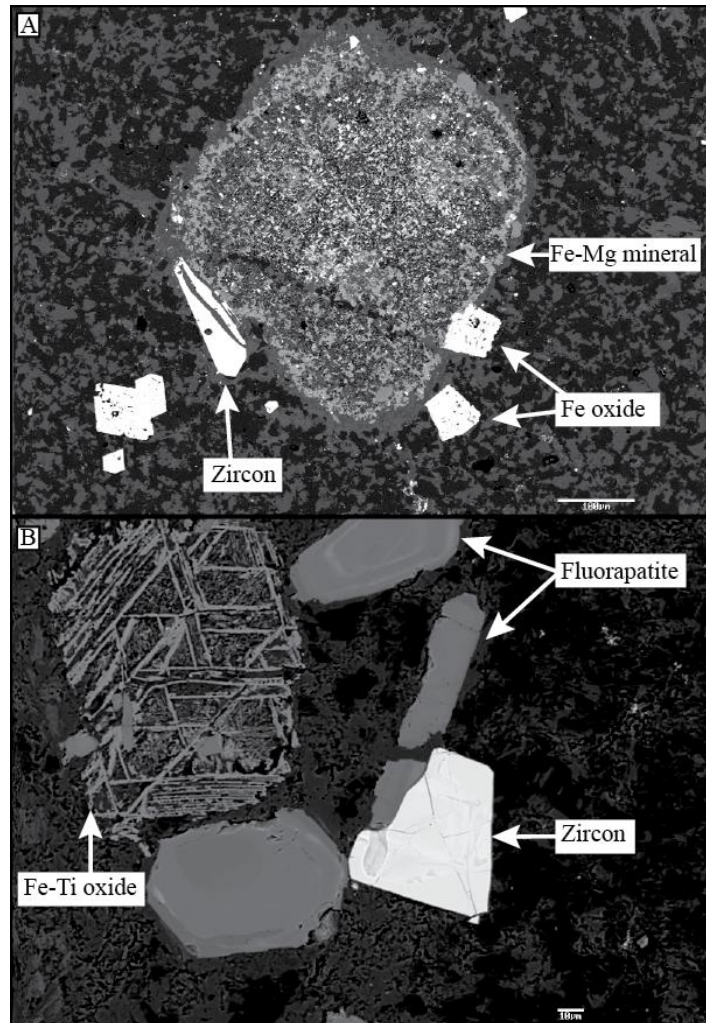
Figure 3.4 (A) Backscattered electron imaging of well-preserved, subhedral to euhedral zircon and fluorapatite grains in the Beaverlodge ridge regolith. (B) EMPA image of Fe-Ti oxide grains in the Beaverlodge ridge regolith. Fe-Ti oxide was originally ilmenite (?) with rutile (?) exsolution along crystallographic lattice plane. Remainder of the grain has been altered by chlorite.

Whole Rock Geochemistry

Whole rock geochemistry is summarized in Appendix B. Geochemical data are discussed below and shown in Figures 3.5 to 3.11 in five formats: 1) Zr versus X (where X is any major or trace element), 2) Isocon plots, 3) X versus distance from the unconformity, 4) trace element plots, and 5) REE plots. These diagrams shed light on the relative mobility of various elements compared to the least-altered sample and on the composition of the porphyry clasts and weathering rinds in the quartz arenite relative to the underlying porphyry.

1. Zr versus X

This plots an element X (where X = major or trace element) relative to the "immobile" element, in this case, Zr. Immobile elements often display little to no change during weathering (Sheldon and Tabor, 2009). However, as no element is 100% immobile, a combination of geochemistry and petrography is needed to determine the mobility of a particular element. Relatively immobile High Field Strength Elements (HFSE) include Al, Ti, Zr, and Nb (Palmer et al., 1989; Brantley and White, 2009; Mitchell and Sheldon, 2009; Brantley and Lebedeva, 2011). Zirconium was chosen as an appropriate immobile element because it typically resides in the highly refractory mineral zircon. Petrographic observations confirm that zircon grains show no signs of alteration (Figure 3.4.A), even in the most altered porphyry samples. Aluminum was not chosen as an immobile element because of the presence of secondary potassium aluminosilicates (i.e. sericite). Titanium was not chosen because it resides in accessory Ti and Fe-Ti oxides and as previously demonstrated, they have been partially replaced by chlorite. In addition, titanium concentrations are low in all of the porphyry samples (Figure 3.4.B). Niobium was not selected as the immobile element because of its low concentrations in all of the porphyry samples.

Binary elemental plots can be used to determine, which elements have been mobilized. All major elements in the altered porphyry show considerable spread relative to the least-altered porphyry (Figure 3.5). Altered porphyry samples have bulk SiO_2, MgO, and Na_2O contents less than the least-altered porphyry sample, whereas $Fe_2O_3^T$, CaO, and K_2O are higher. SiO_2, in the weathering rinds of the porphyry clasts, is higher than for the altered and least-altered porphyry, whereas $Fe_2O_3^T$, MgO, CaO, and Na_2O are lower (totals almost near zero in some cases) in comparison to the altered and least-altered porphyry. K_2O abundances in the weathering rinds and porphyry block are similar to the altered porphyry (Figure 3.5.G). Al_2O_3, in the altered porphyry and porphyry clasts, is higher than the least-altered, whereas Al_2O_3 abundances in the weathering rinds is less than the least-altered sample. TiO_2 abundances in the altered porphyry, porphyry clasts, and weathering rinds are higher than the least-altered (Figure 3.5.H). P_2O_5 abundances in

the altered porphyry, weathering rinds, porphyry clasts are higher than the least-altered porphyry.
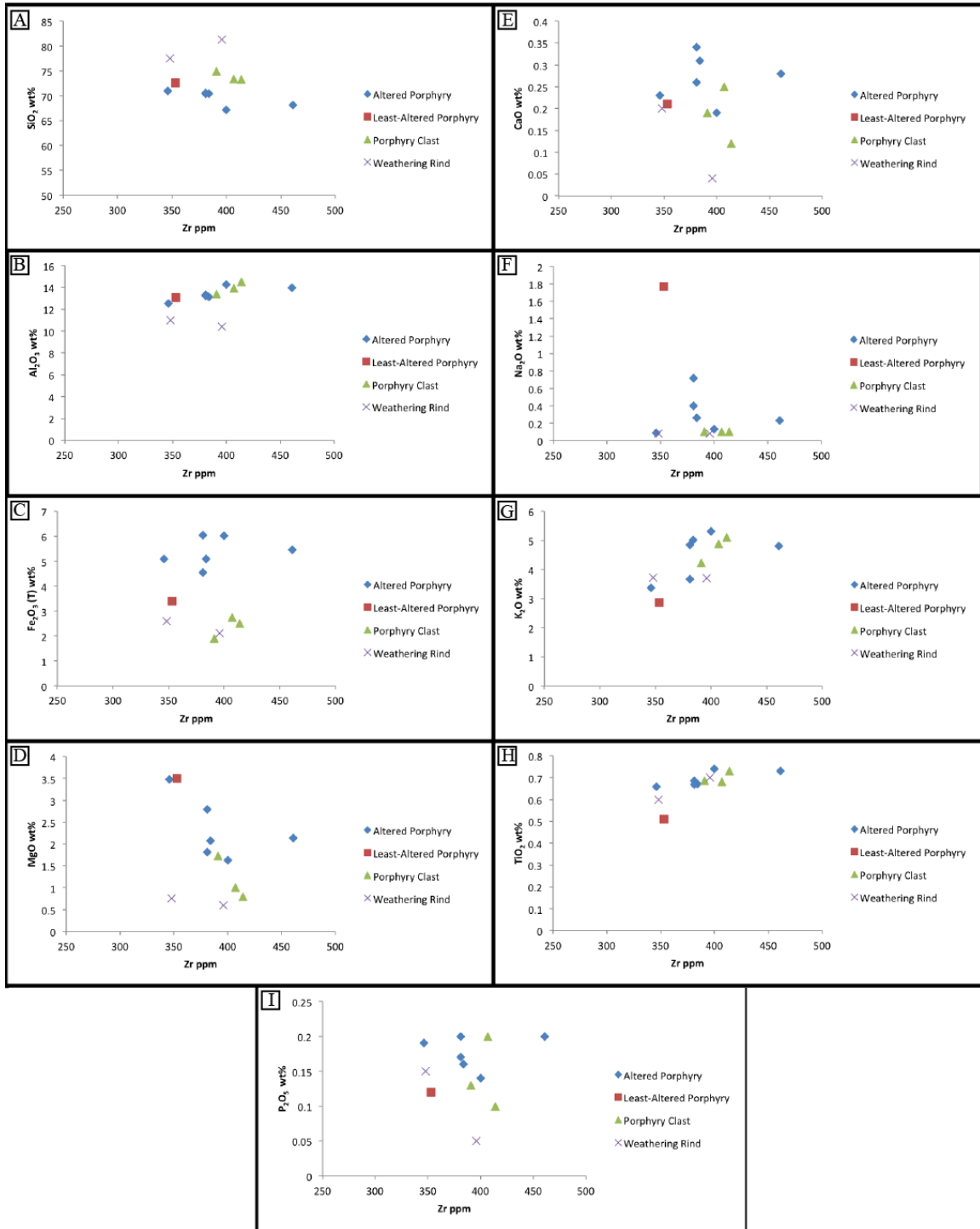
Figure 3.5 Binary plot of (A) SiO_2, (B) Al_2O_3, (C) $Fe_2O_3^T$, (D) MgO, (E) CaO, (F) Na_2O, (G) K_2O, (H) TiO_2, and (I) P_2O_5 versus Zr of the altered porphyry, least altered porphyry, porphyry clasts, and weathering rinds with respect to Zr.

25

The behaviour of trace elements is controlled by conditions of the weathering environment (Scott and Pain, 2008). Of particular interest to this study is the behaviour of Ba, Rb, and Sr as they are found in high abundances in the most altered porphyry samples. Barium and Sr are known to substitute into K- and Ca-bearing minerals, specifically alkali and plagioclase feldspars (Bouseily and Sokkary, 1975). Rubidium tends to concentrate in micas, specifically biotite or muscovite as well as K-feldspars (Scott and Pain, 2008). Figure 3.6 plots Ba, Sr, and Rb relative to the immobile element Zr. The altered porphyry Ba values are higher than the least-altered porphyry, and the weathering rinds and porphyry clasts are similar to the altered porphyry. The altered porphyry, weathering rind, and porphyry clast Sr concentrations are less than the least-altered porphyry. Finally, the altered porphyry, porphyry clasts, and weathering rinds Rb values are higher than the least-altered porphyry.
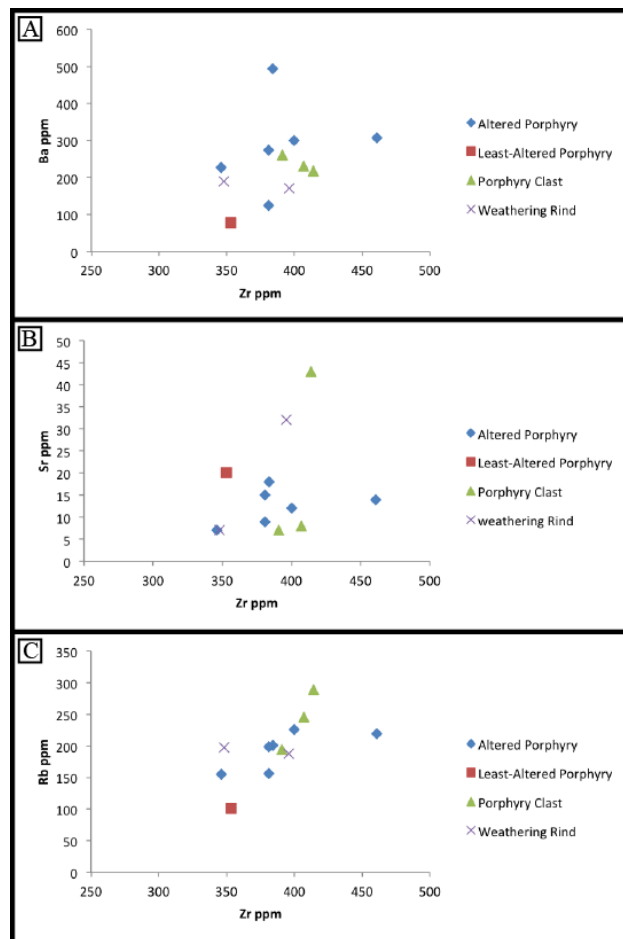
Figure 3.6 Binary plot of (A) Ba, (B) Sr, and (C) Rb values of the altered porphyry, least-altered porphyry, porphyry clasts, and weathering rinds with respect to Zr.

26

2. Isocon Plots

An additional useful method to access the relative mobility of elements is through isocon analysis. Grant (1986) proposed a graphical solution to Gresens' (1967) composition-volume equation in metasomatic alteration. In isocon analysis, Grant (1986) rearranges Gresens' (1967) equation and derives a linear relationship between the concentration of elements in altered rocks and concentration of elements in unaltered rock. Before doing so, one must define an isocon (a line of equal of geochemical concentration) and is represented by a straight line through the origin (Grant, 1986). Typically, three isocons are generated assuming: constant mass, constant volume, and constant element oxide (in this case Zr). The slope of the constant mass isocon is M^O/M^A, which represents the mass before (M^O) and after (M^A) alteration. The slope of the constant volume isocon is ρ_O/ρ_A, which represent the ratio of densities before and after alteration. And finally, the slope of constant Zr isocon is C_{Zr}^A/C_{Zr}^O where C_{Zr}^A represents the concentration of Zr in the most altered sample and C_{Zr}^O is the concentration of Zr in the least-altered sample. Gains and losses of elements are assessed by displacement of data from the reference isocon. Gain of element X plots above the reference isocon and loss of element X plots below the reference isocon. Isocon diagrams often require re-scaling of the data, which does not affect the slope of the isocon (Grant, 2005).

Figure 3.7 shows isocon analysis of altered porphyry, porphyry clasts, and weathering rinds. The constant mass and constant volume isocon have nearly identical slopes suggestion both volume and mass have been conserved. The best-fit isocon was determined to be the constant Zr isocon. The slope of the isocon is 1.1173. The constant Zr isocon is consistent with geochemical and mineralogical trends discussed before and forthcoming. Figure 3.7.A is an isocon diagram representing average concentrations of X element in altered porphyry samples collected below the unconformity. Elements that define the isocon and therefore show little mobility include: Zr, Al, and Ti. Elements that plot above the isocon (i.e. show gains) include: Fe, Ca, K, P, Ba, and Rb. Elements that plot below the isocon (i.e show losses) include: Si, Mg, Na, and Sr. Figure 3.7.B is an isocon diagram representing average chemical concentrations of X element in porphyry block samples. Zirconium, Al, Ti, and P define the isocon. Elements that plot above the

isocon include: K, Ba, and Rb. Elements that plot below the isocon include Si, Fe, Mg, Ca, Na, and Sr. Figure 3.7.C is an isocon diagram representing average chemical compostion of X element for weathering rind samples. Silicon, Zr, and Ti define the isocon. Elements that plot above the isocon include: K, Ba, and Rb. Elements that plot below the isocon include: Al, Fe, Mg, Ca, Na, P, and Sr. In order to calculate total mass change during alteration, the following formula (Equation 3.1) was used:

$$\Delta M = [(\frac{1}{S}) - 1] \times 100 \qquad \text{(Equation 3.1)}$$

where ΔM is total mass change and S is the slope of the isocon (Grant, 1986). Based on the above formula, the total mass change was about -10.49%. To calculate total volume changes during alteration the following formula (Equation 3.2) was used:

$$\Delta V = [(\frac{1}{S}) \times (\frac{\rho^A}{\rho^O}) - 1] \times 100 \qquad \text{(Equation 3.2)}$$

where ΔV is total volume change, S is the slope of the isocon, and ρ^A/ρ^O is the ratio of densities (Grant, 1986). Based on the above formula, the total volume change was about -14.90%.
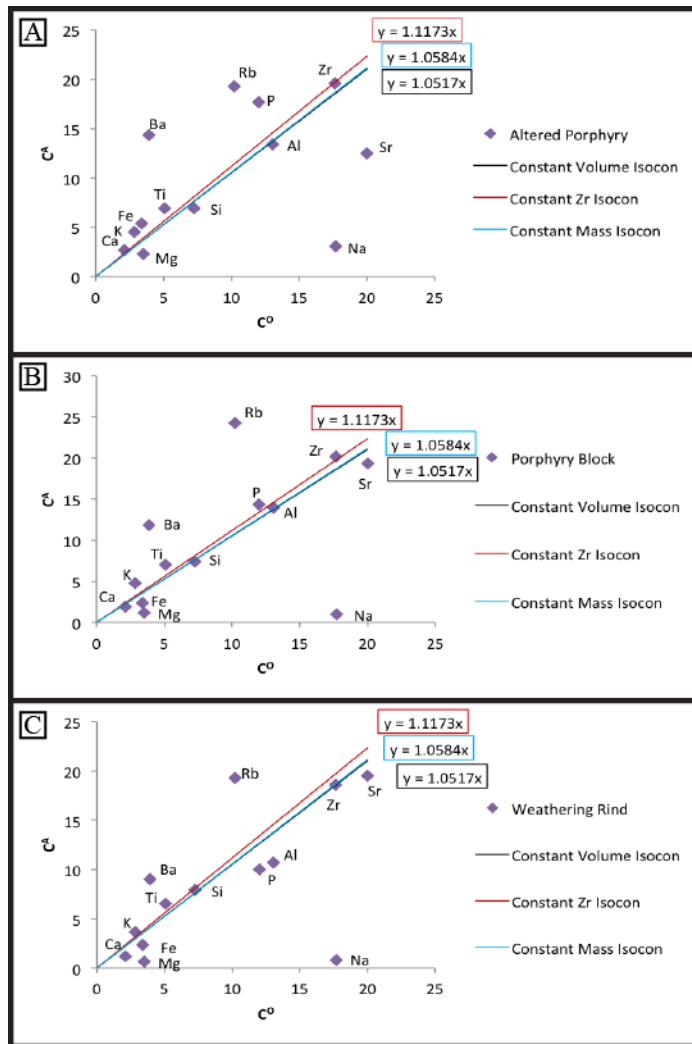
Figure 3.7 Isocon diagrams showing average element concentrations of porphyry samples. A deviation of the element from the isocon suggests an increase or depletion of the element relative to the least-altered sample. (A) Isocon diagam of altered porphyry samples collected below the unconformity. (B) Isocon diagram of porphyry block samples. (C) Isocon diagram of weathering rind samples.

3. X versus Distance from the Unconformity

Concentration values of X element of altered and least-altered porphyry samples are plotted as a function of distance from the unconformity on a single plot. These plots represent the concentration of X element of altered and least-altered porphyry samples collected below the unconformity. Two samples (BLU 9710 and BLU 9715 collected 40 and 45 metres from the unconformity, respectively) were removed from these plots as their behaviour is not consistent with the remaining samples. Figure 3.8 is a plot of bulk

29

major (SiO_2, Al_2O_3, $Fe_2O_3{}^T$, MgO, CaO, Na_2O, K_2O, TiO_2, and P_2O_5) elemental values for the altered porphyry and least-altered porphyry. SiO_2, MgO, and Na_2O decrease toward the unconformity, Al_2O_3, $Fe_2O_3{}^T$, K_2O, and P_2O_5 increase toward the unconformity, and CaO remains low and constant. Titanium is unchanged going towards the unconformity. These trends are consistent with Precambrian weathering profiles developed on granites after GOE (Maynard et al., 1995; Panahi et al., 2000).
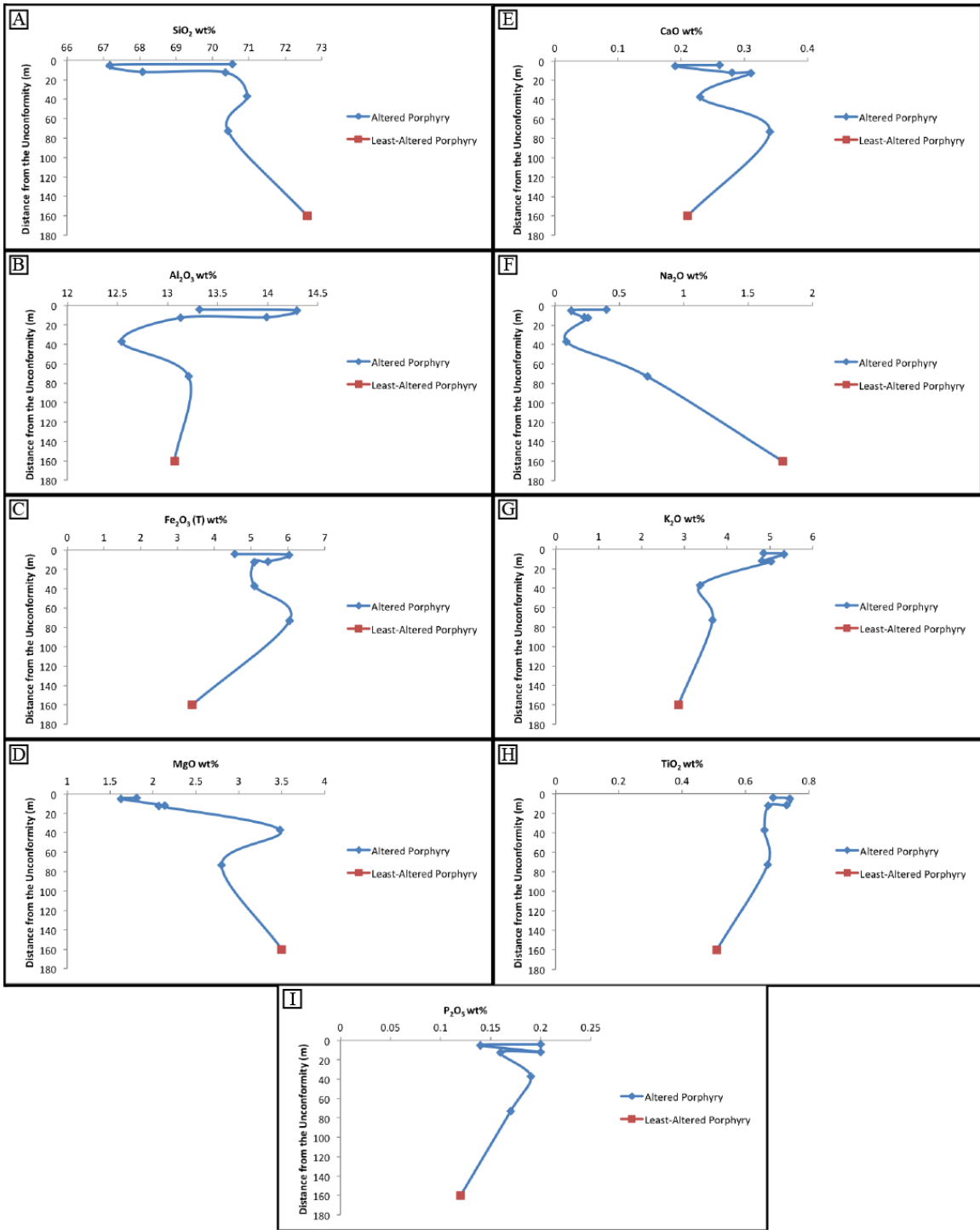
Figure 3.8 Plots of major element concentrations (A) SiO_2, (B) Al_2O_3, (C) $Fe_2O_3{}^T$, (D) MgO, (E) CaO, (F) Na_2O, (G) K_2O, (H) TiO_2, and (I) P_2O_5 for altered and least altered porphyry versus distance from the unconformity.

With respect to trace elements versus distance from the unconformity (Figure 3.9), Ba values increase dramatically toward the unconformity, from a least-altered value

of 78 ppm to as high as 493 ppm. Strontium values decrease toward the unconformity.
Rubidium increases toward the unconformity from 102 ppm to as high as 226 ppm.
Samples BLU 9710 and BLU 9715 were again removed form these plots, as their
chemical behaviour is not consistent with the remaining samples.
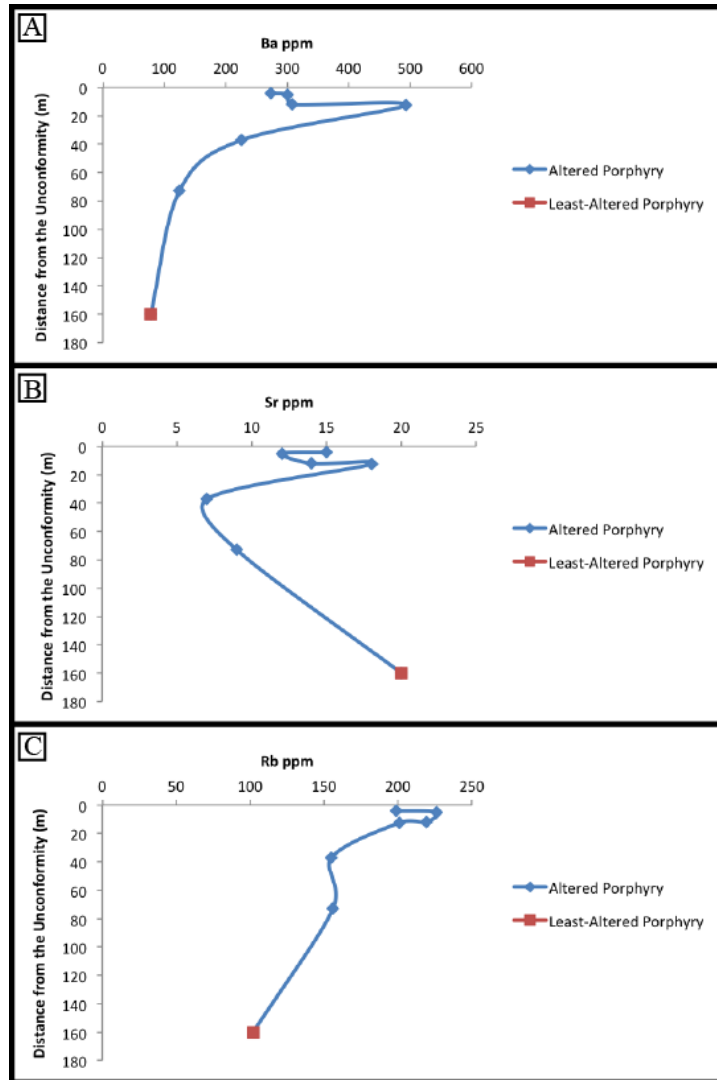
Figure 3.9 (A) Ba, (B) Sr, and (C) Rb values of the altered porphyry and least-altered porphyry versus distance from the unconformity.

4. Trace elements ratios

As with major element ratios, trace element ratios can be used to help normalize
differences and highlight different alteration processes (Sheldon and Tabor, 2009). Trace
element ratios have been used to distinguish weathering intensity (Sheldon and Tabor,

32

2009), to evaluate leaching (Mitchell and Sheldon, 2009; Sheldon and Tabor, 2009), and to examine weathering behaviours of different parent rock types (Scott and Pain, 2008; Mitchell and Sheldon, 2009; Sheldon and Tabor, 2009). The Ba/Sr ratio can help decipher leaching behaviour during weathering as both Ba and Sr have similar atomic radii and similar chemical affinities. Strontium is more soluble than Ba, so a heavily leached weathering profile should have a lower Ba/Sr ratio near the top of the profile and higher Ba/Sr values within the profile (Mitchell and Sheldon, 2009; Sheldon and Tabor, 2009). Figure 3.10.A plots the Ba/Sr ratio as a function of distance. The value for the least-altered porphyry is around 3.9 and is as high as 32 in the most altered porphyry suggesting a heavily leached profile.

An additional useful trace element ratio is the bulk Th/U ratio, which has been used to decipher provenance and pedogenesis (Condie et al., 1995; Pan and Stauffer, 2000; Sheldon and Tabor, 2009; Lahtinen and Nironen, 2010). A higher Th/U in the weathering profile compared to the parent material suggests intense weathering conditions and presence of a strong redox gradient, whereas a constant Th/U ratio suggests no significant redox gradient and pedogenesis was not intense (Sheldon and Tabor, 2009). The Th/U ratio from the least-altered porphyry to the top of the regolith remains constant, between 2.8 to 3.4, suggesting no significant redox gradient (Figure 3.10.B; Sheldon and Tabor, 2009). A constant Th/U ratio could also be interpreted to mean that the uranium in the uranium mineralization at Beaverlodge Lake (Tatie) did not come from the weathering profile.
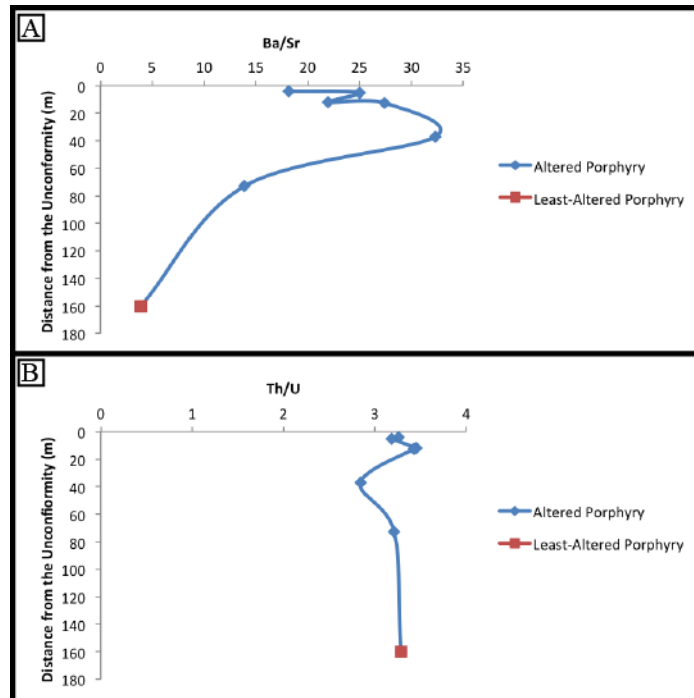
Figure 3.10 Trace element ratios of altered and least-altered porphyry, (A) Ba/Sr and (B) Th/U plotted as a function of distance from the unconformity.

5. Rare Earth Elements

The mobility and fractionation of REEs during weathering has been the subject of intense research since the 1980s (Nesbitt, 1979; Duddy, 1980; Pan and Stauffer, 2000; Panahi et al., 2000). While REEs generally have a 3+ oxidation state, under reducing conditions, europium has an oxidation state of 2+ and under oxidizing conditions, cerium has an oxidation state of 4+ (Winter, 2001). Reduction of Eu^{3+} to Eu^{2+} makes it available to replace Ca^{2+}, Sr^{2+}, and Na^{+} in plagioclase feldspar (Panahi et al., 2000). Relevant to this study, REEs can be redistributed during weathering such that they may be depleted in one section and enriched in another (Scott and Pain, 2008).

Figure 3.11 plots, chondrite-normalized, REE values of the porphyry clasts, weathering rinds, altered porphyry, and least-altered porphyry of the Beaverlodge Lake regolith. Table B.3 summarizes percent changes of light REE ($\Sigma LREE_N = La_N$ to Nd_N), medium REE ($\Sigma MREE_N = Sm_N$ to Dy_N), and heavy REE ($\Sigma HREE_N = Er_N$ to Lu_N) relative to the least-altered porphyry. It appears that a minor amount of REE mobilization

34

occurred in the regolith. With respect to altered porphyry samples, some samples plot above and below the least-altered sample. Altered porphyry samples show a similar general trend as the least-altered porphyry (i.e. negative slope and pronounced negative Eu anomaly). The average percent change of $\Sigma LREE_N$ is 14.8% in altered porphyry samples (Table B.3). The average percent change of $\Sigma MREE_N$ and $\Sigma HREE_N$ for altered porphyry samples is -0.5% and -15.9%, respectively (Table B.3). Weathering rinds also show enrichment in $\Sigma LREE_N$ (24.0%). Weathering rinds also show enrichment in $\Sigma MREE_N$ (14.1%) relative to the least-altered porphyry sample; however $\Sigma HREE_N$ in weathering rinds show depletion (-8.2%) relative to the least-altered porphyry. Weathering rinds follow the same general trend as the least-altered porphyry. Porphyry clasts, on the other hand, show depletion in $\Sigma LREE_N$, $\Sigma MREE_N$, and $\Sigma HREE_N$ (-46.6%, -23.8%, and -17.4%, respectively) compared to the least-altered porphyry, but show the same general overall trend as the least-altered porphyry (Table B.3).
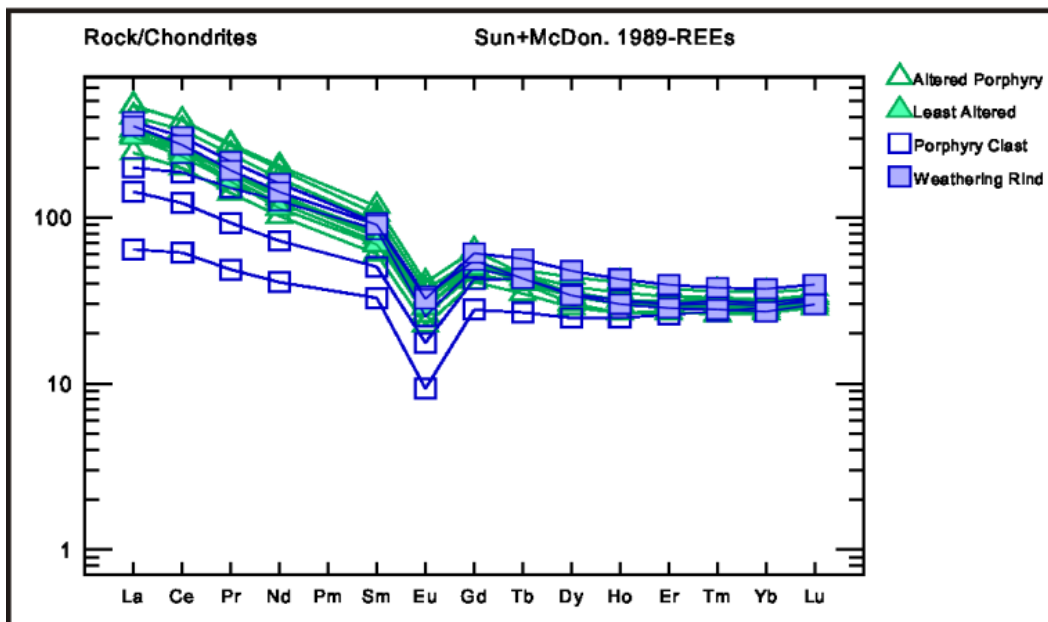
Figure 3.11 Normalized REE diagrams of altered porphyry, porphyry clast, weathering rind, and least-altered porphyry at Beaverlodge ridge. REE normalized to C1 chondrites from Sun and McDonough, 1989.

The above observations are further supported by Zr versus $\Sigma LREE_N$ (Figure 3.12). Altered porphyry and weathering rinds are enriched in LREE compared to the least-

altered porphyry, whereas porphyry clasts are less enriched in LREE compared to the least-altered porphyry.
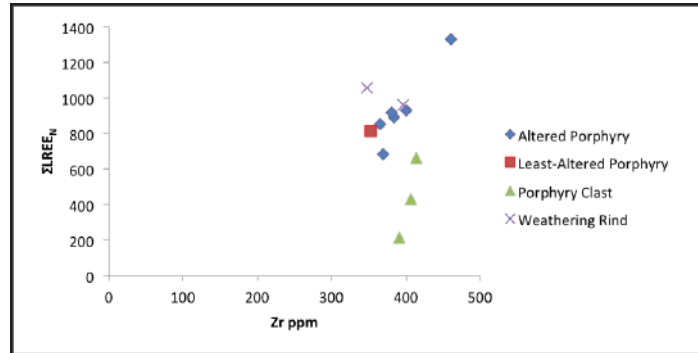
Figure 3.12 Binary plot of $\Sigma LREE_N$ versus Zr of altered porphyry, least-altered porphyry, porphyry clasts, and weathering rinds

Light REE remobilization and enrichment in the altered porphyry can also be observed using $\Sigma LREE_N$ versus distance where $\Sigma LREE_N = 814$ of the least-altered porphyry and 1329 of the most altered porphyry (Figure 3.13).
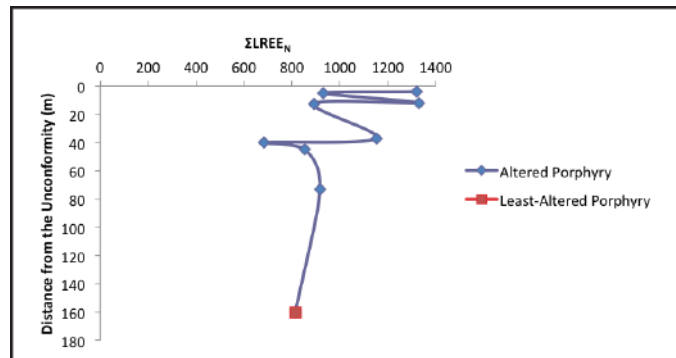
Figure 3.13 Plot of $\Sigma LREE_N$ versus distance from the unconformity.

Light REE remobilization in the regolith is supported by backscatter electron (BSE) imaging. Monazite grains are common in and around primary fluorapatite crystals, suggesting remobilization of LREE at least on a micrometer scale (Figures 3.14.A and B). Monazite grains are often seen filling small cracks in fluorapatite grains and in small voids in the surrounding heavily altered groundmass thus are interpreted to be secondary in nature. Presence of secondary monazites could explain the increase in P_2O_5 going from unweathered porphyry to weathered equivalent.
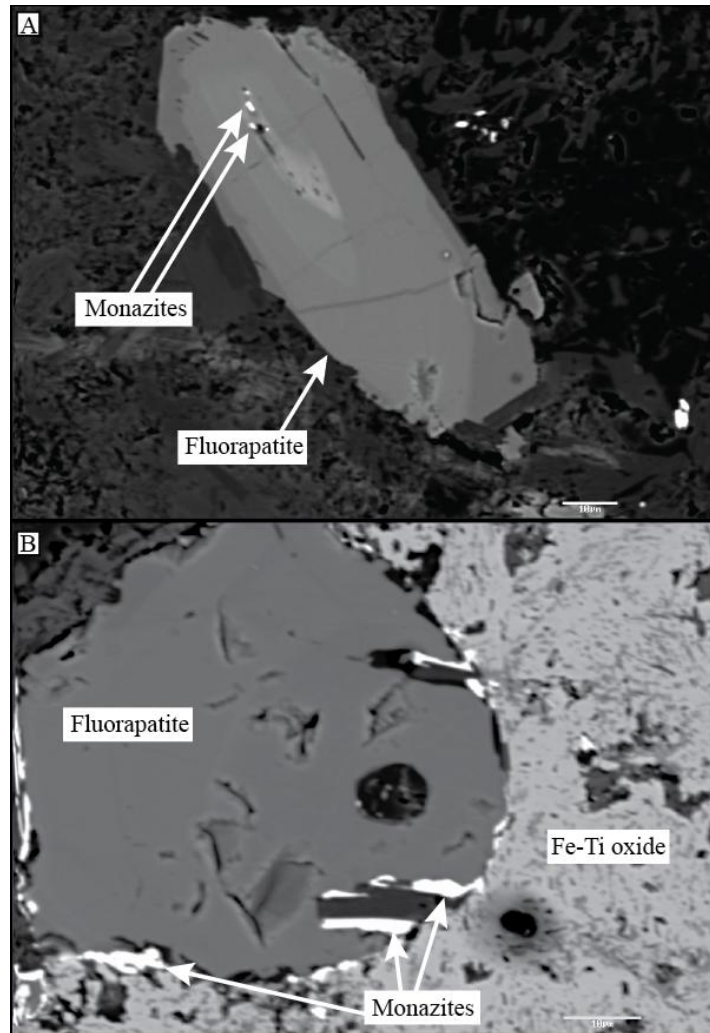
Figure 3.14 (A) Backscattered electron image of fluorapatite grain with secondary monazite grains inside the fluorapatite. (B) EMPA image of fluorapatite and Fe-Ti oxide with secondary monazite outside the fluorapatite.

The pronounced chondrite-normalized negative Eu anomaly in the porphyry clasts, weathering rinds, altered and least-altered porphyry samples suggests inheritance of the anomaly from the original protolith. The negative anomaly might be due to substitution of Eu^{2+} for Ca^{2+} in the plagioclase feldspar phenocrysts and fractional crystallization of plagioclase feldspar in the source magma (Winter, 2001). The size of the negative Eu anomaly in altered and least-altered porphyry, Eu/Eu*, has a range of values from 0.45 to 0.49. When plotted as a function of distance from the unconformity, Eu/Eu* appears constant going towards the unconformity (Figure 3.15).
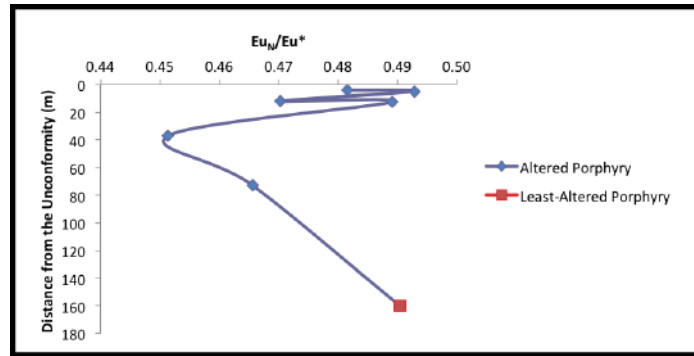
Figure 3.15 Size of Eu anomaly, Eu/Eu*, versus distance from the unconformity

Discussion

Major element weathering indices

Weathering indices can be used to quantify the totality of weathering processes. One of the most common weathering indices is the chemical index of alteration (CIA). The CIA is a measurement of the weathering of feldspar minerals and their hydration to form clay minerals (Sheldon and Tabor, 2009). The formula (Equation 3.3) for the CIA is:

$$CIA = (\frac{Al_2O_3}{Al_2O_3 + CaO^* + Na_2O + K_2O}) \times 100 \qquad \text{(Equation 3.3)}$$

As clay content increases, Al_2O_3 also increases, but CaO^* and Na_2O should decrease, and therefore CIA should increase. An increase in Al_2O_3 could be due to introduction of Al_2O_3 into the system or a volume reduction. Initial CIA values vary for different parent materials and changes in CIA from parent to weathered material can be large or small (Sheldon and Tabor, 2009). For example, fresh basalts have CIA values ranging from 30 to 40, whereas fresh granites have CIA values around 50 to 60. Chemical Index of Alteration values at Beaverlodge range from 68 in the least-altered porphyry to 77 in the most altered porphyry (Appendix B). However, caution must be taken when using the CIA on Precambrian paleoregoliths as addition of K_2O by metasomatism due to burial of the weathering profile, diagenesis of overlying sediments, or illitization of clay minerals may modify CIA values (Sheldon and Tabor, 2009). As a result, an additional weathering index without K_2O has been developed, termed CIA – K (Sheldon and Tabor, 2009). The formula for CIA – K is summarized by Equation 3.4.

$$\mathrm{CIA-K} = (\frac{\mathrm{Al_2O_3}}{\mathrm{Al_2O_3 + CaO^* + Na_2O}}) \times 100 \qquad \text{(Equation 3.4)}$$

CIA – K values of the Beaverlodge regolith range from 81 in the least-altered porphyry to 99 in the most altered porphyry (Appendix B).

When plagioclase feldspar weathering alone is considered, the Plagioclase Index of Alteration (PIA) should be used (Equation 3.5; Fedo et al., 1995). The formula is:

$$\mathrm{PIA} = (\frac{\mathrm{Al_2O_3 - K_2O}}{\mathrm{Al_2O_3 + CaO^* + Na_2O - K_2O}}) \times 100 \qquad \text{(Equation 3.5)}$$

PIA values range from 77 for the least-altered porphyry to 99 for the altered porphyry (Appendix B). $\mathrm{Al_2O_3}$, $\mathrm{CaO^*}$, $\mathrm{Na_2O}$, and $\mathrm{K_2O}$ values used in the three weathering indices presented above are calculated in terms of moles. $\mathrm{CaO^*}$ represents Ca in silicate-bearing minerals only so Ca in non-Ca-silicates including calcite, dolomite, and apatite is removed (Fedo et al., 1995).

Mass Transfer and Mass Balance

Many geologic processes can be described in terms of which elements are involved in a given process and how their abundances and distribution vary relative to the parent material. One common method of accessing gains and losses in a regolith is through mass balance (Sheldon and Tabor, 2009). Two new sets of plots are presented, which shed further light into the nature of the alteration at Beaverlodge Lake.

1. ε versus τ to determine an immobile

In order to determine changes in the *mass* of the regolith, we compare the concentration of an element or an oxide (C_j), such as $\mathrm{SiO_2}$ in a weathered rock (written as $C_{j,w}$; where $_w$ denotes a sample from the regolith) against the same component in the protolith or parent rock ($C_{j,p}$; White et al., 2001; Brantley and White, 2009). Variation in $C_{j,w}$ reflects changes in mass, but also changes due to losses and gains of other components as well as other factors such as compaction or dilation of the original regolith. This could affect the original volume, V_p, compared to the regolith, V_w (White et al., 2001; Brantley and White, 2009). Concentration ratios of the weathered component

in the regolith compared to the protolith are defined by the following equation (Equation 3.6; White et al., 2001; Brantley and White, 2009).

$$\frac{C_{j,w}}{C_{j,p}} = \frac{\rho_\rho}{\rho_w} \frac{1}{(\varepsilon_i + 1)}(1 + \tau_j)$$ (Equation 3.6)

Any change in the concentration ratio, $C_{j,w} / C_{j,p}$, can be explained by changes in three variables: (i) ratio of bulk densities (ρ_ρ / ρ_w); (ii) volume change or strain of an immobile element in the regolith (ε_i), and; (iii) mass transport coefficient of a second element with respect to the immobile element (τ_j), which describes component *j* as either loss, gain, or conservative (See Equations 3.5 and 3.6; Brimhall and Dietrich, 1987; Brimhall et al., 1992; Sheldon, 1996; White et al., 2001; Buss et al., 2008; Brantley and White, 2009; Sheldon and Tabor, 2009; Mitchell and Sheldon, 2009; Du et al., 2012).

Volumetric strain is a function of the ratios of densities and concentration of element *i* (Brantley and White, 2009) and can be calculated from Equation 3.7. Positive ε_i values indicate expansion of the regolith, negative values indicate collapse, and $\varepsilon_i = 0$ show isovolumetric weathering (Brantley and White, 2009).

$$\varepsilon_{i,w} = \frac{\rho_\rho \times C_{i,p}}{\rho_w \times C_{i,w}} - 1$$ (Equation 3.7)

The mass transfer coefficient, $\tau_{j,w}$, can be simplified as follows (Equation 3.8).

$$\tau_{j,w} = \frac{\rho_w \times C_{j,w}}{\rho_\rho \times C_{j,p}}(\varepsilon_{i,w} + 1) - 1$$ (Equation 3.8)

When $\tau_{j,w} < 0$, removal of component *j* has occurred; when $\tau_{j,w} > 0$, addition of component *j* has occurred; finally, when $\tau_{j,w} = 0$, isomass weathering has occurred indicating no loss or gain of component *j* (White et al., 2001; Sheldon, 2006; Buss et al., 2008; Brantley and White, 2009; Mitchell and Sheldon, 2009; Brantley and Lebedeva, 2011; Du et al., 2012). An appropriate immobile element must be determined prior to examining the mass transport coefficient of the typical mobile elements (SiO_2, $Fe_2O_3{}^T$, MgO, CaO, Na_2O, K_2O, Ba, Sr, and Rb). As previously discussed, traditional immobile HFSE include Al, Ti, and Zr. To determine the appropriate immobile element, plots of $\varepsilon_{i,w}$ versus $\tau_{j,w}$ were completed, resulting in six possible combinations (Table B.4). The

plot of $\varepsilon_{Zr,w}$ versus $\tau_{Ti,w,\varepsilon(Zr)}$ demonstrate a small range in $\varepsilon_{Zr,w}$ (-0.151 to 0.028) with a greater range of τ_{Ti}, (0.098 to 0.321; Figure 3.16.A). This result supports petrological observations that Zr was unaffected during weathering. The plot of $\varepsilon_{Zr,w}$ versus $\tau_{Al,w,\varepsilon(Zr)}$ demonstrate a slightly larger range in $\varepsilon_{Zr,w}$ compared to τ_{Al} (-0.180 to -0.021; Figure 3.16.B). However, presence of sericite suggests alteration of primary Al-bearing mineral (K-feldspar and plagioclase feldspar) to a more OH-rich sheet silicate.
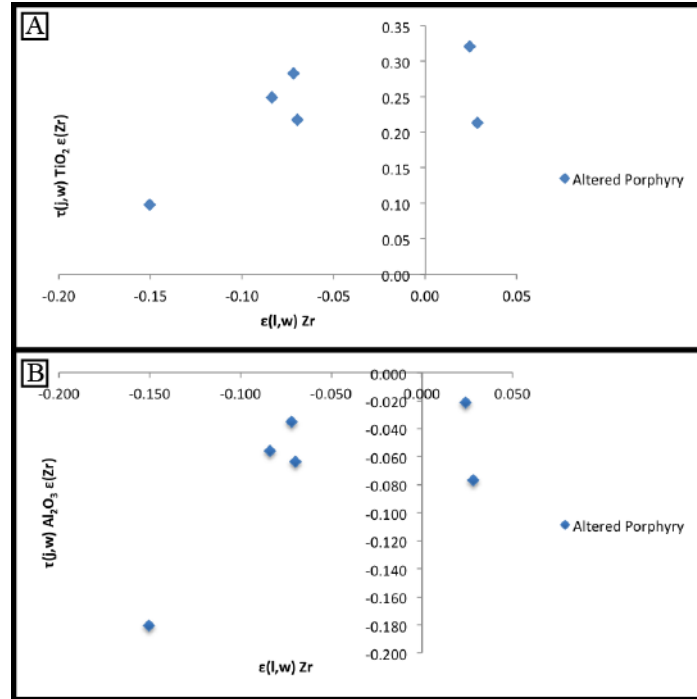
Figure 3.16 (A) $\varepsilon_{Zr,w}$ versus $\tau_{Ti,w,\varepsilon(Zr)}$ to determine the immobile element. Negative $\varepsilon_{Zr,w}$ values indicate collapse whereas positive $\varepsilon_{Zr,w}$ indicate expansion of the regolith. Wide range of values for $\tau_{Ti,w,\varepsilon(Zr)}$ indicate addition of Ti relative to immobile Zr.

2. τ versus Distance from the Unconformity

The elements typically considered mobile (SiO_2, $Fe_2O_3{}^T$, MgO, CaO, Na_2O, K_2O, Ba, Sr, and Rb) are plotted as a function of distance from the unconformity (Table B.5). Figure 3.17 plots the mass transport coefficient ($\tau_{j,w}$) of major elements as a function of distance from the least-altered to the top of the regolith, assuming Zr to be immobile. There is a loss in SiO_2 (between ~10 – 30%) and a loss in MgO (almost 60%). $Fe_2O_3{}^T$ shows gains in the profile, between ~20 – 60 %. The largest gains/losses in the profile were observed in Na_2O and K_2O. Loss of Na_2O is upwards of 95% and gains of K_2O are

41

upwards of 60%. Initial gain of CaO is up to 50%. However, closer to the unconformity, values of CaO show 0% change compared to the least-altered porphyry sample.
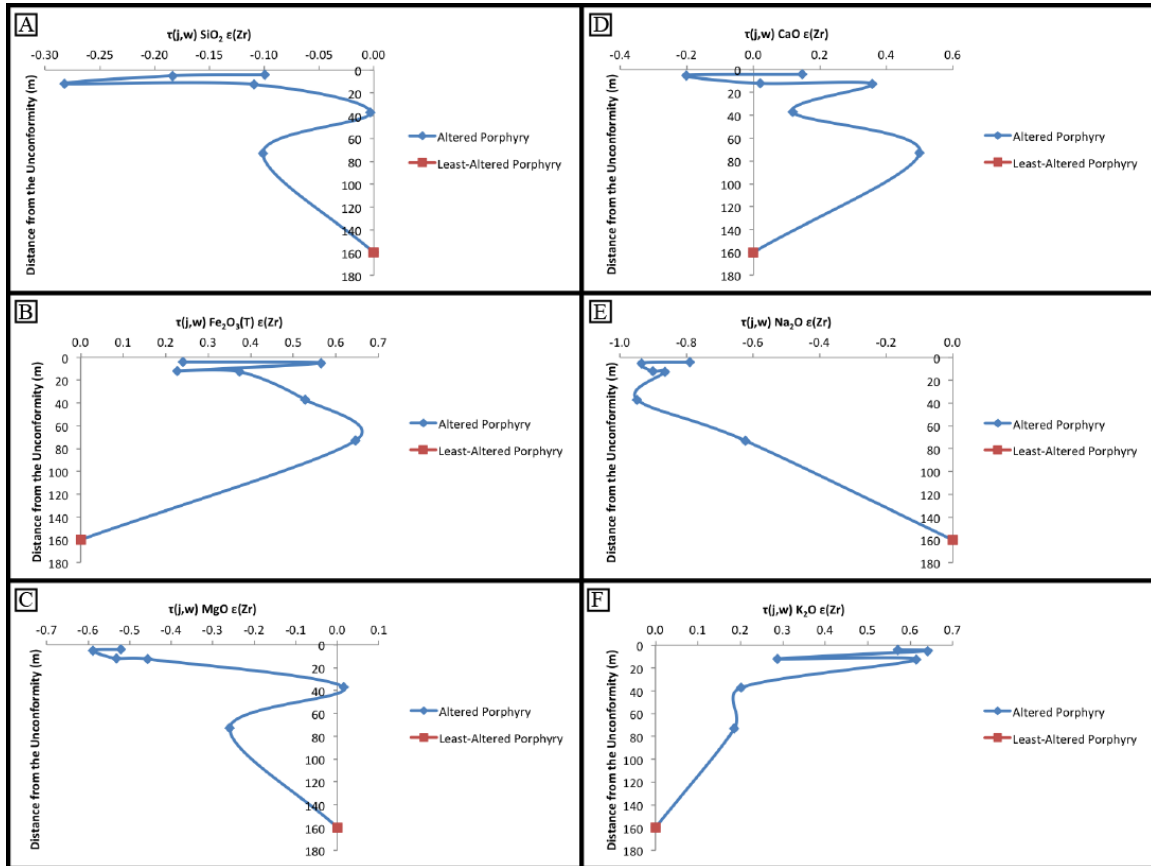
Figure 3.17 Results of mass-balance calculations of major elements (considering Zr immobile) and previously decided least-altered sample as the parent rock. Losses are represented by negative and gains are represented by positive values. See text for more information.

Mass transport coefficients were also calculated for the trace elements Ba, Sr, and Rb and plotted as a function of distance from the unconformity (Figure 3.18). While the loss of Sr is between 40 and 60%, large gains were observed in Rb (around 75%) and Ba (around 200% with one sample at 480%).

42
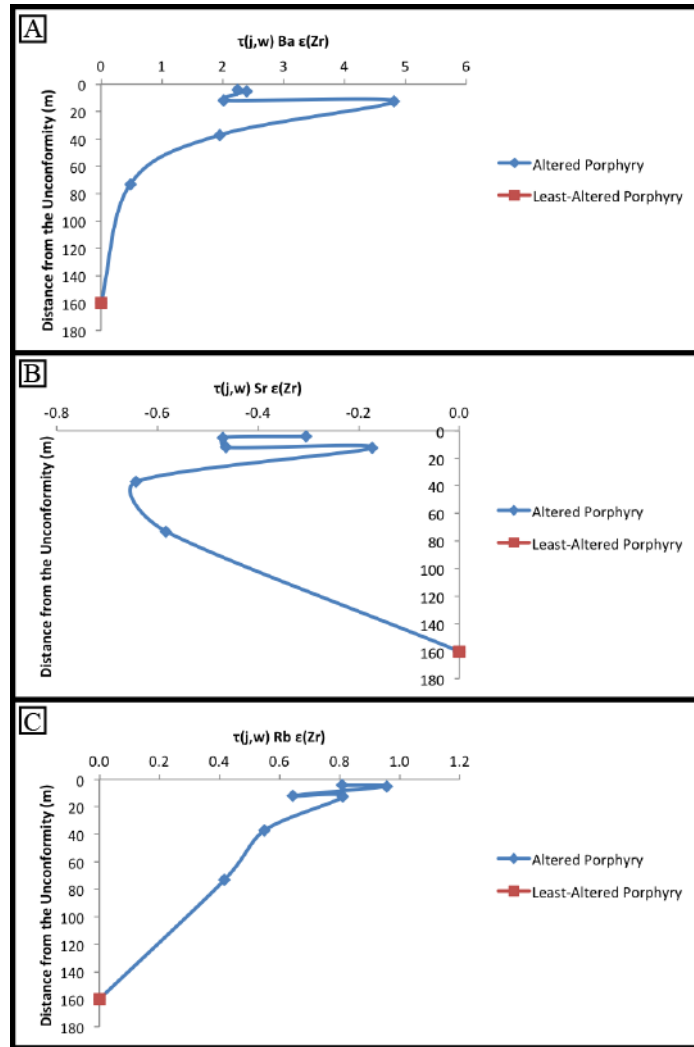
Figure 3.18 Results of mass-balance graphs calculations of trace elements: (A) Ba, (B) Sr, and (C) Rb (considering Zr immobile) and previously decided least-altered sample as the parent rock. Losses are represented by negative and gains are represented by positive values. See text for more information.

Mass balance calculations of four representative REEs (La, Ce, Eu, and Er) was also undertaken on the altered porphyry, similar to the approach undertaken for the major and trace elements. Lanthanum, Ce, and Eu are enriched toward the unconformity by about 10% to 50%, whereas Er is depleted by about 20% to 30% (Figure 3.19).
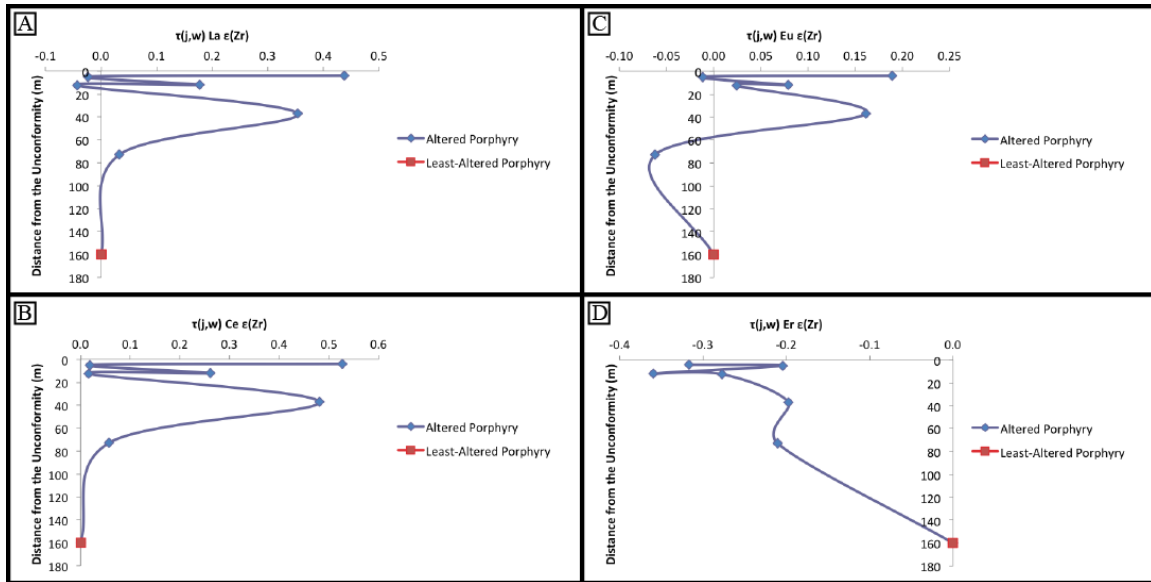
Figure 3.19 Results of mass-balance graphs calculations of rare earth elements: (A) La, (B) Ce, (C) Eu, and (D) Er (considering Zr immobile) and previously decided least-altered sample as the parent rock. Losses are represented by negative and gains are represented by positive values. See text for more information.

Physical Weathering and Paleolatitude of Beaverlodge ridge ca. 1.9 Ga

The process by which a consolidated rock breaks down is complex as it involves multiple factors that include source composition, climate, drainage, and relative rates of chemical and physical weathering (Prothero and Schwab, 2004). The rate of chemical weathering increases with increasing total precipitation and temperature, and therefore chemical weathering is rapid and effective in wet humid climates. As a result, soils/regoliths that developed under humid (tropical to subtropical) weathering conditions will be deep and well developed. In arid or cold regions such as in deserts or in polar weathering conditions, physical weathering is the dominant form of weathering (Scott and Pain, 2008). Thus, soils/regoliths developed in arid or cold conditions will be thin and not well preserved (Scott and Pain, 2008).

Irving et al. (2004) reported 18 paleopoles from red beds and igneous rocks from western Laurentia. The samples collected extend over a range at least of 100 million years between 1960 and 1830 Ma and formed during the Hudsonian orogeny. Paleolatitude for western Laurentia ca. 1960 – 1830 Ma, during the deposition of the

44

redbeds was 15 to 30° (Irving et al., 2004). Mitchell et al. (2010) constructed the Orosirian (2.05 Ga to 1.8 Ga) paleomagnetic poles from the Slave craton and calculated paleolatitudes at roughly 0° - 15° for that time period. The Irving et al. (2004) and Mitchell et al. (2010) estimates were nearly identical to those proposed for the assembly of the supercontinent Nuna (Zhao et al., 2002; Evans and Mitchell, 2011). This suggests that Laurentia and therefore Beaverlodge Lake were in a paleolatitude between 0° and 30° at ca. 1.9 Ga and therefore experienced tropical to subtropical weathering conditions.

Comparison with modern weathering profiles

The maximum calculated CIA – K and PIA values for the Beaverlodge Lake regolith are 99.1 and 98.7, respectively, indicating advanced weathering (Fedo et al., 1995) and the retention of $Fe_2O_3^T$ in the profile is consistent with other regoliths that formed after GOE (Rye and Holland, 1998). The almost complete removal of Na_2O and loss of SiO_2 suggest the destruction of plagioclase feldspar. The conversion of plagioclase to sericite and clay minerals is similar to other regoliths developed on granites (Maynard et al., 1995; Panahi et al., 2000). The increase in Al_2O_3 could be due to the presence of sericite in the heavily altered porphyry samples. Young and Nesbitt (1998) suggested that Al should remain fairly constant in weathering profiles except for the upper parts of the profile. The nearly constant and low CaO values throughout the Beaverlodge regolith likely reflect relatively low initial CaO concentration in the original protolith. Most Precambrian paleosols developed on both basalts and granites display a progressive loss of CaO from unweathered rock to weathered equivalents, due to the breakdown of plagioclase feldspar and the formation of clay minerals (Holland et al., 1989; Wiggering and Beukes, 1990; Gall, 1994; Pan and Stauffer, 2000). Calcium in porphyry samples resides in low Ca plagioclase phenocrysts (calcic cores of Na-plagioclase) and accessory fluorapatites. Accessory fluorapatites remained intact during alteration, which could explain why CaO remains nearly constant and low throughout the regolith (Figure 3.14.B). The decrease in Mg up-profile suggests a breakdown of Fe-Mg silicate minerals such as biotite or hornblende and the formation of Fe-oxides (Driese et al., 2011), which is common in paleoweathering profiles (Rye and Holland, 1998).

Nesbitt and Wilson (1992) showed that the trends in modern chemical weathering in basalts are not affected by the climate or the time of formation. They suggested that rainfall is the biggest determinant of the mineralogy and bulk composition of the soil. In "dry zones," they argued that chemical weathering only goes as far as the intermediate stages before erosion removes the weathering products. Therefore, weathering zones and horizons will usually be thin and the likelihood of preserving major weathering events is small (Nesbitt and Wilson, 1992). However, in "wet zones," mature weathering profiles are produced and will likely be thick with advanced to well-developed weathering zones (Nesbitt and Wilson, 1992). Introduction of acids will accelerate chemical weathering and lead to the development of a more depleted weathering zone (Nesbitt and Wilson, 1992). While the regolith at Beaverlodge Lake is not developed within a basalt protolith, presence of a thick well-developed regolith as well as published paleolatitude data ca. 1.9 Ga suggest that the Beaverlodge Lake regolith formed in a "wet zone."

The development of positive Ce anomalies is common in modern weathering profiles and has been attributed to the oxidation of Ce^{3+} to Ce^{4+} and the precipitation of highly insoluble phases such as cerianite near the top of weathering profiles (CeO_2; Braun et al., 1990; Pan and Stauffer, 2000). Many investigators have found that the Ce anomaly is concentrated in the upper, more oxidized parts of the weathering profile (Pan and Stauffer, 2000; Taylor and Eggleton, 2001). Braun et al. (1990) discussed a Ce anomaly at four different lateritic profiles. The positive Ce anomaly is found near the top of the saprolite, beneath a zone of iron oxide accumulation and cerianite is present as very fine coatings on clay surfaces (Braun et al., 1990). At Flin Flon, Pan and Stauffer (2000) described a positive Ce anomaly in the uppermost maroon paleosol. They also described very-fine aggregates of cerianite in muscovite/paragonite. Lahtinen and Nironen (2010) described a small positive Ce anomaly in some ca. 1.85 Ga Tiirismaa and Pyhäntaka paleosol samples. They also described a strong positive Ce anomaly in the Pyhäntaka duricrust fragment and some meta-arkoses. Lahtinen and Nironen (2010) concluded that these Ce positive anomalies indicate an oxidizing environment at the time of paleosol formation.

While positive Ce anomalies occur near the top of weathering profiles, negative Ce anomalies tend to form at weathering fronts (Braun et al., 1990; Braun et al., 1998; Walden, 2005). Local anoxic weathering conditions can and frequently do inhibit the formation of Ce anomalies during weathering under today's high O_2 atmosphere (Braun et al., 1990; Walden, 2005). The presence of a Ce anomaly implies high atmospheric O_2 during weathering, but the absence of one does not require low atmospheric O_2 levels (Walden, 2005). Due to its restricted occurrence in a weathering profile, Ce anomalies are susceptible to removal by erosion (Pan and Stauffer, 2000). In some modern weathering profiles, Ce anomalies are absent (Morteani and Preinfalk, 1996).

As previously discussed, Ce anomalies tend to occur in the upper more oxidized soil zones of the weathering profile and are highly susceptible to being removed by erosion. The absence of a Ce anomaly in the Beaverlodge Lake regolith could be due to the removal of the upper oxidized soil horizon by erosion. Absence of vegetation in the Paleoproterozoic would make removal of the upper oxidized soil horizon during weathering easier. Low atmospheric O_2 was unlikely at the time of formation of the Beaverlodge Lake regolith as other weathering profiles approximately the same age as the Beaverlodge display positive Ce anomaly. Contrary to this, recent work by Frei et al. (2013), who looked at Cr isotopes in Banded Iron Formations deposited ca. 1.9 Ga, has led to the suggestion that the atmosphere during this period was not overly oxidized.

Metamorphism, metasomatism, diagenesis, or weathering?

The above descriptions of elemental changes in the weathering profile at Beaverlodge Lake did not differentiate weathering processes from subsequent activities (e.g. late hydrothermal activity along the unconformity and low-grade regional metamorphism). Diagenesis and/or metasomatism as well as low-grade regional metamorphism have modified the abundances of major and trace elements in the regolith (e.g. K, Fe, Ba, Sr, and Rb).

Enhanced K_2O is a common phenomenon within Precambrian paleosols (Mitchell and Sheldon, 2009). There are a number of possible mechanisms for potassium

enrichment such as "reverse weathering," where excess K_2O is derived from the water column in which the overlying sediments were deposited, movement of groundwater along the unconformities, and metasomatic alteration (Wiggering and Beukes, 1990). Potassium enrichment in the Beaverlodge regolith is apparent by the presence of K-rich minerals such as sericite and in the geochemistry by an increase in K_2O going up profile. Samples collected away from the unconformity show minimal sericite alteration of plagioclase feldspar phenocrysts and surrounding groundmass, whereas samples near the unconformity show abundant sericite alteration of plagioclase feldspar phenocrysts and surrounding groundmass, suggesting that these chemical and mineralogical chances were not effects of metamorphism, metasomatis, and diagenesis.

The chemical compositions of paleosols are typically plotted within Al_2O_3, CaO^*+ Na_2O, K_2O (A-CN-K) compositional space. Figure 3.20 plots A-CN-K for the altered and least-altered porphyry at Beaverlodge Lake. It shows that there has been an increase in K_2O, and as previously demonstrated, removal of Na_2O and low concentrations of CaO.
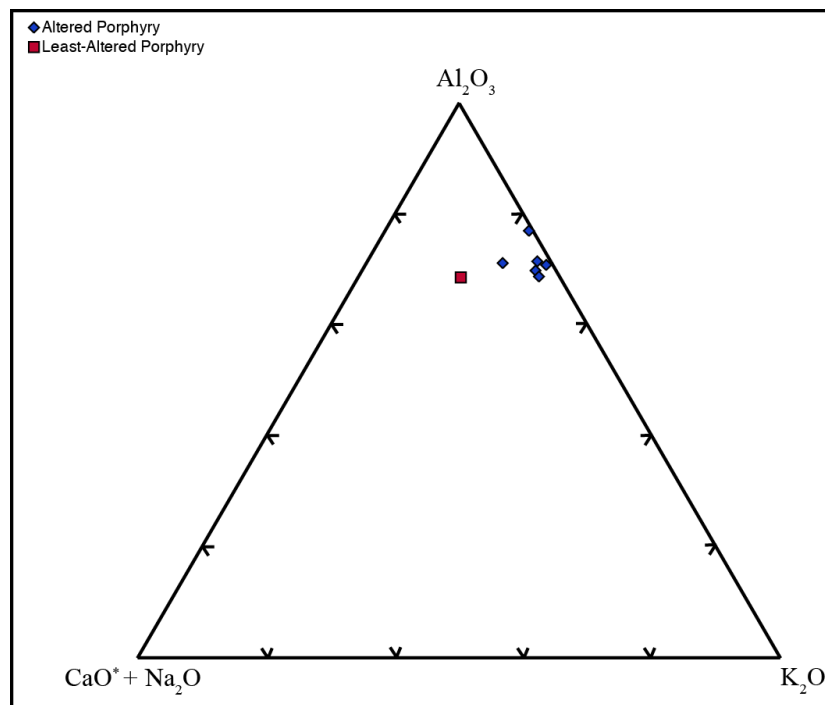
Figure 3.20 A-CN-K ternary diagram showing low Na_2O and CaO and elevated K_2O concentrations in the altered and least-altered porphyry.

Binary elemental plots of Ba, Sr, and Rb relative to immobile Zr show varying degrees of enrichment relative to the least-altered porphyry. Mass-balance plots of K_2O, Rb, and Ba of the altered porphyry as a function of distance, indicate addition of K_2O, Rb, and Ba relative to the least-altered porphyry. On the other hand, mass-balance plots of Sr as a function of distance suggest a loss relative to the least-altered porphyry. This suggests the following sequence of events: (1) exposure of the Hottah porphyry to the Paleoproterozoic atmosphere at ca. 1.90 Ga, (2) tropical to subtropical weathering at a paleolatitude around 15°, (3) development of a craggy surface environment and "porphyry clasts," (4) deposition of quartz arenite of the Conjuror Bay Formation, (5) diagenesis of the Conjuror Bay Formation quartz arenite, which introduced K_2O, Ba, and Rb into the weathering profile and converted the clay-altered plagioclase phenocrysts to sericite, and finally (6) greenschist grade metamorphism where chlorite replaced ferromagnesian minerals.

The relative timing of K-metasomatism in relation to low-grade regional metamorphism is difficult to determine. Based on textural evidence preserved in the altered porphyry, K-metasomatism appears to have occurred both prior to and after low-grade regional metamorphism. Sericite is seen replacing the plagioclase phenocrysts and altering the surrounding groundmass. In addition, protracted K_2O-rich groundwater flow along the Hottah granitoid – Conjuror Bay Formation unconformity well after low-grade regional metamorphism could also be responsible for elevated K_2O values.

Conclusions

This study has shown that the Beaverlodge Lake regolith experienced tropical to subtropical weathering conditions at 1.9 Ga. Abundant rainfall and tropical to sub-tropical weathering conditions created a deep weathering profile. Geochemical trends show addition of Al_2O_3, $Fe_2O_3^T$, K_2O, P_2O_5, Ba, and Rb from least-altered to weathered equivalent; decrease in SiO_2, Na_2O, MgO, and Sr, and low and near constant CaO values. Titanium remains constant in the weathering profile. These geochemical trends are similar to other Precambrian regoliths as well as modern regoliths developed on granites. Removal of SiO_2, Na_2O, and Sr are consistent with the destruction of plagioclase

feldspar. Retention of $Fe_2O_3{}^T$ is consistent with a profile that developed after GOE. Depletion of MgO is consistent with the breakdown of ferromagnesian minerals such as biotite and hornblende. Near constant and low values of CaO suggest low initial concentration of CaO in the porphyry. Addition of K_2O, Ba, and Rb by K-metasomatism can be explained by diagenesis of the overlying quartz arenite of the Conjuror Bay Formation. Diagenesis of the Conjuror Bay Formation converted the clay-altered plagioclase phenocrysts to sericite. Greenschist grade metamorphism resulted in ferromagnesian minerals being replaced by chlorite and Fe oxides. The lack of a Ce anomaly in the Beaverlodge Lake regolith suggests removal of the upper oxidized soil zones by erosion. Low atmospheric O_2 conditions at the time of formation of the Beaverlodge Lake regolith was unlikely as other regoliths/paleosols that formed during a similar time show pronounced Ce anomalies.

CHAPTER 4
MESOPROTEROZOIC PAN-CONTINENTAL FLUID FLOW FROM U-Pb AND REE URANINITE SYSTEMATICS IN BEAVERLODGE LAKE, NORTHWEST TERRITORIES

Chapter 4 "Mesoproterozoic Pan-Continental Fluid Flow from U-Pb and REE Uraninite Systematics in Beaverlodge Lake, Northwest Territories" studies the Tatie and Bee U occurrence at Beaverlodge Lake, NT. Through U-Pb uraninite dating by SIMS and REE determination by LA-ICP-MS, it is shown that two types of uraninite mineralization are preserved and they can be correlated to world-class uranium deposits. This manuscript was written and edited by the author, Dr. Yuanming Pan, Dr. Eric Potter, Dr. Mostafa Fayek, and Luke Ootes. It is intended to be submitted for publication in Economic Geology in the coming year.

Abstract

Uranium deposits and prospects are ubiquitous throughout the Paleoproterozoic Great Bear magmatic zone of the Northwest Territories, Canada. At Beaverlodge Lake, the high-grade, low tonnage Tatie uranium deposit occurs at an unconformity between a quartz arenite and underlying feldspar porphyry within the ca. 1.9 Ga Hottah Terrane. The uraninite mineralization at Tatie is of basement-hosted unconformity-type similar to those found in the Paleo to Mesoproterozoic Athabasca Basin, whereas mineralization at the nearby Bee prospect is consistent with synmetamorphic-type mineralization. The timing of mineralization has been constrained by in-situ U-Pb uraninite geochronology using secondary ion mass spectrometry (SIMS). The SIMS results, while variably discordant, yield an upper intercept age 1370.2 ± 7.9 Ma for Tatie and 407 ± 21 Ma for Bee. In-situ laser ablation inductively coupled plasma mass spectrometry (LA-ICP-MS) analyses highlight that the ca. 1370 Ma uraninite is LREE depleted relative to HREE with an overall asymmetric bell-shaped, chondrite-normalized REE pattern centered on Tb to Er. The ca. 407 Ma uraninite at Bee is characterized by low La concentrations and a flat to slightly negative chondrite-normalized REE pattern. While the Athabasca-age equivalent strata are now eroded at Beaverlodge Lake, the data indicate that the equivalent of this basin and fluid related to unconformity-related mineralization cycled through the basement. The younger Devonian age at Bee may reflect meteoric fluid cycling and uranium remobilization during the Phanerozoic basin evolution of the overlying Western Canada Sedimentary Basin. The implications of this study are twofold: 1) A large extensive Mesoproterozoic basin existed across the basement of the western Canadian Shield and uranium mineralization was related to fluid flow at the base of this basin and 2) the region should be considered as prospective for future exploration for basement-hosted, unconformity-related uranium mineralization.

Introduction

Uranium is one of the world's most important energy sources. World-class uranium deposits can be divided into the following groups: unconformity-related deposits, sandstone hosted, intrusive, metasomatic, IOCG/breccia, vein-type, roll-front, and volcanic-hosted (Kyser and Cuney, 2009). Unconformity-related deposits constitute about 33% of the western world's uranium resource (Jefferson et al., 2007) and have been studied extensively. Type examples include the deposits in the Paleo through Mesoproterozoic Athabasca and Thelon Basins in Canada (Figure 4.1), Nabarlek and Ranger in Australia, and Karku in Russia (Jefferson et al., 2007).

The Athabasca Basin has been used to create genetic models for the formation of unconformity-type uranium and serves as a point of reference to which other basins are compared (Kyser and Cuney, 2009). These genetic models are based on mineral chemistry, mineral assemblages, and fluid rock interactions (e.g. Hoeve and Sibbald, 1978; Hoeve and Quirt, 1984; Kotzer and Kyser, 1995; Fayek and Kyser, 1997; Alexandre et al., 2005; Kyser and Cuney, 2009). Despite their status as a point of reference, the Athabasca Basin and the U deposits still have many unanswered questions. Among them are the timing of primary U mineralization, the source of U, the precipitation and deposition mechanism for U, and the extent of U mineralization.

Uranium occurrences and prospects are common throughout the Paleoproterozoic Great Bear magmatic zone (GBmz) and Wopmay orogen. They have been proposed to represent a diverse range of deposit types including polymetallic deposits, five-element vein, quartz stockwork hosted U, and iron oxide-copper-gold (IOCG; Ootes et al., 2013). Significant deposits include past-producers such as Rayrock in the south and Port Radium – Echo Bay (Eldorado, Echo Bay, El Bonanza, and Contact) and Camsell River region (Terra and Norex) in the north.
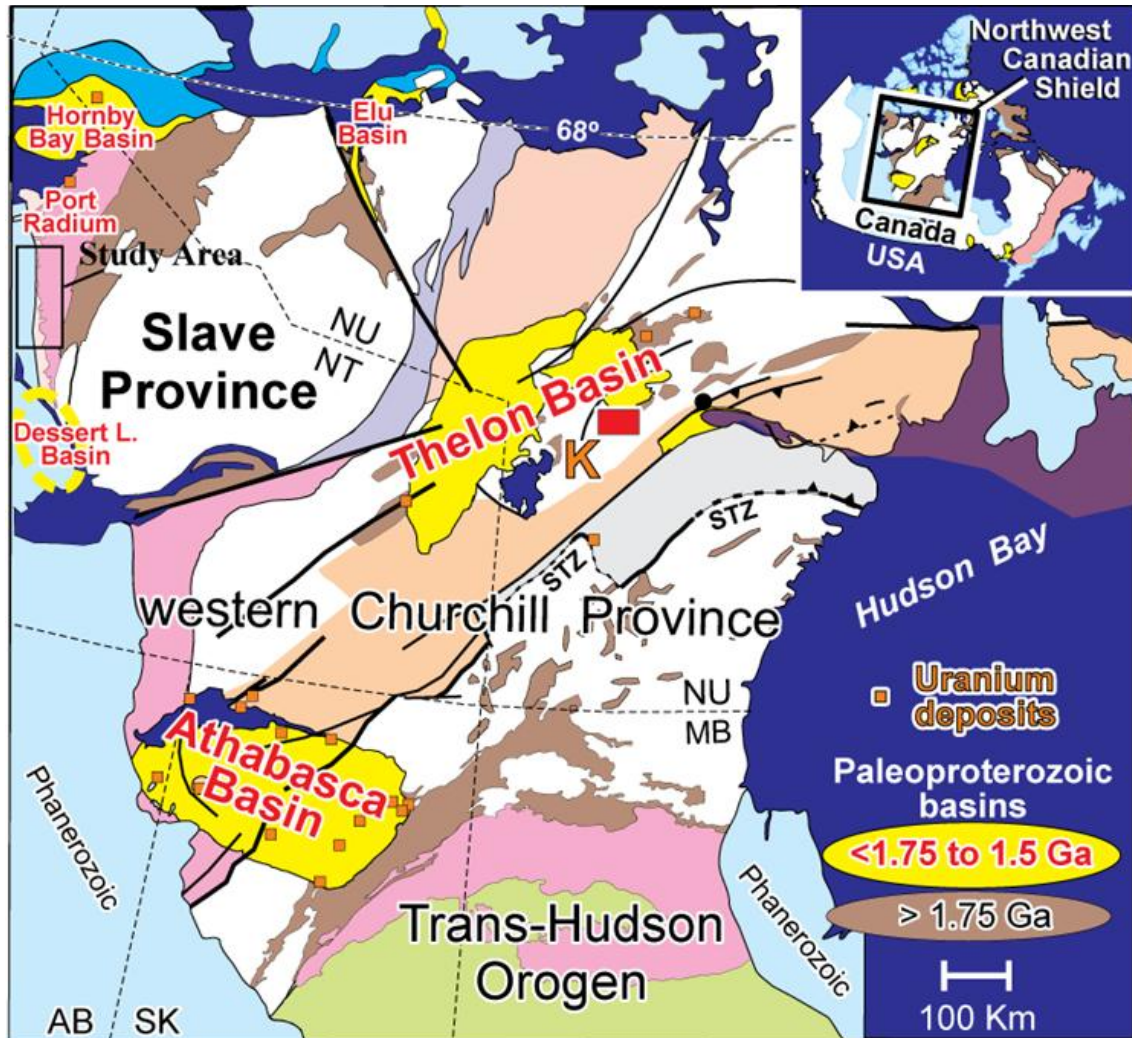
Figure 4.1 Distribution of major tectonic domains in the northwestern Canadian Shield as well as Paleoproterozoic sedimentary basins including the Athabasca and Thelon Basins. Highlighted are the Wopmay Orogen and Great Bear Magmatic Zone. (Modified after Jefferson et al., 2013).

At Beaverlodge Lake, NT, the Bee propect and past-producing Tatie deposit have been investigated in this study. Petrography, electron microprobe analysis (EMPA), *in-situ* secondary ion mass spectrometer (SIMS) and laser ablation inductively coupled plasma mass spectrometry (LA-ICP-MS) suggest that the uranium mineralization at Bee and Tatie are typical of synmetamorphic and basement-hosted unconformity-type, respectively. In particular, age data and REE patterns from uraninites allow the Tatie U deposit to be correlated to other world-class uranium deposits preserved throughout

54

northern Canada. The results of this study suggest Mesoproterozoic Pan-continental fluid flows in Northwestern Canada.

Uranium mineralization and Local Geology

Uranium mineralization in the GBmz

Within the Wopmay orogen of northwestern Canada, most of the known U mineral deposits and showings are hosted in the GBmz (Figure 4.2). The U deposits and showings types found in the GBmz include Ni-Co-As-Ag-Bi ± U five element veins, IOCG ± U, and late giant quartz vein hosted mineralization (Badham et al., 1975; Robinson and Ohmoto, 1973; Changkakoti et al., 1986; Goad et al., 2000; Gandhi, 2000; Corriveau et al., 2007; Mumin et al., 2007; Byron, 2010; Ootes et al., 2013).

There are several past producing U deposits in the GBmz including the Echo Bay – Port Radium region and Rayrock. Prior to production from the Elliot Lake quartz pebble conglomerate and Athabasca Basin unconformity-related deposits, the Echo Bay – Port Radium region was seen as Canada's most important uranium producer from 1931 to 1989 (Badham, 1975; Reardon et al., 1992; Mumin et al., 2007) and it produced over 15,000,000 lbs. of U_3O_8 and ~32,000,000 oz Ag. Mineralization was hosted in quartz and carbonate veins and is associated with shear zones in basement rock units (Reardon, 1992). Recent re-examination of the Contact Lake Belt area has identified widespread IOCG-like polymetallic mineralization similar to that in NICO and Sue-Dianne in the southern GBmz (Mumin et al., 2007). At Rayrock, stockwork quartz veins and breccia fillings containing U were mined during Canada's first uranium boom in the 1950s and produced over 450,000 lbs. of U_3O_8 between 1956 and 1958. The deposit is hosted in a quartz vein, which cuts basement granite and contains variable amounts of sulphides, hematite, and epidote near the main mineralizing zone (Gandhi et al., 2000).

The timing and relationship of the various styles of U mineralization is difficult to constrain (Ootes et al., 2013). Previously, Miller (1982) dated various uraninite grains from a variety of U showings and estimated U-Pb ages ranging from 2058 Ma to 339 Ma. These wide ranges of ages most likely indicate secondary uranium mobilization ages, at

least in some cases. Intrusion related mineralization at one prospect has been dated around 1873 Ma (Ootes et al., 2010a) and the IOCG associated uranium mineralization is contemporaneous with plutonism associated with the Great Bear magmatic zone ca. 1870 Ma (Hildebrand, 1986; Gandhi, 1994; Gandhi et al., 2001; Mumin et al., 2007). Most of the uranium mineralization in the GBmz occurs adjacent to quartz stockwork systems. These stockworks might represent an epithermal stage of a larger IOCG mineralization system or a structural feature used by younger fluids (Mumin et al., 2007; Byron 2010; Ootes et al., 2013).
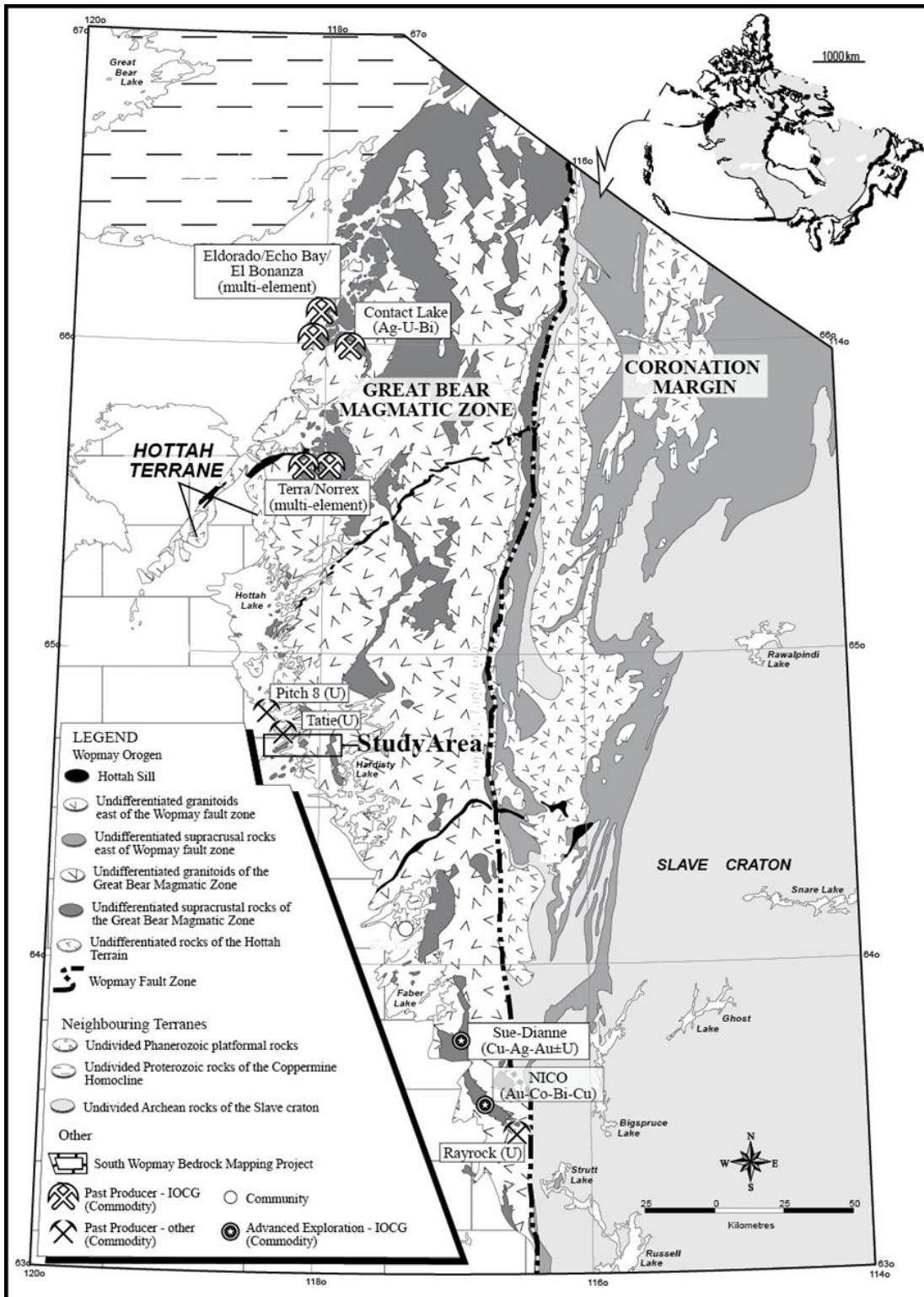
Figure 4.2 Regional geology of the Wopmay Orogen. Various significant past-producing mines and deposits are shown. Study area relevant to this study is shown. (Modified after Ootes et al., 2013).

57

Geology of the Study Area

Beaverlodge Lake is 100 km south of Great Bear Lake, NT (not to be confused with Beaverlodge Lake, Saskatchewan). At Beaverlodge Lake, there is a prominent 18-km long, NE-SW trending ridge. At the base of the ridge, ca. 1.93 Ga Hottah plutonic complex granite and hypabyssal porphyry are unconformably overlain by both the ca. 1.9 Ga Zebulon Formation volcanic rocks and Conjuror Bay formation quartz arenite and overlying siltstone of the Bell Island Bay Group (Reichenbach, 1991; Jackson and Ootes, 2012; Shakotko et al., 2013). Coincident with the basement porphyry – quartz arenite unconformity is the minor past-producing Tatie U deposit. In addition, there is a well-documented giant quartz vein at Beaverlodge Lake. The giant quartz vein is 25 metres in width and over a kilometer in length (Byron, 2010). The vein is hosted in the quartz arenite and overlying siltstone (Byron, 2010).

Uranium was discovered in the area in 1933. In 1934, D'Arcy Arden and E.H. Hargreaves staked the Tatie and Bee claims (Figure 4.3; Hargreaves, 1935). Pitchblende was found at the surface as a small lense on the Tatie 2 claim. The Tatie 2 claim is on the unconformity between Hottah porphyry and Conjuror Bay quartz arenite. A shaft was sunk where pitchblende was found. Two additional trenches were dug on the Tatie 2 claim with one measuring 13 feet by 13 feet by 10 feet and the second one being 6 feet by 4 feet by 3 feet. Only one and a half tonnes of ore was excavated from Tatie, but this was upwards of 40.5 wt.% U_3O_8 (Henderson, 1949). No pitchblende was found beneath the small lense and work was discontinued after sinking a shaft to a depth of 65 feet plus 60 feet of crosscutting (Hargreaves, 1935). Other showings were discovered and trenched at Beaverlodge Lake, such as at Bee. The Bee claims are located 1.8 km northeast from the Tatie claims and are in the middle of the giant quartz vein. Between 1934 and 1935, about eight trenches were dug on the Bee 3 claim (Kidd, 1936; Henderson, 1949; Byrne and Smith, 1955).
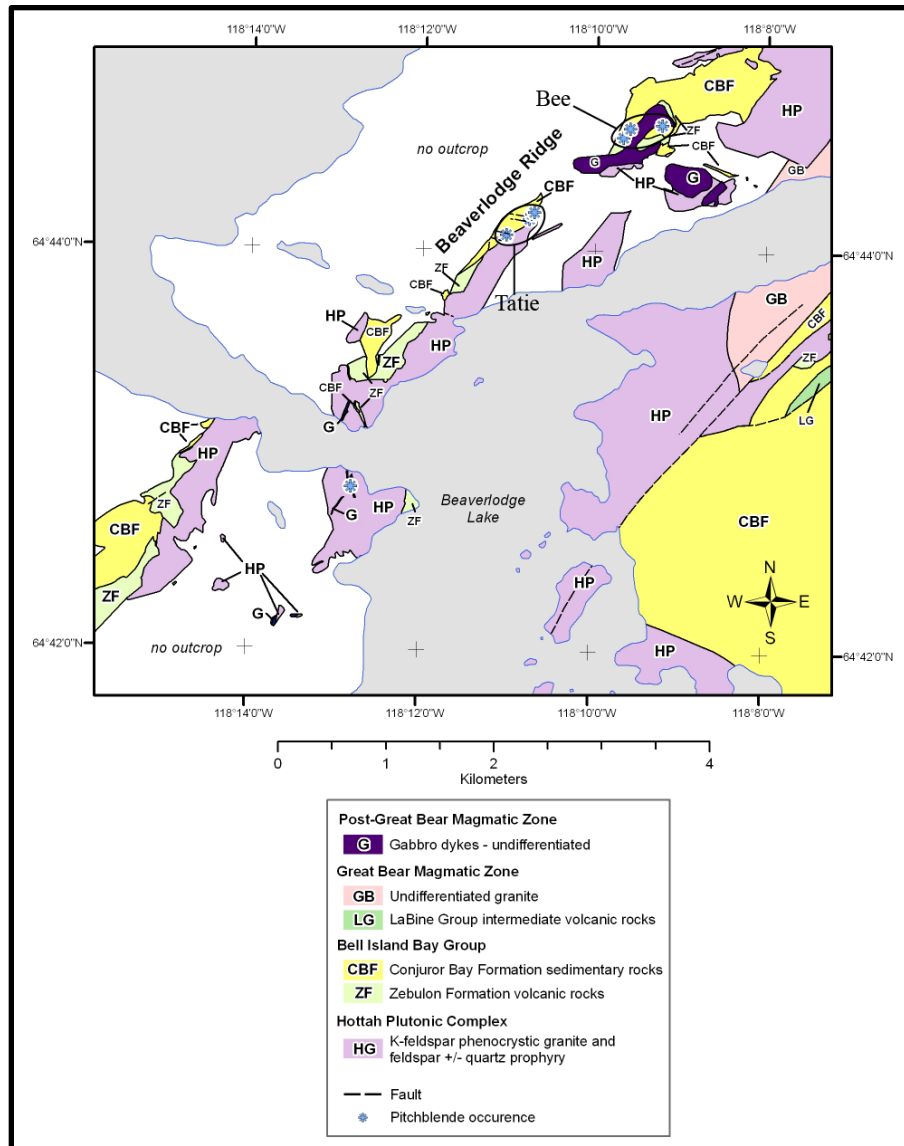
Figure 4.3 Distribution of sequences and uranium occurrences along Beaverlodge ridge. Modified after Henderson (1949), McGlynn (1979), Hildebrand and Roots (1985), and Jackson and Ootes (2012). Highlighted are the Tatie deposit and the Bee showing.

In 1943, the Tatie and Bee claims were re-staked by DeStaffany as part of the Cormac Group, which consisted of 6 claims and later increased to 26. Between 1955 and 1956, an exploration program was undertaken at Beaverlodge Lake on the Cormac Group, which consisted of 2005 feet of drilling and 900 feet of drifting and crosscutting. Two high-grade separate lenses were located during drilling with grades varying from 0.1% of 50.0 wt.% U_3O_8. Both lenses were outlined by 16-diamond diamond drill holes and results are summarized in Appendix C. Grady (1955) documented the occurrence of

pitchblende in open cavities, fracture zones, and at the intersection of fractures. Grady (1955) asserted that intrusion of the "quartz stockwork" relieved stressed more easily near the contact with underlying feldspar porphyry than in the main body of the quartz arenite. Grady (1955) noted that there are more fractures at or near the contact with the underlying feldspar porphyry. All recorded pitchblende showings occur within 50 feet of the contact between quartz arenite and feldspar porphyry. Drill core and geological reports of these claims indicate that pitchblende is associated with abundant hematite and chlorite (Figure 4.4). Other minerals documented include uranophane, limonite, pyrite, cobaltite, and calcite (Grady, 1955). The project was eventually abandoned and allowed to revert back to the Crown.

Between 1965 and 1966, the area was re-staked as the 8 Atom claims by McGuire and 35 Tin Claims by McCormick. Baykal (1967) re-investigated all previous work in the Beaverlodge Lake area and concluded that pitchblende was found intermittently for about 2.5 miles along the Beaverlodge thrust and other shear zones. Ore shoots occur in fractures or brecciated zones. Baykal (1967) noted the association of pitchblende in or near major and secondary faults. Since 2004, the land at Beaverlodge Lake has not been re-staked or leased.

Thirty-eight additional uranium showings are known to occur between Beaverlodge Lake and Hottah Lake and all appear to have a close association between hematite and pitchblende (Henderson, 1949). Between eleven and fifteen showings were discovered during the course of fieldwork by Henderson (the remainder had been discovered by earlier prospectors). Nine out of the 38 showings occur along or near the contact between the volcanic and/or basement porphyry with quartz arenite. Other showings occur along joints associated with gabbro dykes or sill-like bodies that intrude into granitic rocks and two other showings occur in joints and cracks in granite (Henderson, 1949).

Due to the coincidence of the high-grade mineralization at the unconformity and a previously reported ca. 2.05 Ga U-Pb age for uraninite at Tatie (Miller, 1982), a working

hypothesis suggested that uranium mineralization at Tatie was related to the development of the ca. 1.9 Ga unconformity (Ootes et al., 2010b). The age data from this study suggest that this initial hypothesis was probably incorrect.
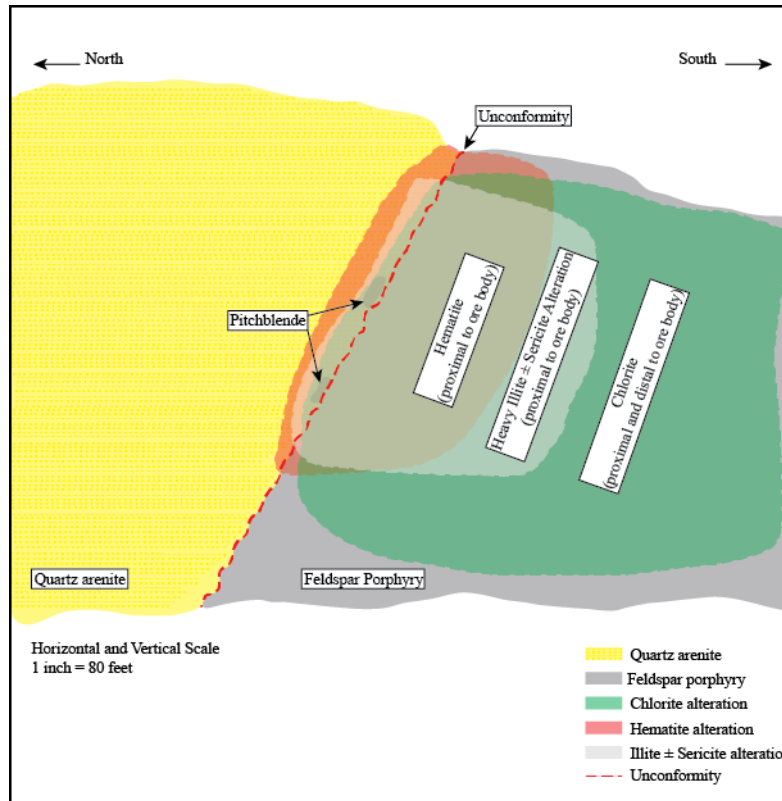
Figure 4.4 Simplified cross-section depicting the location of the Tatie deposit. Cross-section shows lithology and alteration mineralogy. View is looking east and scale is 1 inch = 80 feet. North and south arrows are shown (Modified from Baykal, 1967)

Results

Petrography

Uraninite grains from sample A1090 (from Bee) vary from slightly to heavily fractured. Filling the heavily fractured uraninite grains in this sample are abundant late chlorite, iron oxide, and quartz veins as well as minor secondary coffinite (Figure 4.5.A).

Sample 12ps4 (from Bee and collected in the giant quartz vein) contains abundant and multiple generations of quartz with minor chlorite and sericite. Sample 12ps4 was barren of uraninite.

61

Sample A1709 (from Tatie) preserves botryoidal uraninite, which is typically less than 1 mm in diameter, with secondary coffinite, cobaltite, iron-rich magnesite, calcite, and minor chalcopyrite.

Sample 12ps1 (from Tatie) consists primarily of quartz, chlorite, Fe oxides, Ti oxides, and very fine-grained disseminated (< 1 μm) uraninite. The disseminated uraninite grains are often associated with chlorite and often occur as very fine-grained clumps.

Sample A1092 (from Tatie) contains quartz and abundant late Fe oxide veins.

Sample A1094 (from Tatie) contains heavily altered plagioclase feldspar phenocrysts completely replaced by illite, quartz phenocrysts, chlorite replacing Fe-Mg minerals and as veins, and minor Fe oxides, Fe-Ti oxides, and Ti oxides. Titanium oxides are frequently cut by late chlorite veins. Samples A1092 and A1094 are barren of uraninite.

Alteration in samples A1090 (from Bee) and A1709 (from Tatie) is visible along grain boundaries and fractures. Coffinite in both samples occurs along the rims or in fractures of the uraninite as stringers or masses. Cobaltite and carbonate minerals in the Tatie sample tend to occur as small fine-grained masses in the core or between uraninite botryoides (Figure 4.5.B).

Samples from Bee (A1090) and Tatie (A1709) have uraninite grain sizes amenable to microbeam analyses whereas the other samples (12ps1, 12ps4, A1092, and A1094) were either barren of uraninite or uraninite was too fine-grained and disseminated for microbeam analysis. The paragenetic sequence of mineralization at Tatie is summarized in Figure 4.6.
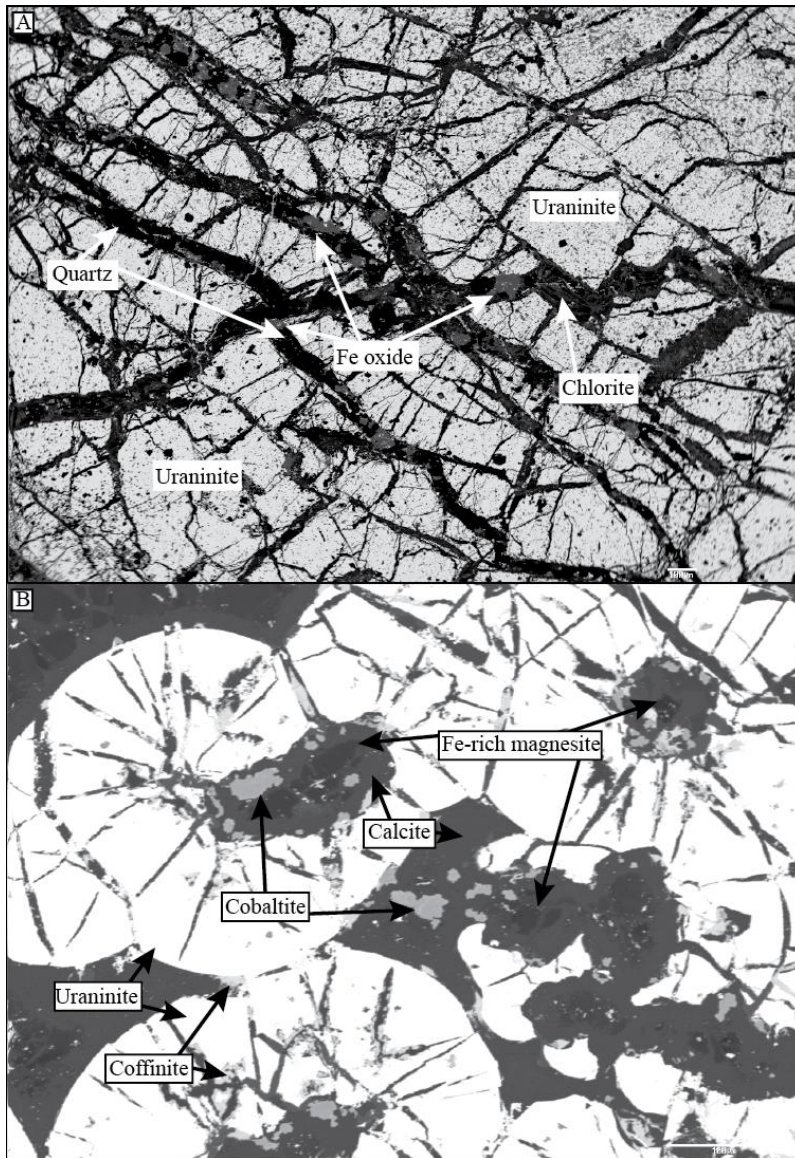
Figure 4.5 Backscattered electron image of uranium bearing minerals and alteration minerals including: uraninite, coffinite, iron-rich magnesite, calcite, and cobaltite from samples A) Bee and B) Tatie.

Electron microprobe analysis (EMPA)

Uraninite grains from Bee (A1090) shows variation in U content from 75 to 81 wt.%, whereas the Pb content varies from 3 to 4 wt.% (Appendix D). Older generations of uraninite, such as those found in the sample from Tatie (A1709), have lower concentrations of U between 68 and 72 wt.%; however, they have higher concentrations of Pb between 15 and 18 wt.%. Thorium, Mg, Al, and P contents in both samples are all ≤0.2 wt.%. The concentrations of Si, Fe, and Y in uraninite of both samples are all close

to their respective detection limits. Uraninite grains from Bee appears to be slightly more heterogeneous than its counterpart in the sample from Tatie.

From the EMPA data, chemical U-Th-Pb ages were calculated from uraninite grains from Bee (A1090) and from Tatie (A1709). Two assumptions were made before calculating the chemical U-Th-Pb ages. Firstly, Pb present in uraninite is assumed to be all radiogenic Pb without any ^{204}Pb ("common Pb"; Bowles, 1990). Secondly, it is assumed that the U-Pb system has remained closed since the formation of the uraninite grain (i.e. no gain or loss of U, Th, or Pb; Bowles, 1990). Three chemical U-Th-Pb formulas were used and yielded a wide range of ages from 1692 Ma to 324 Ma (Appendix D).

The first method (Method 1; Equation 4.1) is a simple approximation of the age where:

$$t_{(Ma)}(Ma) = Pb(wt.\%) \times 100 \qquad \text{(Equation 4.1)}$$

as noted by Bowles (1990). Method 1 ages from Bee range from 313 Ma to 419 Ma. The range for the sample from Tatie is 1471 Ma to 1855 Ma.

The second data treatment (Method 2; Equation 4.2) uses the following formula:

$$t = \lambda_1^{-1} \ln \left[\left(\frac{1.104Pb}{U} \right) + 1 \right] \qquad \text{(Equation 4.2)}$$

where Pb and U are expressed in weight percentages and $\lambda_1^{-1} = \dfrac{1}{0.000155125}$. Method 2 ages from Bee range from 287 Ma to 347 Ma. The age range for Tatie samples is 1363 Ma to 1598 Ma. Method 3 (Equation 4.3; Ranchin 1968 as in Bowles, 1990) is:

$$t = \frac{Pb \times 7550}{(U + 0.36Th)} \qquad \text{(Equation 4.3)}$$

where Pb, U, and Th are also expressed in weight percentages and age is expressed in Ma. Method 3 ages from Bee range from 305 Ma to 414 Ma while Tatie sample range from 1610 Ma to 1925 Ma. Bowles (1990) noted that Method 3 (Ranchin's (1968) formula) yielded ages that are too old for samples greater than 200 Ma. Error was estimated as 5% of Pb analyses (Bowles, 1990). Analyses of Bee and Tatie uraninite

grains revealed little Th and therefore the contribution of thorogenic Pb was deemed negligible.

Quantitative EMPA were undertaken on the alteration mineral coffinite $(USiO_4)_{1-x}$ $(OH)_{4x}$ found in the sample from Tatie (A1709; Appendix E). Coffinite analyses focused along grain boundaries with botryoidal uraninite. Coffinite Si values range from 0.9 to 6 wt.%. Coffinite Fe and Ca concentrations are above detection limits and most likely represent inclusions of chlorite and/or carbonate in the coffinite. Compared to the unaltered botryoidal primary uraninite, coffinite analyses show elevated levels of Si (3.6 compared to 0.07 wt.%), Fe (1.9 compared to 0.1 wt.%), and Ca (1.92 compared 0.54 wt.%). However, coffinite has less U (66.8 compared to 70.7 wt.%) and Pb (3.1 compared to 16.8 wt.%) than the least-altered primary uraninite. The presence of coffinite along grain boundaries with primary uraninite and low Pb content suggests later remobilization of U.

Quantitative analyses of carbonate minerals in the sample from Tatie (A1709) revealed two distinctive phases: calcite and iron-rich magnesite (Appendix F). Calcite Ca wt.% values are between 31.74 to 33.19 wt.%. Trace amounts of Mg, Fe, and Mn are also identified. Iron-rich magnesite also contains elevated Mg contents, with values upwards of 22.43 wt.% Mg and 17.66 wt.% Fe. Trace amounts of Ca and Mn were also detected in the iron-rich magnesite. Carbonate minerals were identified in the core, fractures, and outside the botryoidal uraninite, indicating a later alteration event.

Mineral	Stage		
	Pre-ore	Ore	Post-ore
Illite (alteration of plagioclase)	▬▬▬		
Chlorite (alteration of Fe-Mg minerals)	▬▬▬		
Uraninite		▬▬▬	
Carbonates			▬▬▬
Cobaltite			▬▬▬
Coffinite			▬▬▬

Figure 4.6 General mineral paragenesis sequence of the Tatie U showing. Three stages are recognized pre-ore, syn-ore, and post-ore

SIMS U-Pb uraninite geochronology

Samples from the Tatie (A1709) deposit and Bee (A1090) showing were analyzed by Secondary Ion Mass Spectrometry (SIMS) at the University of Manitoba. Analytical techniques are in Appendix A and results are presented in Table G.1 and Figure 4.7 Uraninite grains from Bee are moderately to strongly discordant, with a best-fit discordia line yielding an upper intercept of 407 ± 21 Ma and a lower intercept of -72 ± 28 Ma (MSWD = 1.7; Figure 4.7.A; Appendix G). Uraninite grains from Tatie are also moderately to strongly discordant. A best-fit discordia line yields an upper intercept of 1370.2 ± 7.9 Ma and a lower intercept of 12 ± 15 Ma (MSWD = 1.05; Figure 4.7.B; Appendix G).
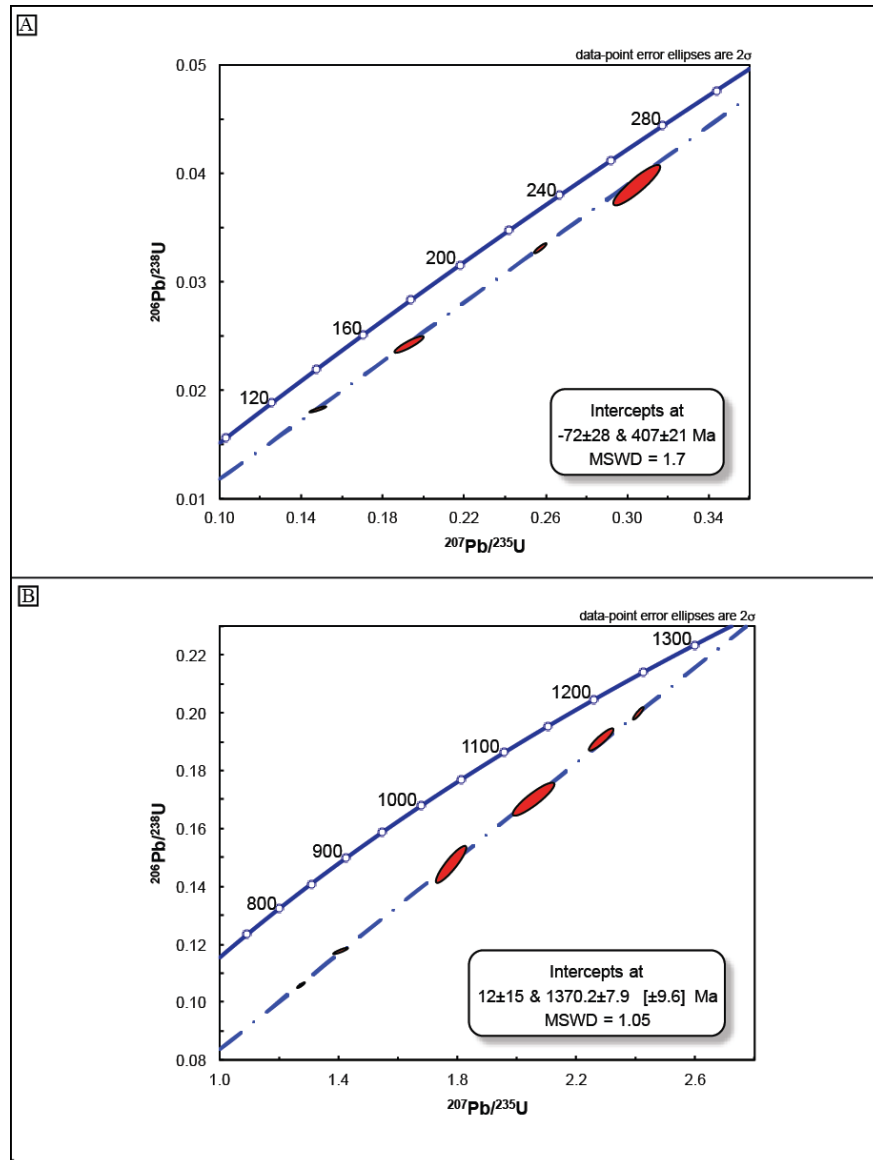
Figure 4.7 U-Pb results from in situ isotopic analyses of A) Bee and B) Tatie.

Laser ablation inductively coupled plasma mass spectrometry (LA-ICP-MS)

The uraninite grains that were dated were subjected to LA-ICP-MS in order to determine REE contents at the Geological Survey of Canada. Analytical techniques are in Appendix A and results in Table H.1 and Figures 4.8 and 4.9. While ablating the uraninite grains, Co-Ni-Fe-As rich zones were discovered in the uraninite (inclusions of cobaltite). One dataset containing the average values during the entire ablation period is presented (Appendix H).

Figure 4.8 plots the chondrite-normalized REE concentrations of uraninite grains from Bee (A1090) and from Tatie (A1709). The samples show different REE patterns, consistent with the notion that they represent different styles of U mineralization. Mercadier et al. (2011) suggested the fractionation of REEs into uraninite is complex and is a function of multiple factors including: crystallographic controls, temperature of ore formation, nature of mineralizing fluid (salinity of the fluid), and source of the REEs therefore different REE patterns might reflect different mineralizing styles. Chondrite-normalized REE patterns of uraninite grains from Bee are characterized by low La concentrations and a flat to slightly negative slope. It is enriched in light rare earth elements (ΣLREE = La to Eu) as opposed to heavy rare earth elements (ΣHREE = Gd to Lu). The average ΣLREE$_N$/ΣHREE$_N$ ratio for uraninite grains from Bee is 1.3. Uraninite from Tatie displays an asymmetric bell-shaped, chondrite-normalized REE pattern. The bell-shaped pattern is centered on Tb to Er then is negatively sloped, reflecting depletion in LREE relative to HREE. The average ΣLREE$_N$/ΣHREE$_N$ ratio for uraninite from Tatie is 0.3. Mercadier et al. (2011) suggested that below 350 ℃, total REE decreases and fractionation occurs. As a result, crystallographic controls dominate and uraninite incorporates REEs with ionic radii close to U^{4+} (Tb-Er) thus resulting in a "bell-shaped" pattern centered on Tb to Er. Uraninite grains from both Bee and Tatie exhibit small negative Eu anomalies suggesting reducing conditions during precipitation of uranium oxides (Mercadier et al., 2011). The size of the negative Eu anomaly, Eu/Eu*, ranges from 0.488 to 0.524 for the sample from Bee and 0.527 to 0.544 for the sample from Tatie.
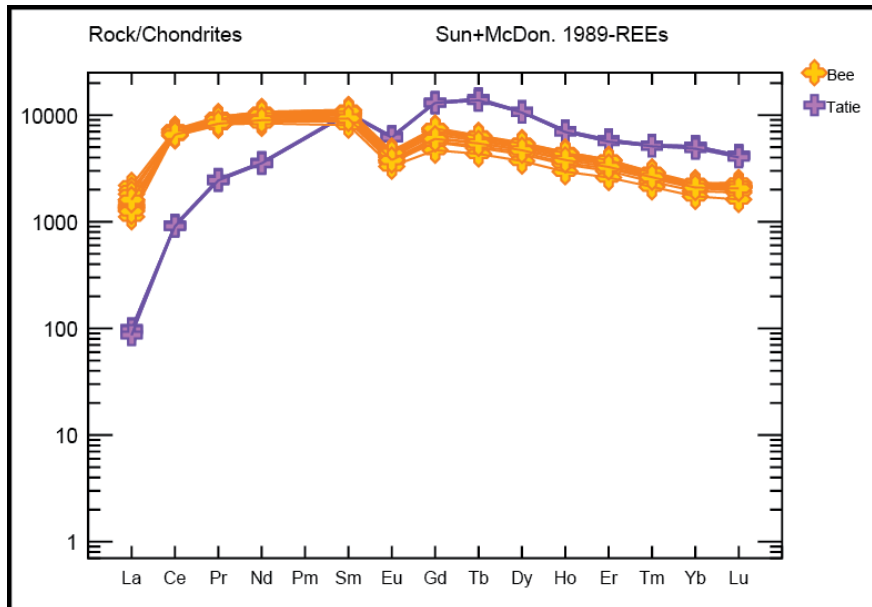
Figure 4.8 REE patterns for samples A1090 from Bee and A1709 from Tatie. See text for discussion. Samples are normalized to chondrites from Sun and McDonough (1989).

Discussion

Comparison of Tatie and Bee to Athabasca and Mistamisk

The Athabasca Basin hosts a number of major U deposits including Key Lake, Collins Bay, Millennium, McArthur River, Cigar Lake, Cluff Lake, Eagle Point, and Rabbit Lake (Kyser and Cuney, 2009). The Athabasca Group, which makes up the basin fill, consists of quartz-rich sandstone and conglomerate and has been interpreted as fluvial and near-shore to shallow shelf (Ramaekers, 1990; Ramaekers et al., 2007). The basement of the Athabasca Basin is comprised of Archean to Early Proterozoic granitoids and graphitic metapelites (Annesley et al., 2005; Kyser and Cuney, 2009). Uranium mineralization typically consists of massive to semi-massive lenses, pods, veins, or breccias in either basement or the overlying sandstone units (Jefferson et al., 2007).

In general, two sub-types of U deposits have been identified: (1) simple, composed primarily of uraninite and (2) complex, containing uraninite plus other sulfides and arsenides (Hoeve and Quirt, 1984; Wallis et al., 1983; Wallis et al., 1985; Reyx and Ruhlmann, 1993). Ore bodies in the Athabasca Basin can range from purely sandstone-

69

hosted to basement-hosted (Hoeve and Quirt, 1984; Wallis et al., 1983; Wallis et al., 1985; Reyx and Ruhlmann, 1993). Basement-hosted deposits are primarily simple type and the uraninite ore can be found in faults and fractures (Kyser and Cuney, 2009). Sandstone-hosted U deposits are associated with Ni, Cu, Co, Pb, Zn, and Mo sulfides (Kyser and Cuney, 2009).

Alteration minerals associated with unconformity-type deposits varies between deposits (Hoeve and Quirt, 1984). In general, the alteration halos are zoned and have been divided into pre-ore stage, ore stage, and post-ore stage alteration. In sandstone-hosted deposits, pre-ore alteration is dominated by diagenesis and hydrothermal (Alexandre et al., 2009). Diagenesis consists of hematite, kaolinite, dravite, desilification, and illite. Post-ore alteration consists of kaolinite, dravite, pyrite, and minor amonnts of copper, nickel, and cobalt sulphides (Alexandre et al., 2009). In basement-hosted deposits, earliest alteration involves illitization of feldspar and alteration of biotite to chlorite. Post-ore alteration includes vein chlorite, euhedral quartz, dravite, dolomite, and rare kaolinite with rare pyrite, rutile, chalopyrite, bornite, pentlandite, cobaltite, and magnetite (Alexandre et al., 2009). Several fluid models have been developed to explain the precipitation of U including fluids mixing at the unconformity (egress-style) and fluid-rock interaction (ingress-style). Fluids from the overlying Athabasca Group were said to be oxidizing and contained the U; while the fluids from the basement were reducing (Hoeve and Quirt, 1984; Jefferson et al., 2007).

Dating of uraninite can be very complicated. Uraninite readily recrystallizes at low temperatures and as a result it releases some or all the radiogenic Pb it has accumulated (Fayek and Kyser, 2000; Alexandre and Kyser, 2005). In addition, diffusion rate in uraninite is rapid and also results in Pb loss (Kotzer and Kyser, 1993; Janeczek and Ewing, 1995; Sharpe, 2013). The susceptibility of uraninite to recrystallize and the rapid diffusion rates make it very unusual to obtain concordant U-Pb ages.

The timing of U mineralization in the Athabasca Basin is a complex issue. Post-peak metamorphic cooling during the Trans-Hudson Orogen gives a maximum age of

basin formation at ca. 1750 Ma (Armstrong and Ramaekers, 1985; Rayner et al., 2003; Alexandre et al., 2009). $^{40}Ar/^{39}Ar$ dating of pre-ore illite and chlorite suggest diagenesis began at ca. 1675 Ma (Alexandre et al., 2009; Kyser and Cuney, 2009). $^{40}Ar/^{39}Ar$ dating of syn-ore illite at McArthur River and Dawn Lake deposits vary from 1277 Ma to 1583 Ma (Alexandre et al., 2009). LA-ICP-MS U-Pb dating of uraninite at McArthur River demonstrates that the main U mineralization occurred at ca. 1540 (Alexandre et al., 2009; Kyser and Cuney, 2009). In situ U-Pb uraninite dating at Cigar Lake, McArthur River, and Sue Zone U deposits indicate they formed ca. 1500 Ma (Fayek et al., 2000, 2002). As previously discussed, uraninite is highly susceptible to alteration by subsequent fluid events, including Pb loss due to diffusion (Kotzer and Kyser, 1993; Janeczek and Ewing, 1995; Sharpe, 2013). Therefore caution is required when interpreting uraninite U-Pb data. Uraninite U-Pb ages are often better interpreted as Pb-loss events. For example, uraninite ages and therefore Pb-loss events from the Athabasca Basin are consistent with continental-wide tectonic events such as Mazatzal Orogeny (ca. 1.6 to 1.5 Ga), the Berthoud Orogeny (ca. 1.4 Ga), the Mackenzie mafic dyke swarm (ca. 1.27 Ga), the Grenville Orogeny (ca. 1.1 Ga), and the assembly and break-up of Rodinia (ca. 1 to 0.85 Ga) (Alexandre et al., 2009; Kyser and Cuney, 2009).

At Tatie, the presence of high-grade pitchblende lenses associated with hematite, chlorite, and illite, and the occurrence of pitchblende at or near the unconformity between feldspar porphyry and quartz arenite, suggests that the style of U mineralization here is similar to that found in the Athabasca Basin. However, the bedrock exposure preserved at Beaverlodge Lake significantly pre-dates the Athabasca strata.

Chondrite-normalized REE concentrations in uraninite from Tatie are similar to those reported by Mercadier et al. (2011) for the Eagle Point and Millennium deposits (Figure 4.9.B). Figure 4.9.C plots chondrite-normalized REE concentrations of uraninites from Tatie and Cigar Lake. Both basement-hosted and unconformity-type uraninites display an asymmetric "bell-shaped" pattern centered on Tb to Er (Mercadier et al., 2011). Both basement-hosted and unconformity-type uraninites show a decrease towards

HREE and a negative Eu anomaly. Although uraninites from Tatie have greater REE concentrations, the overall pattern appears similar.

When comparing uraninites from Tatie to basement-hosted uraninites such as those from Eagle Point and Millennium, the average $\Sigma LREE_N/\Sigma HREE_N$ ratio for uraninite from Tatie is 0.364, compared to 0.176 for those from Eagle Point and 0.125 for those from Millennium. The slope of the REE pattern, La_N/Yb_N, for uraninites from Tatie sample is 0.019, 0.007 for Eagle Point, and 0.019 for Millennium. When comparing uraninites from Tatie to unconformity-type uraninites such as those from Cigar Lake, the average $\Sigma LREE_N/\Sigma HREE_N$ ratio for uraninite from Cigar Lake is 0.186 and 0.364 for Tatie. The La_N/Yb_N for Cigar Lake is 0.063 and 0.019 for Tatie.

Figure 4.10 plots La_N/Sm_N versus Dy_N/Lu_N for Tatie, Eagle Point, Millennium, and Cigar Lake. Tatie, Eagle Point, Millennium, and Cigar Lake have a low La_N/Sm_N ratio compared to Dy_N/Lu_N. While the average La_N/Sm_N ratio for Tatie is 0.009 compared to 0.008 from Eagle Point and 0.023 from Millennium, the average Dy_N/Lu_N ratio for Tatie is 2.125, 2.777 for uraninites from Eagle Point and 3.262 from Millennium. The average La_N/Sm_N ratio for Cigar Lake is 0.067 compared to 0.009 for uraninites from Tatie; while the average Dy_N/Yb_N ratio for Cigar Lake is 3.388 compared to 2.125 for uraninites from Tatie.

The 1370.2 ± 7.9 Ma U-Pb isotopic age and the less precise microprobe chemical U-Pb age of ca. 1567 Ma for uraninite from Tatie are similar to a Pb-loss event dated at 1400 Ma and attributed to far-field effects of the Berthoud Orogeny. This Pb-loss event has been interpreted to affect geochronology in the Athabasca Basin (Alexander et al., 2005; Alexandre et al., 2009; Kyser and Cuney, 2009). The 1370.2 ± 7.9 Ma age could represent a primary mineralization age; however due to the susceptibility of uraninite to be isotopically reset, the presence of both fractured uraninite and coffinite, it is possible that the ca. 1370 Ma age may not be the primary mineralization age at Tatie. Based on the above, the ca. 1370 Ma age from Tatie is interpreted to represent a reset age on older material.

After considering the texture, mineralogy, REE patterns, and age data, it is reasonable to suggest that the processes that formed the Tatie deposit are related to those observed in the Athabasca Basin; however, the Athabasca age equivalent stratigraphy at Beaverlodge Lake is now eroded. While the geology preserved at Beaverlodge Lake suggests an intriguing option for primary mineralization age, the results of this study suggest that U mineralization was not related to the formation of the 1.9 Ga unconformity. They do suggest however that whatever process reset the uraninite at ca. 1370 Ma was acting on a large scale and is also recorded in the Athabasca Basin. Mineralization, although preserved in an older unconformity, was related to younger (Mesoproterozoic) unconformities (now eroded) and is discussed below.
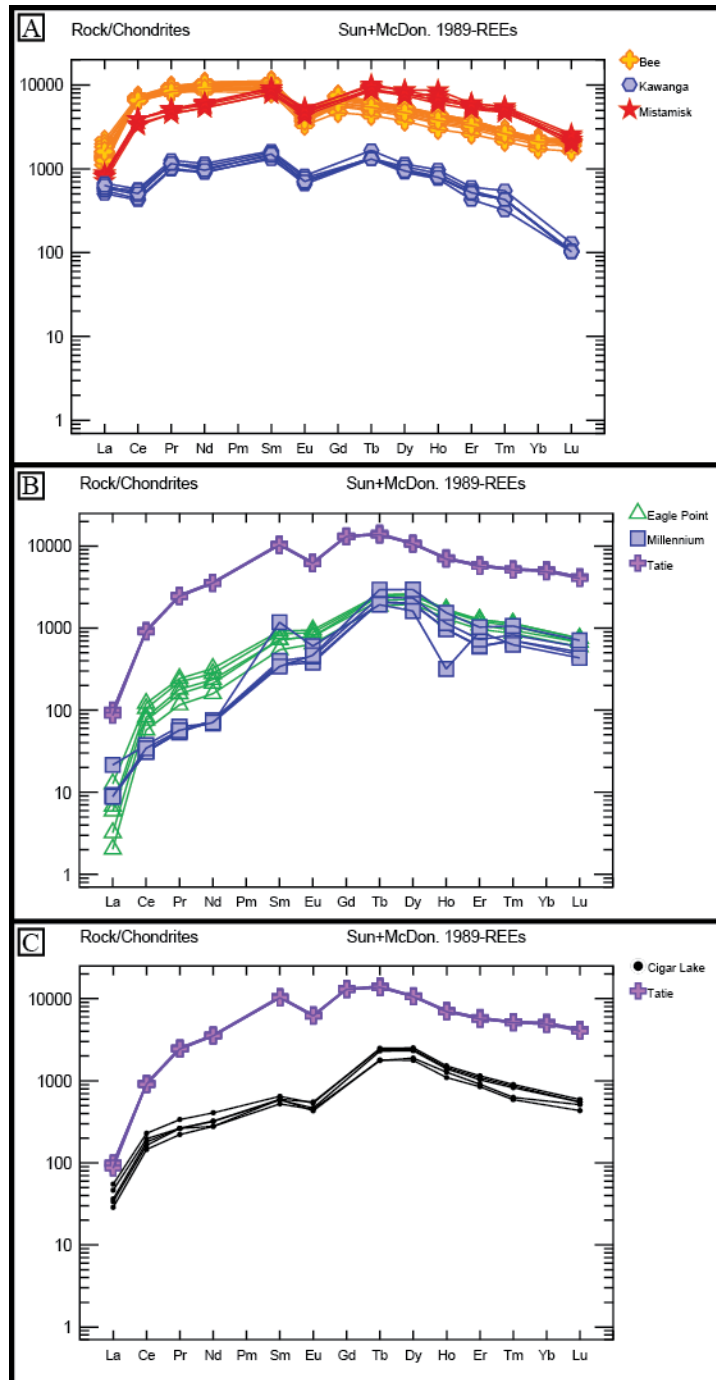
Figure 4.9 REE patterns for samples A) Bee, Kawanga and Mistamisk, B) Tatie, Eagle Point and Millennium, and C) Tatie and Cigar Lake. See text for discussion. Samples are normalized to chondrites from Sun and McDonough (1989). Kawanga, Mistamisk, Eagle Point, Millennium, and Cigar Lake data can be found in Mercadier et al. (2011).

Chondrite-normalized REE patterns of uraninite from Bee are also similar to values reported by Mercadier et al. (2011). Rare earth element concentrations in

uraninite, normalized to chondrite values, are plotted for samples from Bee, Mistamisk, and Kawanga (Figure 4.9.A). Both Mistamisk and Kawanga are currently defined as synmetamorphic U deposits. Chondrite-normalized REE patterns in uraninites from Bee, Mistamisk, and Kawanga exhibit low La concentrations and a rather flat to slightly negative slope REE pattern with a small negative Eu anomaly. The average $\Sigma LREE_N/\Sigma HREE_N$ ratio for uraninite from Bee is 1.3 whereas this ratio for uraninite from Mistamisk is 0.576 and 0.908 for Kawanga. The average La_N/Yb_N ratio for Bee is 0.708, 0.221 for Mistamisk, and 2.203 for Kawanga. The average La_N/Sm_N ratio for Bee is 0.155 compared to 0.094 from Mistamisk and 0.402 from Kawanga. The average Dy_N/Lu_N ratio for Bee is 2.296 and 2.175 for uraninites from Mistamisk and 3.726 from Kawanga (Figure 4.10). This supports the previous observation of low concentrations of La_N relative to HREE. The age of 407 ± 21 Ma and average microprobe ages of 348 Ma from Bee could represent meteoric fluid cycling and U remobilization along the Phanerozoic – Precambrian unconformity. In fact, this unconformity is well-preserved on the southwest side of Beaverlodge Lake (Henderson, 1949; Jackson and Ootes, 2012).

At Mistamisk, uraninite-albite veins occur in the argillite member of the Dunphy Formation (Kish and Cuney, 1981). Other minerals documented in the uraninite-albite veins include chlorite, dolomite, and minor amounts of quartz, tellurides, sulphides, gold, and organic material (Kish and Cuney, 1981). Temperature and pressure of vein formation from fluid inclusion data yielded homogenization temperatures between 300 º - 350 ºC and pressures around 2.5 kbar (Kish and Cuney, 1981). Based on the above, the interpretation of a synmetamorphic origin for U at Bee seems highly unlikely.

Previously, Byron (2010) determined homogenization temperatures values for the giant quartz vein at Beaverlodge Lake and obtained temperatures ranging from 150 º to 250 ºC below the temperatures determined at Mistamisk. As previously discussed, uraninite in Bee is associated with a quartz stockwork vein. Quartz stockwork veins in the GBmz occur near U mineralization and are interpreted to represent an epithermal stage in a larger IOCG-like mineralization system. Mineralization at Bee could represent a larger IOCG-like mineralization system.
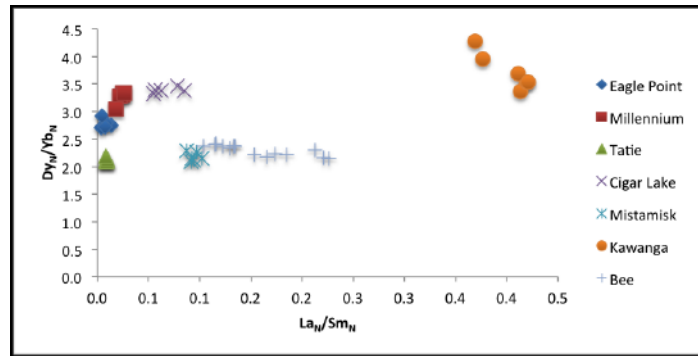
Figure 4.10 La_N/Sm_N versus Dy_N/Yb_N for sample Bee, Kawanga, Mistamisk, Tatie, Eagle Point, Millennium, and Cigar Lake (Rare earth element data for Mistamisk, Kawanga, Eagle Point, Millennium, and Cigar Lake from Mercadier et al., 2011).

Comparison of Tatie and Bee to other uranium showings in the GBmz

Uranium mineralization in GBmz can be classified into four distinct categories: magmatic U mineralization, IOCG and affiliated systems, quartz veining, and secondary U mineralization in fractures (Ootes et al., 2013). U-Pb uraninite age data presented earlier on uraninite samples from Tatie indicates an age much younger than the proposed age of magmatic U mineralization at 1870 Ma and IOCG mineralization linked to this extensive magmatic activity (e.g., Ootes et al., 2010a). The geology preserved at Beaverlodge Lake as well as previous work by Miller (1982) suggest that mineralization at Tatie is related to development of the unconformity ca. 1.9 Ga. However, the results of this study do not support this. Further work is needed to determine the primary mineralization age at Tatie. The absence of any Bi-bearing minerals and native Ag in all samples from Tatie and Bee rules out the likelihood of five-element type vein mineralization (Kissin, 1992). Finally, the presence of high-grade lenses containing upwards of 50 wt.% U_3O_8 at or near an unconformity between basement granite/porphyry and quartz arenite is not indicative of polymetallic IOCG ± U deposits. No comparable dataset (i.e. SIMS and LA-ICP-MS data on uraninite) exists for certain deposits, such as Port Radium and Rayrock.

Source of the Uranium

Uranium in the host rocks resides in minerals such as zircon and monazite. Electron microprobe observations of altered porphyry samples in chapter 3 reveal that zircon grains are sub- to euhedral and well-preserved in the regolith (Figure 3.4) and thus unlikely contributed significantly to the formation of the Tatie deposit. Monazite grains are common in the regolith and typically anhedral to subhedral and mostly fine-grained. Secondary monazite grains are common in the regolith (Figure 3.14) suggesting possible hydrothermal alteration and remobilization of U, LREE, and P. Further work is needed to determine the U concentrations of these monazites and determine their role, if any, in the formation of the Tatie deposit.

As previously discussed, the ca. 1370 Ma age at Tatie is interpreted to be a reset age on older material therefore mineralization at Tatie could be related to the formation of the unconformity ca. 1.9 Ga. But as previously demonstrated in chapter 3, a constant Th/U ratio in the Beaverlodge Lake regolith suggests that U at Tatie was not derived from the weathering profile. The age data presented in this chapter suggest that strata correlative to the Athabasca and Dismal Lake Groups may have covered the Beaverlodge Lake area. Mineralization could be related to a younger unconformity (now eroded) above the preserved older unconformity (Figure 4.11). Although hosted in an unconformity, the older unconformity was in the "basement" and therefore served a structural/chemical trap during a much younger mineralizing event. The results of this study suggest a large Mesoproterozoic sedimentary basin existed across the Western Canadian Shield and that the GBmz should be considered prospective for basement-hosted unconformity-type U mineralization.
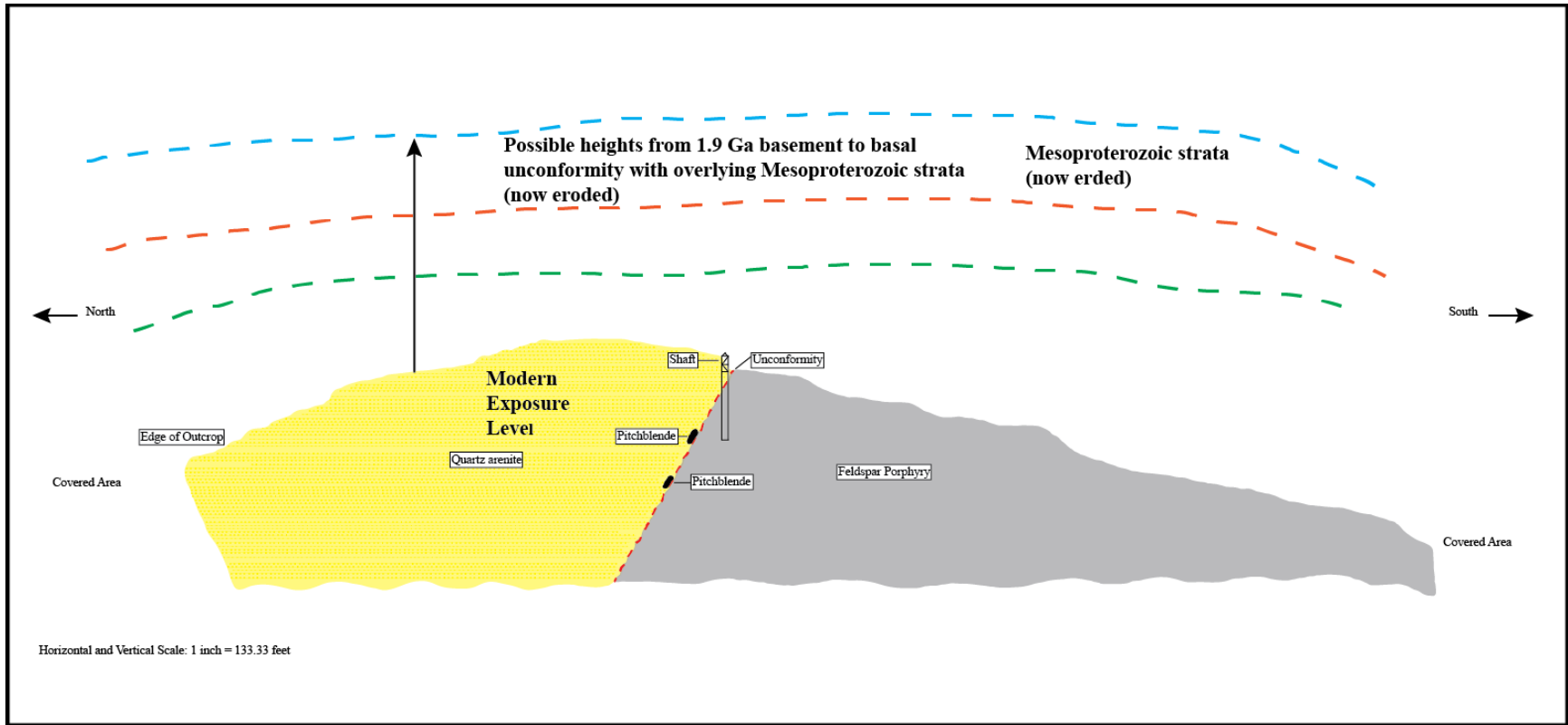
Figure 4.11 Vertical cross-section depicting the location of the Tatie deposit and the now eroded Mesoproterozoic strata. View is looking east and scale is 1 inch = 133.33 feet. North and south arrows are shown (Modified from Baykal, 1967)

Conclusions

The results obtained in this study lead to the following conclusions:

(1)   U-Pb uraninite age data from Bee (A1090) and Tatie (A1709) at Beaverlodge Lake, NT show moderate to highly discordant results, but with upper intercept ages of 1370.2 ± 79 Ma and 407 ± 21 Ma, respectively.

(2)   LA-ICP-MS analyses show that uraninite from Bee is characterized by low La concentrations and a flat to negative sloped chondrite-normalized REE pattern, similar to those of synmetamorphic uraninite found at Mistamisk and Kawanga. Rare earth element data from uraninite from Tatie displays an asymmetric bell-shaped pattern centered on Tb to Er, similar to basement-hosted unconformity-type found in the Athabasca Basin.

(3)   The processes that formed the Tatie deposit were probably similar to those in the Athabasca Basin. The age of ca. 1370 Ma is interpreted as a reset age and suggests that whatever process reset the uraninite is also recorded in the Athabasca Basin.

(4)   The ca. 407 Ma age from uraninite at Bee corresponds to late remobilization of U, probably related to groundwater flow along the Phanerozoic-Precambrian unconformity.

(5)   A large Mesoproterozoic sedimentary basin extended across the western Canadian Shield.

(6)   The Great Bear magmatic zone should be considered prospective for basement-hosted unconformity-type U mineralization.

CHAPTER 5
CONCLUSIONS

Chapter 5 provides a short summary of Chapters 3 and 4 and conclusions of this thesis. Chapter 5 contains the reference list relevant to Chapters 3 and 4. Analytical appendices follow Chapter 5 and include supporting whole-rock geochemistry, and EMPA data.

The paleoregolith and U showings at Beaverlodge Lake, NT were examined in this thesis. The paleoregolith was studied in order to shed light on Precambrian weathering conditions, to compare the weathering profile to other known counterparts, and to decipher ancient atmospheric oxygen levels. The U showings (Tatie and Bee) were studied in order to compare Tatie and Bee to other occurrences in the GBmz and world-class U deposits in the Athabasca basin and elsewhere. In order to accomplish these goals, a variety of methods were used including: fieldwork in 2011 and 2012, petrography, whole-rock geochemical analyses, mass balance calculations, electron microprobe analyses, SIMS, and LA-ICP-MS.

Conclusions in Chapter 3

- A Paleoproterozoic weathering profile developed on ca. 1930 Ma rhyodacite porphyry of the Hottah Plutonic Complex is unconformably overlain by ca. 1900 Ma quartz arenite of the Conjuror Bay Formation.

- Mass balance of major and trace elements reveal a gain in Al_2O_3, $Fe_2O_3^T$, K_2O, P_2O_5, Ba, and Rb; loss in SiO_2, MgO, Na_2O, and Sr; constant and low abundance of CaO. Titanium remains constant in the weathering profile.

- The loss of MgO could be due to the breakdown of ferromagnesian minerals. The loss of SiO_2 and Na_2O could be due to the breakdown of plagioclase feldspar. Low concentrations of CaO are due to the fact that CaO resides primarily in low Ca plagioclase and accessory fluorapatite.

- Minor remobilization of LREE is apparent on a micrometer scale, as secondary monazite grains are common in and around fluorapatite.

- The Beaverlodge paleoregolith is similar to other Precambrian examples in that there is evidence of late K-metasomatism, but it differs from post-GOE examples in the absence of a Ce-anomaly. Since Ce anomalies tend to occur in the upper oxidized soil zones, the lack of a

Ce-anomaly at Beaverlodge suggests removal of the upper oxidized soil zone by erosion. The absence of a Ce-anomaly does not suggest that the weathering profile formed under anoxic conditions as other weathering profiles that formed roughly at the same time as Beaverlodge show pronounced anomalies.

- Uranium, Th, and Th/U also remain constant throughout the profile, suggesting that the U in the U mineralization at Beaverlodge did not come from the weathering profile

Conclusions in Chapter 4

- A large number of U occurrences are present in the GBmz.
- Two distinctive styles of uraninite mineralization at Beaverlodge Lake consist of basement-hosted unconformity type and synmetamorphic-type. U-Pb dating of uraninite samples from Bee and Tatie yielded an upper intercept of 407 ± 21 Ma and 1370.2 ± 7.9 Ma, respectively.
- The ca. 407 Ma uraninite is characterized by low La concentrations then a flat to slightly negative REE pattern. REE abundances in uraninite determined by LA-ICP-MS suggest that the ca. 1370 Ma uraninite is LREE depleted relative to HREE and has an overall asymmetric bell-shaped, chondrite normalized REE pattern centered on Tb to Er.
- The ca. 407 Ma age probably corresponds to meteoric fluids cycling through the Precambrian – Phanerozoic unconformity and remobilization of U. The ca. 1370 Ma age is interpreted to be a reset age on older material and is similar to a ca. 1400 Ma Pb loss age found in the Athabasca Basin

Recommendations for Future work

This thesis has offers many opportunities for future projects, such as

- Comparing the U showing at Beaverlodge Lake, NT to fracture-hosted U deposits in the GBmz such as at Port Radium and Rayrock (using *in-situ* U-Pb dating of uraninite by SIMS and REE determination of uraninite by LA-ICP-MS).
- Finding other U showings in the northwestern Canadian Shield associated with Paleoproterozoic unconformities that can be correlated to the Athabasca and Thelon Basins.

LIST OF REFERENCES

Alexandre, P. and Kyser, T.K., 2005. Effects of cationic substitutions and alteration of uraninite, and implications for the dating of uranium deposits: The Canadian Mineralogist, v. 43, p. 1005 – 1017.

Alexandre, P., Kyser, T.K., Polito, P. and Thomas, D., 2005. Alteration Mineralogy and Stable Isotope Geochemistry of Paleoproterozoic Basement-Hosted Unconformity-Type Uranium Deposits in the Athabasca Basin, Canada: Economic Geology, v. 100, p. 1547 – 1563.

Alexandre, P., Kyser, K., Thomas, D., Polito, P., and Marlat, J., 2009. Geochronology of unconformity-related uranium deposits in the Athabasca Basin, Saskatchewan, Canada and their integration in the evolution of the basin: Mineralium Deposita, v. 44, p. 41 – 59.

Annesley, I.R., Madore, C., and Portella, P., 2005. Geology and thermotectonic evolution of the western margin of the Trans-Hudson Orogen: evidence from the eastern sub-Athabasca basement: Canadian Journal of Earth Sciences, v. 42, p. 573 – 597.

Armstrong, R.L. and Ramaekers, P., 1985. Sr isotopic study of Helikian sediment and diabase dikes in the Athabasca Basin, northern Saskatchewan: Canadian Journal of Earth Sciences, v. 22, p. 399 – 407.

Badham, J.P.N., 1975. Mineralogy, Paragenesis and Origin of the Ag—Ni, Co Arsenide Mineralisation, Camsell River, N. W. T. Canada: Mineralium Deposita, v. 1, p. 153 – 175.

Baragar, W.R.A and Donaldson, J.A., 1973. Coppermine and Dismal Lakes map areas, Geological Survey of Canada, Paper 71-39.

Baykal, O., 1967. Geological Report on Beaverlodge – Hottah Lake Prospect Atom and Tin Claims N.W.T.; Document Number 017728; Syracuse Oil Ltd. and Index Construction Company Limited, p. 1 – 45.

Bell, R.T, 1996. Sandstone uranium, *in* Geology of Canadian Mineral Deposit Types, ed. O.R. Eckstrand, W.D. Sinclair, and R.I. Thorpe; Geological Survey of Canada, Geology of Canada, no. 8, p. 212 – 219 (*also* Geological Society of America, The Geology of North America, v. P-1).

Beyer, S.R., Kyser, K., Hiatt, E.E., Polito, P.A., Alexandre, P. and Hoksbergen, K., 2012. Basin evolution and Unconformity-Related Uranium Mineralization: The Camie U Prospect, Paleoproterozoic Otish Basin, Quebec: Economic Geology, v. 107, p. 401 – 425.

Bekker, A., Holland, H.D., Wang, P.-L., Rumble Ill, D., Stein, H.J., Hannah, J.L., Coetzee, L.L., Beukes, N.J., 2004. Dating the rise of atmospheric oxygen: Nature, v. 427, p. 117 – 120.

Bennett, V. and Rivers, T., 2006. U-Pb ages of zircon primary crystallization and inheritance for magmatic rocks of the southern Wopmay orogeny, Northwest Territories: Northwest Territories Geoscience Office, NWT Open Report 2006-006, 65 p.

Bouseily, A.M. and Sokkary, A.A., 1975. The Relation between Rb, Ba and Sr in Granitic Rocks: Chemical Geology, v. 16, p. 207 – 219.

Bowles, J.F.W., 1990. Age dating of individual grains of uraninite in rocks from electron microprobe analyses: Chemical Geology, v. 83, p. 47 – 53.

Bowring, S.A., 1984. Uranium-lead zircon geochronology of Early Proterozoic Wopmay Orogen, Northwest Territories, Canada: An example of rapid crustal evolution; Unpublished Ph.D. thesis, University of Kansas, Lawrence, Kansas, 148 p.

Bowring, S.A. and Grotzinger, J.P., 1992, Implications of new chronostratigraphy for tectonic evolution of Wopmay orogen, northwest Canadian Shield: American Journal of Science, v. 292, p. 1 – 20.

Brantley, S.L. and Lebedeva, M., 2011. Learning to Read the Chemistry of Regolith to Understand the Critical Zone: Annual Review of Earth and Planetary Sciences, v. 39, p. 387 – 416.

Brantley, S.L. and White, A.F., 2009. Approaches to Modeling Weathered Regolith, In: Reviews in Mineralogy & Geochemistry, v. 70, p. 435 – 484.

Braun, JJ., Pagel, M., Muller, JP., Bilong, P., Michard, A. and Guillet, B., 1990. Cerium anomalies in Lateritic profiles: Geochimica et Cosmochimica Acta, v. 54, p. 781 – 795.

Braun, JJ., Viers, J., Dupré, B., Polve, M., Ndam, J. and Muller, JP., 1998. Solid/liquid REE fractionation in the Lateritic system of Goyoum, East Cameroon: The implication for the present dynamics of the soil covers of the humid tropical regions: Geochimica et Cosmochimica Acta, v. 62, p. 273 – 299.

Brimhall, G.H., Chadwick, O.A., Lewis, C.J., Compston, W., Williams, I.S., Danti, K.J., Dietrich, W.E., Power, M.E., Hendricks, D. and Bratt, J., 1992. Deformation Mass Transport and Invasive Processes in Soil Evolution: Science, v. 255, p. 695 – 702.

Buss, H.L., Sak, P.B., Webb, S.M. and Brantley, S.L., 2008. Weathering of the Rio Blanco quartz diorite, Luquillo Mountains, Puerto Rico: Coupling oxidation, dissolution, and fracturing: Geochimica et Cosmochimica Acta, v. 72, p. 4488 – 4507.

Byron, S. J., 2010. Giant Quartz Veins of the Great Bear Magmatic Zone, Northwest Territories, Canada: M.S.c thesis, University of Alberta, 146 p.

Byrne, N.W. and Smith, F.G., 1955. Geological Report Pitch-Ind Group, Beaverlodge Lake, N.W.T; Document Number 017384; United Uranium Corporation Limited, p. 1 – 4.

Changkakoti, A., Ghosh, D.K., Krstic, D., Gray, J. and Morton, R.D., 1986. Pb and Sr Isotope Compositions of Hydrothermal Minerals from the Great Bear Lake Silver Deposits, N.W.T., Canada: Economic Geology, v. 81, p. 739 – 743.

Cloutier, J., Kyser, K., Olivo, G.R., Alexandre, P. and Halaburda, J., 2009. The Millennium Uranium Deposit, Athabasca basin, Saskatchewan, Canada: An Atypical Basement-Hosted Unconformity-Related Uranium Deposit: Economic Geology, v. 104, p. 815 – 840.

Cook, F.A., 2011. Multiple Arc Developments in the Paleoproterozic Wopmay Orogen, Northwest Canada, In: Arc-Continent Collisions, Frontiers in Earth Science edited by D. Brown and P.D. Ryans, Chapter 14, p. 403 – 427.

Corriveau, L., Ootes, L., Mumin, H., Jackson, V., Bennett, V., Cremer, J. F., Rivard, B., McMartin, I., and Geaudoin, G., 2007. Alteration vectoring to IOCG(U) deposits in frontier volcano-plutonic terrains, Canada. In "Proceedings of Exploration 07: Fifth Decennial International Conference on Mineral Exploration" edited by B. Millkereit, 2007, p. 1171-1177.

Davis, W.J., Rainbird, R.R., Gall, Q., and Jefferson, C.J., 2008. *In situ* U-Pb dating of diagenetic apatite and xenotime: Paleofluid flow history within the Thelon, Athabasca and Hornby Bay basins: Geochimica et Cosmochimica Acta, v. 72, no. 12S, p. A203.

Deer, W.A., Howie, R.A., and Zussman, J., 1992. An introduction to the rock-forming minerals: London, Longman, 696 p.

Driese S.G., Jirsa, M.A., Ren, M., Bratnely, S.L., Sheldon, N.D., Parker, D. and Schmitz, M., 2011. Neoarchaen paleoweathering of tonalite and metabasalt: Implications for reconstructions of 2.69 Ga early terrestrial ecosystems and paleoatmospheric chemistry: Precambrian Research, v. 189, p. 1 – 17.

Du, X., Rate, A.W. and Gee, M.A. Mary., 2012. Redistribution and mobilization of titanium, zirconium, and thorium in an intensely weathered Lateritic profile in Western Australia: Chemical Geology, v. 330-331, p. 101 – 115.

Duddy, I.R., 1980. Redistribution and fractionation of rare-earth and other elements in a weathering profile: Chemical Geology, v. 30, p. 363 – 381.

Evans, D.A.D. and Mitchell, R.N., 2011. Assembly and breakup of the core of Paleoproterozoic – Mesoproterozoic supercontinent Nuna: Geology, v. 39, p. 443 – 446.

Fayek, M. and Kyser, T.K., 1997. Characterization of Multiple Fluid-Flow Events and Rare-Earth-Element Mobility Associated with Formation of Unconformity-Type Uranium Deposits in the Athabasca Basin, Saskatchewan: The Canadian Mineralogist, v. 35, p. 627 – 658.

Fayek, M. and Kyser, T.K., 2000. Low temperature oxygen isotopic fractionation in the uraninite-UO_3-CO_2-H_2O system: Geochimica et Cosmochimica, v. 64, p. 2185 – 2197.

Fayek, M., Harrison, T.M., Grove, M., and Coath, C.D., 2000. A Rapid In Situ Method for Determining the Ages of Uranium Oxide Minerals: Evolution of the Cigar Lake Deposit, Athabasca Basin: International Geology Review, v. 42, p. 163 – 171.

Fayek M., Kyser, T.K., and Riciputi, L.R., 2002. U and Pb Isotope Analysis of Uranium Minerals by Ion Microprobe and the Geochronology of the McArthur River and Sue Zone Uranium Deposits, Saskatchewan, Canada: The Canadian Mineralogist, v. 40, p. 1553 – 1569.

Fedo, C.M., Nesbitt, H.W., and Young, G.M., 1995. Unraveling the effects of potassium metasomatism in sedimentary rocks and paleosols, with implications for paleoweathering conditions and provenance: Geology, v. 23, p. 921 – 924.

Frei, R. and Polat, A., 2013. Chromium isotope fractionation during oxidative weathering— Implications from the study of a Paleoproterozoic (ca. 1.9 Ga) paleosol, Schreiber Beach, Ontario, Canada: Precambrian Research, v. 224, p. 434 – 453.

Gall, Q., 1994. The Proteroizoic Thelon paleosol, Northwest Territories, Canada: Precambrian Research, v. 68, p. 115-137.

Gandhi, S.S., 1994. Geological setting and genetic aspects of mineral occurrences in the southern Great Bear magmatic zone, Northwest Territories; in W.D. Sinclair and D.G. Richardson, eds., Studies of Rare-Metal Deposits in the Northwest Territories: Geological Survey of Canada, Bulletin 475, p. 63-96.

Gandhi, S.S., Carriere, J.J., and Prasad, N., 2000. Implications of a preliminary fluid inclusion study of giant quartz veins of the southern Great Bear magmatic zone, Northwest Territories; Geological Survey of Canada: Current Research, no. 2000-C1.

Gandhi, S.S., Mortensen, J.K., Prasad, N., and van Breemen, O., 2001. Magmatic evolution of the southern Great Bear continental arc, northwestern Canadian Shield: geochronological constraints: Canadian Journal of Earth Science, v. 38, p. 767 – 785.

Gandhi, S.S. and van Breemen, O., 2005. SHRIMP U-Pb geochronology of detrital zircons from the Treasure Lake Group – new evidence for Paleoproterozoic collisional tectonics in the southern Hottah terrane, northwestern Canadian Shield: Canadian Journal of Earth Science, v. 42, p. 833 – 845.

Goad, R.E., Mumin, A.H., Duke, N.A., Neale, K.L., Mulligan, D.L. and Camier, W.J., 2000. The NICO and Sue-Dianne Proterozoic, Iron Oxide-hosted Polymetallic Deposits, Northwest Territories: Application of the Olympic Dam Model in Exploration: Exploration and Mining Geology, v. 9, no. 2, p. 123 – 140.

Grady, J.C., 1955. Cormac Group; Document Number 080798; Traverse Longlac Mines Ltd; p. 1 – 11.

Grant, J.A., 1986. The isocon diagram—a simple solution to Gresens' equation for metasomatic alteration: Economic Geology, v. 81, p. 1976 – 1982.

Grant, J.A., 2005. Isocon analysis: A brief review of the method and applications: Physics and Chemistry of the Earth, v. 30, p. 997 – 1004.

Gresens, R.L., 1967. Composition-volume relationships of metasomatism: Chemical Geology, v. 2, p. 47 – 55.

Hargreaves, E.H., 1935. Shaft and Trench work on Tatie claims; Document Number 015222; Great Bear Development Co; p. 1 – 7.

Harlan, S.S., Heaman, L., LeCheminant, A.N. and Premo, W.R., 2003. Gunbarrel mafic magmatic event: A key 780 Ma time marker for Rodinia plate reconstructions: Geology, v. 31, p. 1053 – 1056.

Hazen, R.M., Ewing, R.C. and Sverjensky, D.A., 2009. Evolution of uranium and thorium minerals: American Mineralogist, v. 94, p. 1293 – 1311.

Henderson, J.F., 1949. Pitchblende occurrences between Beaverlodge and Hottah lakes, Northwest Territories: Geological Survey of Canada, Paper 49-16.

Hiatt, E.E., Palmer, S.E., Kyser, T.K. and O'Connor, T.K., 2010. Basin evolution, diagenesis and uranium mineralization in the Paleoproterozoic Thelon Basin, Nunavut, Canada: Basin Research, v. 22, pp. 302-323.

Hildebrand, R.S., Bowring, S.A., Steer, M.E., and Van Schmus, W.R., 1983. Geology and U-Pb geochronology of parts of the Leith Peninsula and Rivère Grandin map areas, District of Mackenzie, *in* Current Research, Part A: Geological Society of Canada Paper 83-1A, p. 329 – 342.

Hildebrand, R.S. and Roots, C.F., 1985. Geology of the Rivère Grandin map area Hottah Terrane and western Great Bear magmatic zone, District of Mackenzie: Geological Survey of Canada, Paper 85-01A, p. 373 – 383.

Hildebrand, R.S., 1986. Kiruna-type deposits; their origin and relationship to intermediate subvolcanic plutons in the Great Bear magmatic zone, Northwest Canada: Economic Geology, v. 81, p. 640 – 659.

Hildebrand, R.S., Hoffman, P.F. and Bowring, S.A., 1987. Tectono-Magmatic Evolution of the 1.9-Ga Great Bear Magmatic Zone, Wopmay Orogen, Northwestern Canada: Journal of Volcanology and Geothermal Research, v. 32, p. 99 – 118.

Hildebrand, R.S., Hoffman, P.F., and Bowring, S.A., 2010a. The Calderian orogen in Wopmay orogen (1.9 Ga), northwestern Canadian Shield: GSA Bulletin, v. 122, p. 794 – 814.

Hildebrand, R.S., Hoffman, P.F., Housh, T. and Bowring, S.A., 2010b. The nature of volcano-plutonic relations and the shapes of epizonal plutons of continental arcs as revealed in the Great Bear magmatic zone, northwestern Canada: Geosphere, v. 6, p. 812 – 839.

Hoeve, J., and Sibbald, T.I.I., 1978. On the genesis of Rabbit Lake and other unconformity-type uranium deposits in northern Saskatchewan, Canada: Economic Geology, v. 73, p. 1450 – 1473.

Hoeve, J., and Quirt, D., 1984. Mineralization and host rock alteration in relation to clay mineral diagenesis and evolution of the Middle-Proterozoic, Athabasca Basin, northern Saskatchewan, Canada. Saskatchewan Research Council, Technical Report No. 187, 187pp.

Hoffman, P.F., Bowring, S.A., Buchwaldt, R. and Hildebrand, R.S., 2011. Birthdate for the Coronation margin paleocean: age of initial rifting in Wopmay orogen, Canada: Canadian Journal of Earth Sciences, v. 48, p 281 – 293.

Holland, H.D., Feakes, C.R., Zbinden, E.A., 1989. The Flin Flon Paleosol and the Composition of the atmosphere 1.8 Bybp: American Journal of Science, v. 289, p. 362 – 389.

Holland, H.D., 2002. Volcanic gases, black smokers, and the Great Oxidation Event: Geochimica et Cosmochimica Acta, v. 66, p. 3811 – 3826.

Holland, H.D., 2006. The oxygenation of the atmosphere and oceans: Philosophical Transactions of the Royal Society B, v. 361, p. 903 – 915.

Holland, H.D., 2009. Why the atmosphere become oxygenated: Geochimica et Cosmochimica Acta, v. 73, p. 5241 – 5255.

Humphris, S.E., Chapter 9: The Mobility of Rare Earth Elements in the Crust. In: Rare Earth Element Geochemistry. Ed. P. Henderson. Netherlands: Elsevier Science Publishers, 1984. p. 317 – 340. Print.

Irving, E., Baker, J., Hamilton, M. and Wynne, P.J., 2004. Early Proterozoic geomagnetic field in western Laurentia: implications for paleolatitudes, local rotation and stratigraphy: Precambrian Research, v. 129, p. 251 – 270.

Jackson, V.A. and Ootes L., 2012. Preliminary Geologic Map of the South-Central Wopmay Orogen (parts of NTS 86B, 86C, and 86D); results from 2009 to 2011; Northwest Territories Geoscience Office, NWT Open Report 2012-004. 1 map, scale 1:100 000.

Janeczek, J. and Ewing, R.C., 1995. Mechanisms of Lead Release from Uraninite in Natural Fission Reactors in Gabon: Geochimica et Cosmochimica Acta, v. 59, p. 1917 – 1931.

Jefferson, C.W., Thomas, D.J., Gandhi, S.S., Ramaekers, P., Delaney, G., Brisbin, D., Cutts, C., Quirt, D., Portella, P., and Olson, R.A., 2007. Unconformity-associated uranium deposits of the Athabasca Basin, Saskatchewan and Alberta, *in* EXTECH IV: Geology and Uranium Exploration TECHnology of the Proterozoic Athabasca Basins, Saskatchewan and Alberta, ed. C.W. Jefferson and G. Delaney; Geological Association of Canada, Bulletin 588, p. 23 – 67 (also *Sasaktchewan Geological Society, Special Publications 18; Geological Association of Canada, Mineral Deposits Division, Special Publications 4*).

Jefferson, C.W., Peterson, T., Tschirhart, V., Davis, W., Scott, J.M.J., Reid, K., Ramaekers, P., Gandhi, S.S., Bleeker, W., Pehrsson, S., Morris, W.A., Fayek, M., Potter, E., Bridge, N., Grunsky, E., Keating, P., Ansdell, K., and Banerjee, N., 2013a. LIPs and Proterozoic uranium (U) deposits of the Canadian Shield; Geological Survey of Canada, Open File 7352, 56 pages + spread sheet, doi:10.4095/292377

Kerans, C., Ross, G.M., Donaldson, J.A., and Geldsetzer, H.J., 1981. Tectonism and depositional history of the Helikian Hornby Bay and Dismal Lakes Groups, District of Mackenzie, *in* Proterozoic Basins of Canada, ed. F.H.A. Campbell, Geological Survey of Canada, Paper 81-10, p. 157 – 182.

Kidd, D.F., 1936. Rae to Great Bear Lake, Mackenzie District, Northwest Territories: Geological Survey of Canada, Memoir 187, p. 44.

Kish, L. and Cuney, M., 1981. Uraninite-albite veins from Mistamisk Valley of the Labrador Trough, Quebec: Mineralogical Magazine, v. 44, p. 471 – 483.

Kissin, S.A., 1992. Five-element (Ni-Co-As-Ag-Bi) Veins: Geoscience Canada, v. 19, n. 3, p. 113 – 124.

Konhauser, K.O., Pecoits, E., Lalonde, S.V., Papineau, D., Nisbet, E.G., Barley, M.E., Arndt, N.T., Zahnle, K., and Kamber, B.S., 2009. Oceanic nickel depletion and a methanogen famine before the Great Oxidation Event: Nature, v. 458, p. 750 – 754.

Kranidiotis, P. and MacLean, W.H., 1987. Systematrics of Chlorite Alteration at the Phelps Dodge Massive Sulfide Deposit, Matagami, Quebec: Economic Geology, v. 82, p. 1898 – 1911.

Kotzer, T.G. and Kyser, T.K., 1993. O, U, and Pb isotopic and chemical variations in uraninite: Implications for determining the temporal and fluid history of ancient terrains: American Mineralogist, v. 78, p. 1262 – 1274.

Kotzer, T.G., and Kyser, T.K., 1995. Petrogenesis of the Proterzoic Athabasca Basin, northern Saskatchewan, Canada, and its relation to diagenesis, hydrothermal uranium mineralization and paleohydrogeology: Chemical Geology, v. 120, p. 45 – 89.

Kyser, K. and Cuney, M., 2009. Unconformity-related uranium deposits, *in* Recent and not-so-recent developments in uranium deposits and implications for exploration, ed. M. Cuney and K. Kyser, Mineralogical Association of Canada, Short Course v. 39, p. 161 – 220.

Lahtinen, R. and Nironen, M., 2010. Paleoproterozoic Lateritic paleosol-ultra-mature/mature quartzite-meta-arkose successions in southern Fennoscandia-intra-orogenic during the Svecofennian orogeny: Precambrian Research, v. 183, p. 770 – 790.

LeCheminant, A.N. and Heaman, L.M., 1989. Mackenzie igneous events, Canada; Middle Proterozoic hotspot magmatism associated with ocean opening: Earth and Planetary Science Letters, v. 96, p. 38 – 48.

Lin, C. and Bailey, S., 1985. Structural data for sudoite: Clays and Clay Minerals, v. 33, p. 410 – 414.

Ludvig, K., 1993. ISOPLOT, Excel Based Program for Plotting Radiogenic Isotopes; USGS, Open File Report, n. 91-445, p. 1 – 42.

Macdonald, C.C., 1980. Mineralogy and Geochemistry of a Precambrian Regolith in the Athabasca Basin; M.S.c Thesis University of Saskatchewan, 161 p.

Maynard, J.B., Sutton, S.J., Robb, L.J., Ferraz, M.F., Meyer, F.M., 1995. A Paleosol developed on Hydrothermally Altered Granite from the Hinterland of the Witwatersrand Basin: Characteristics of a Source of Basin Fill: The Journal of Geology, v. 103, p. 357 – 377.

McGlynn, J.C., 1979. Geology of the Precambrian rocks of the Riviere Grandin and in part of the Marian River map areas, District of Mackenzie: Geological Survey of Canada, Paper 79-01A, p. 127 – 131.

Mercadier, J., Cuney, M., Lach, P., Boiron, M-C., Bonhoure, J., Richard, A., Leisen, M. and Kister, P., 2011. Origin of uranium deposits revealed by their rare earth element signature: Terra Nova, v. 23, p. 264 – 269.

Miller, R.G., 1982. The geochronology of uranium deposits in the Great Bear batholith Northwest Territories: Canadian Journal of Earth Sciences, v. 19, p. 1428 – 1448.

Mitchell, R.L. and Sheldon, N.D., 2009. Weathering and paleosol formation in the 1.1 Ga Keweenawan Rift: Precambrian Research, v. 168, p. 271 – 283.

Morteani, G. and Preinfalk, C., 1996. REE distribution and REE carriers in laterites formed on the alkaline complexes of Araxá and Catalão (Brazil), In Rare Earth Minerals: Chemistry, Origin and Ore Deposits. Mineralogical Society Series 7, p. 227 – 255.

Mumin, A.H., Corriveau, L., Somarin, A.K. and Ootes, L., 2007. Iron Oxide Copper-Gold-type Polymetallic Mineralization in the Contact Lake Belt, Great Bear Magmatic Zone, Northwest Territories: Exploration and Mining Geology, v. 16, p. 187 – 208.

Nahon, D.B. Introduction to Petrology of Soils and Chemical Weathering. John Wiley and Sons, 1990. Print.

Nedachi, Y., Nedachi, M., Bennett, G. and Ohmoto, H., 2005. Geochemistry and mineralogy of the 2.45 Ga Pronto paleosols, Ontario, Canada: Chemical Geology, v. 214, p. 21 – 44.

Nesbitt, H.W., 1979. Mobility and fractionation of rare earth elements during weathering of a granodiorite: Nature, v. 279, p. 206 – 210.

Nesbitt, H.W. and Wilson, R.E., 1992. Recent Chemical Weathering of Basalts: American Journal of Science, v. 292, p. 740 – 777.

Ootes, L.L., Goff, S., Jackson, V.A., Gleeson, S.A., Creaser, R.A., Samson, I.M., Evensen, N., Corriveau, L. and Mumin, A.H., 2010a. Timing and thermochemical constraints on multi-element mineralisation at the Nori/RA Cu-Mo-U prospect, Great Bear magmatic zone, Northwest Territories, Canada: Mineralium Deposita, v. 45, p. 549 – 566.

Ootes, L., Jackson, V.A., Davis, W.J., Bleeker, W., Acosta-Gongora, P., Smar, L., and Newton, L., 2010b. Components of Hottah terrane vs. Great Bear magmatic zone: new chronostratigraphy and implications for mineral deposits, In: Watson, D.M. (compiler), 2010. 38th Annual Yellowknife Geoscience Forum Abstracts; Northwest Territories Geoscience Office, Yellowknife, NT. YKGSF Abstracts Volume 2010.

Ootes, L., Davis, W., Jackson, V.A., Newton, L., Acosta-Gongora, P. and Shakotko P., 2012. The Hottah – Great Bear Continuum: Implications for IOCG Mineralization and Plate Interactions in the Western Canadian Shield, In: Watson, D.M. (compiler), 2012. 40th Annual Yellowknife Geoscience Forum Abstracts; Northwest Territories Geoscience Office, Yellowknife, NT. YKGSF Abstracts Volume 2012.

Ootes, L., Harris, J., Jackson, V.A., and Azar, B. and Corriveau, L., 2013. Uranium-enriched bedrock in the central Wopmay orogen: implications for mineralization; Exploration and Mining Geology, in press.

Pan, Y. and Stauffer, M.R., 2000. Cerium anomaly and Th/U fractionation in the 1.85 Flin Flon Paleosol: Clues from REE- and U-rich accessory minerals and implications for paleoatmospheric reconstruction: American Mineralogist, v. 85, p. 898 – 911.

Panahi A., Young, G.M., and Rainbird, R.H., 2000. Behavior of major and trace elements (including REE) during Paleoproterozoic pedogenesis and diagenetic alteration of an Archaen granite near Ville Marie, Québec, Canada: Geochimica et Cosmochimica Acta, v. 64, p. 2199 – 2220.

Prothero, Donald R, and F. Schwab. Sedimentary Geology An Introduction to Sedimentary Rocks and Stratigraphy. W. H. Freeman and Company, 2004. Print.

Rainbird, R.H., Jefferson, C.W., Hildebrand, R.S., and Worth, J.K., 1994. The Shaler
    Supergroup and revision of Neoproterozoic stratigraphy in the Amundsen Basin,
    Noerthwest Territories: Geological Survey of Canada: Current Research, Paper, 94-1A,
    61-70.

Ramaekers, P., 1990. Geology of the Athabasca Group (Helikian) in northern Saskatchewan:
    Saskatchewan Geological Survey Report, no. 195, 49 p.

Ramaekers, P., Jefferson, C.W., Yeo, G.M., Collier, B., Long, D.G.F., Drever, G., McHardy, S.,
    Jiricka, D., Cutts, C., Wheatley, K., Catuneau, O., Bernier, S., Kupsch, B., and Post, R.T.,
    2007, Revised geological map and stratigraphy of the Athabasca Group, Saskatchewan
    and Alberta: in EXTECH IV: Geology and Uranium EXploration TECHnology of the
    Proterozoic Athabasca Basin, Saskatchewan and Alberta, (ed.) Jefferson, C.W., and
    Delaney, G.; Geological Survey of Canada, Bulletin 588, p. 155-191.

Rayner, N.M., Stern, R.A., and Rainbird, R.H., 2003. SHRIMP U-Pb detrital zircon
    geochronology of Athabasca group sandstones, northern Saskatchewan and Alberta;
    Geological Survey of Canada: Current Research, no. 2003-F2, 20 p.

Reardon, N.C., 1992. Magmatic – Hydrothermal Systems and Associated Magnetite-Apatite-
    Actinolite Deposits, Echo Bay, Northwest Territories, M.S.c Thesis in Geology at
    University of Ottawa.

Reichenbach, I.G., 1991, The Bell Island Bay Group, remnant of an early Proterozoic ensialic
    marginal basin in Wopmay orogeny, Distrinct Mackenzie; Geological Survey of Canada,
    Paper 88-28.

Renac, C., Kyser, T.K., Durocher, K., Dreaver, G., and O'Connor, T., 2002. Comparison of
    diagenetic fluids in the Proterozoic Thelon and Athabasca basins, Canada: implications
    for long protracted fluid histories in stable intracratonic basins: Canadian Journal of Earth
    Sciences, v. 39, p. 113 – 132.

Retallack, G.J. Soils of the Past: an Introduction to Paleopedology. Boston: Unwin Hyman,
    1990. Print.

Reyx, J. and Ruhtmann, F., 1993. Etude metallographie des differentes associates minerals et
    caracterisation chimique des mineraux uraniferes du gisement de Cigar Lake
    (Saskatchewan, Canada): Canadian Journal of Earth Sciences, v. 30, p. 705 – 719.

Robinson, B.W. and Ohmoto, H., 1973. Mineralogy, Fluid Inclusions, and Stable Isotopes of the
    Echo Bay U-Ni-Ag-Cu Deposits, Northwest Territories, Canada: Economic Geology, v.
    68, p. 635 – 656.

Ross, G.M., 1983. Geology and depositional history of the Hornby Bay Group, Proterozoic,
    Northwest Territories, Canada. Ph.D. thesis. Carleton University, Ottawa, Canada.

Rye, R. and Holland, H.D., 1998. Paleosols and the Evolution of the Atmospheric Oxygen: A Critical Review: American Journal of Science, v. 298, p. 621 – 672.

Rye, R. and Holland, H.D., 2000. Geology and Geochemistry of Paleosols Developed on the Hekpoort Basalt, Pretoria Group, South Africa: American Journal of Science, v. 300, p. 85 – 141.

Scott, K.M. and Pain, C.F. Regolith Science. New York: Springer Science + Business Media B.V., 2008. Print.

Shakotko, P., Pan, Y. and Ootes, L., 2013. A Porphyry – Weathered Porphyry – Quartz Arenite Succession at Beaverlodge Lake, Northwest Territories: Mass Balance Approach to a Precambrian regolith; Northwest Territories Open Report, in review.

Sharpe, R. and Fayek, M., 2011. The World's Oldest Observed Primary Uraninite: The Canadian Mineralogist, v. 49, p. 1199 – 1210.

Sharpe, R., 2013. The Geochemistry and Geochronology of the Bong Uranium Deposit, Thelon Basin, Nunavut, Canada. M.S.c thesis, University of Manitoba, 213 p.

Sheldon, N.D., 2006. Precambrian paleosols and atmospheric CO2 levels: Precambrian Research, v. 147, p. 148 – 155.

Sheldon, N.D. and Tabor, N.J., 2009. Quantitative paleoenvironmental and paleoclimatic reconstruction using paleosols: Earth-Science Reviews, v. 95, p. 1 – 52.

Sun, S.-s. and McDonough, W.F., 1989. Chemical and isotopic composition of oceanic basalts: implications for mantle composition and process: Geological Society, London Special Publications, v. 42, p. 313 – 345.

Taylor, G. and Eggleton, R.A., Regolith Geology and Geomorphology, John Wiley & Sons, 2001. Print.

Utsunomiya S., Murakami, T., Nakada, M. and Kasama, T., 2003. Iron oxidation state of a 2.45-Byr-old paleosol developed on mafic volcanics: Geochimica et Cosmochimica Acta, v. 67, p. 213 – 221.

Velbel, M.A., 1990. Mechanisms of saprolitization, Isovolumetric weathering and pseudomorphs replacement during rock weathering — A review: Chemical Geology, v. 84, p. 17 – 18.

Walden, K.M., 2005. Neodymium and Strontium Isotope Investigation of the Precambrian Kalkkloof Paleosol, South Africa; M.S.c Thesis University of Pittsburg, 52 p.

Wallis, R.H., Saracoglu, N., Brummer, J.J. and Golightly, J.P., 1983. Geology of the McClean uranium deposits, *in* Uranium exploration in Athabasca Basin, Saskatchewan, Canada, ed. E.M. Cameron, Geological Society of Canada, Paper 82-11, p. 71 – 110.

Wallis, R.H., Saracoglu, N., Brummer, J.J. and Golightly, J.P., 1985. Geology of the McClean uranium deposits, *in* Geology of Uranium Deposits, eds. T.I. Sibbald and W. Petruk, Canadian Insitute of Mining and Metallurgy, Special Volume 32, p. 101 – 131.

White, A.F., 1995. Chemical weathering rates of silicate minerals in soils. *In* Chemical Weathering Rates of Silicate Minerals, ed. A.F. White and S.L. Brantley, Mineral Society of America, v. 31, p. 407 – 458.

White, A.F., Bullen, T.D., Schulz, M.S., Blum, A.E., Huntington, T.G. and Peters, N.E., 2001. Differential rates of feldspar weathering in granitic regoliths: Geochimica et Cosmochimica Acta, v. 65, p. 847 – 869.

Wiggering, H. and Beukes, N.J., 1990. Petrography and Geochemistry of a 2000-2200-Ma-old Hematitic Paleo-Alteration Profile on Ongeluk Basalt of the Transvaal Supergroup, Griqualand West, South Africa: Precambrian Research, v. 46, p. 241 – 248.

Winter, J.D., An Introduction to Igneous and Metamorphic Petrology, Prentice Hall, 2001. Print.

Young, G.M. and Nesbitt, H.W., 1998. Processes controlling the distribution of Ti and Al in weathering profiles, siliclastic sediments, and sedimentary rocks: Journal of Sedimentary Research, v. 68, p. 448 – 455.

Zhao, G., Cawood, P.A., Wilde, S.A. and Sun, M., 2002. Review of global 2.1 – 1.9 Ga orogens: implications for a pre-Rodinia supercontinent: Earth-Science Reviews, v. 59, p. 125 – 162.

Zhao, G., Sun, M., Wilde, S.A. and Sanzhong, L., 2004. A Paleo-Mesoproterozoic supercontinent: assembly, growth, and breakup: Earth-Science Reviews, v. 67, p. 91 – 123.

APPENDICES

APPENDIX A

ANALYTICAL TECHNIQUES

Chapter 3

The author undertook fieldwork in the summer of 2011. In 2011, five traverses over 160 metres with an average distance 50 metres between traverses were made along the Hottah granitoids – Conjuror Bay Formation unconformity. Sixteen samples were collected and included: a least-altered porphyry that was collected at the base of the ridge and furthest from the unconformity, heavily altered porphyry, heavily altered mafic dyke, porphyry clasts with weathering rinds entrained in the quartz arenite, quartz arenite, and siltstone from the overlying Conjuror Bay Formation. Of the sixteen samples collected, twenty two samples were carefully cut, crushed, and powdered by the author at the University of Saskatchewan. Samples were sent to Activation Labs in Ancaster, ON and were analyzed using fusion the method ICP – ES for major elements and ICP – MS for trace and rare earth elements. The complete geochemical dataset is presented in Appendix B.

Petrography was conducted on a polarizing microscope with transmitted and reflected light capabilities. Electron microprobe analysis was conducted at the University of Saskatchewan using a JEOL JXA-8600 superprobe equipped with three wavelength dispersive and one-energy dispersive spectrometers. Electron microprobe analysis concentrated on imaging of accessory minerals using backscatter imaging at an accelerating voltage of 15 kV.

Chapter 4

The author undertook fieldwork in the summer of 2012. Twelve samples were collected along the Zebulon Formation – Conjuror Bay Formation unconformity. Of the fourteen samples collected in 2012, twelve samples were crushed and powdered by the author at the University of Saskatchewan in 2012. Powders from 2012 were also sent to Activation Labs and underwent the same analyses as the samples in 2011. The complete geochemical dataset is presented in Appendix I.

Two U-rich samples (12ps1 and 12ps4) containing minor amounts of uranium (scintillometer readings of ca. 480 counts per second) were collected from Beaverlodge Lake in 2012. One U sample (12ps1) came from a waste rock pile outside the main Tatie shaft along the Hottah granitoids – Conjuror Bay Formation quartz arenite unconformity. The second sample (12ps4) came from an exploration trench in a giant quartz vein 2 km NE of the main shaft at Tatie. Six U ore samples were received on loan from the Spence Collection of the Earth Materials collection of Natural Resources Canada. According to information provided by Natural Resources Canada, sample A1090 came from the Bee 3 claim and samples A1709, A1092, A1094, and A1901 came from the Tatie 3 claim. From these samples in addition to the samples collected in 2012, polished thin sections (~ 30 μm and 100 μm) were made for petrographic observations, electron microprobe analysis (EMPA), secondary ion mass spectrometric (SIMS) analysis, and laser ablation inductively coupled plasma mass spectrometry (LA-ICP-MS).

Optical Microscope and Electron Microprobe Analysis (EMPA)

Petrography was conducted on a binocular polarizing microscope with transmitted and reflected light capabilities. Electron microprobe analysis (EMPA) was conducted at the University of Saskatchewan using a JEOL JXA-8600 Superprobe equipped with three wavelength dispersive and one energy dispersive spectrometers. Electron microprobe analysis concentrated on imaging of uraninite and secondary minerals using backscatter imaging. Additional quantitative electron microprobe analysis was undertaken for the purpose of determining the chemical composition of uraninite, coffinite, and carbonates.

The following operating conditions were used in the analysis of uraninite: accelerator voltage of 15 kV, beam current of 50 nA, beam diameter of 3 to 10 μm, count times of 30 s for major elements plus U and 60 s for Th, Pb, and Y. Standards used include quartz (Si), magnetite (Fe), crocoite (Pb), diopside (Mg), Y-Al garnet (Y and Al), apatite (P), diopside (Ca), and metals (U and Th). Appendix C summarizes the chemical composition of uraninite. Quantitative analyses of uraninite allowed for the determination of chemical U-Th-Pb ages following the procedure by Bowles (1990) (Appendix C).

The following operating conditions were used in the analysis of coffinite: accelerator voltage of 15 kV, beam current of 50 nA, beam diameter of 3 to 10 μm, count times of 30 s for major elements plus U and 60 s for Th, Pb, and Y. Standards used included quartz (Si), magnetite (Fe), crocoite (Pb), diopside (Ca and Mg), Y-Al garnet (Y and Al), rutile (Ti), jadeite (Na), sanidine (K) and metals (U and Th). Appendix D summarizes the chemical composition of coffinite.

The following operating conditions were used in the analysis of carbonates: accelerator voltage of 15 kV, beam current of 50 nA, beam diameter of 10 μm, count times of 40 s for major and trace elements. Standards included magnetite (Fe), diopside (Ca and Mg), bustamite (Mn), celestine (Sr), and dolomite (C). Appendix E summarizes the chemical composition of carbonates phases.

Secondary Ion Mass Spectrometry (SIMS)

Secondary ion mass spectrometry (SIMS) analysis was undertaken in the Department of Geological Sciences at the University of Manitoba under supervision of Dr. Mostafa Fayek and Ryan Sharpe. The objective was to determine U and Pb isotopic values and possibly the timing of U mineralization. A detailed description of the analytical techniques is provided and can also be found in Sharpe and Fayek (2011).

Samples A1090 and A1709 (from Bee and Tatie showings, respectively) were chosen for SIMS analysis because these samples have abundant, large (> 5 μm in diameter) and relatively unaltered uraninite grains. Each sample was cleaned and immersed in deionized water in an ultrasonic bath. After the ultrasonic bath, the samples were further cleaned twice, first with deionized water and second with ethanol. After cleaning, a thin layer of gold was coated to the surface of the sample. Secondary Ion Mass Spectrometry analysis was undertaken using a CAMECA 7f and the following isotopes were detected: ^{204}Pb, ^{206}Pb, ^{207}Pb, ^{208}Pb, ^{230}Th, ^{234}U, ^{235}U, and ^{238}U. Typical analyses consisted of 30 cycles lasting ~10 minutes.

The measurement process introduced a mass-dependent bias (instrumental mass fractionation; Sharpe and Fayek, 2011). To correct for this, a standard was used for calibration

(PC-O6 and TKK). Accurate values of $^{206}Pb/^{204}Pb$, $^{207}Pb/^{204}Pb$, $^{207}Pb/^{206}Pb$, $^{235}U/^{238}U$, $^{206}Pb/^{238}U$, and $^{207}Pb/^{235}U$ from the standards were obtained using a Thermal Ionization Mass Spectrometer (TIMS) to correct for instrument mass fractionation (Sharpe and Fayek, 2011). The standards and unknown samples were analyzed during the same analytical session. TIMS values of U and Pb from the standard were used to correct for IMF using Equation A.1:

$$\alpha_{SIMS} = \frac{R_{SIMS}}{R_{TIMS}} \qquad \text{(Equation A.1)}$$

where $R = {}^{207}Pb/^{206}Pb$, $^{206}Pb/^{238}U$, and $^{207}Pb/^{235}U$

This coefficient (α) is applied to the measured U and Pb values to obtain "true" isotopic ratios (Equation A.2; Sharpe and Fayek, 2011):

$$R_{True} = \alpha \times R_{SIMS} \qquad \text{(Equation A.2)}$$

where $R = {}^{207}Pb/^{206}Pb$, $^{206}Pb/^{238}U$, and $^{207}Pb/^{235}U$

After the ratios were corrected for mass bias, results were plotted using the ISOPLOT v. 3.7 program (Ludvig, 1993). Locations chosen for U and lead isotopic analysis represent surfaces where the uraninite grains are least-altered and least-fractured. In some instances, if the uraninite grain was large enough, transects across the grain were made. Concordia plots were generated using $^{206}Pb/^{238}U$ and $^{207}Pb/^{235}U$ values. Appendix G summarizes the U and Pb isotopic values from uraninites from the Tatie and Bee.

Laser Ablation Inductively Coupled Plasma Mass Spectrometry (LA-ICP-MS)

Laser ablation inductively coupled plasma mass spectrometry (LA-ICP-MS) analysis was carried out on uraninite grains in samples A1090 and A1709 (Bee and Tatie showings, respectively) at the Geological Society of Canada, Ottawa, by Dr. Eric Potter. The purpose of this was to determine REE concentrations in uraninite and to compare values with uraninite from other U deposits (e.g. Mercadier et al., 2011). Uraninite grains in samples A1090 and A1709 were ablated adjacent to those that were analyzed via SIMS. Uraninite grains were ablated using a 193 nm Photon-Machines Analyte with Helex ablation cell. Ablated particulate material was analyzed by an Agilent 7700x quadrupole ICP-MS. Ablation was achieved by focusing the beam at the sample surface with a constant energy at 40% of 4 mJ/cm^2 and a constant repetition rate at

10 Hz. The diameter of the ablation depended on the sample: 52 μm spot sized used on all standards whereas a 25 μm spot size was used for the samples. Appendix H summarizes the REE contents from uraninites from Tatie and Bee.

Unused Microprobe Data

Quantitative electron microprobe analysis was undertaken on the minerals: chlorite, fluorapatite, Fe oxide, Ti oxide, and Fe-Ti oxide. The results of these analyses are presented in Appendices J to L. Relevant operating conditions are presented below followed by a brief summary of the key results.

Chlorite

Electron microprobe analysis concentrated on imaging of chlorite from altered porphyry samples collected in 2011. Additional quantitative electron microprobe analysis was undertaken for the purpose of determining the chemical composition of chlorite. The following operating conditions were used in the analysis of chlorites: accelerator voltage of 15 kV, beam current of 50 nA, beam diameter of 10 μm, and count times of 30 s for major elements. Standards included pyrope (Si), rutile (Ti), almandine (Al), chromite (Cr), almandine (Fe), diopside (Mg), bustamite (Mn), diopside (Ca), jadeite (Na), phlogopite (K), and tugtapite (Cl). Appendix J summarizes the chemical composition of chlorite.

Chlorites in the Athabasca Basin have been identified in the pre- and post- ore alteration stages. Pre-ore chlorite in the Athabasca involves the chlortization of biotite and has a typical clinochlore composition (Alexandre et al., 2005; Cloutier et al., 2009). Post-ore chlorite manifests itself as vein chlorite and has a composition near a typical sudoite (Alexandre et al., 2005; Cloutier et al., 2009). The chemical composition of chlorite was plotted in Fe-Al-Mg ternary space. Chlorite geothermometry was also determined and results are summarized in Appendix J.

Two distinctive groups of chlorite were identified based on different morphologies in altered porphyry samples. The first group was seen replacing Fe-Mg minerals and the second group was seen as veins and in fractures. All chlorite analyses plot in the Athabasca pre-ore

stability field suggesting that the chlorites in altered porphyry samples have a similar chemical composition to those in the Athabasca Basin (Figure J.1).

The temperature of formation (T_1) for chlorite was calculated using the formula derived by Kranidiotis and MacLean (1987). In order to determine the temperature of formation, Kranidiotis and McLean (1987) calculated a corrected Al^{IV} value (Equation A.3; Al_C^{IV}) as follows:

$$Al_C^{IV} = Al^{IV} + 0.7[\frac{Fe}{(Fe + Mg)}] . \quad\quad\quad\text{(Equation A.3)}$$

From there, T_1 (in ℃) is computed as follows (Equation A.4):

$$T_1 = 106\ Al_C^{IV} + 18 . \quad\quad\quad\text{(Equation A.4)}$$

The average temperature of formation for chlorite was in a range between 215 ℃ and 309 ℃ with an average temperature of 264 ℃. This was interpreted to be in the range of low-grade metamorphism. Therefore these chlorites were determined to have formed through the metamorphism of Fe-Mg minerals such as biotite or hornblende.

Fluorapatite

Electron microprobe analysis concentrated on imaging of fluorapatite from altered porphyry samples collected in 2011. Fluorapatite occurs as an accessory mineral in the porphyry samples and displays fine scale oscillatory zoning. Additional quantitative electron microprobe analysis was undertaken for the purpose of determining differences in chemical composition between fluorapatite rims, cores, and non-zoned fluorapatites going along and towards the Hottah porphyry – Conjuror Bay Formation unconformity. The following operating conditions were used in the analysis of fluorapatites: accelerator voltage of 15 kV, beam current of 50 nA, beam diameter of 10 μm, count times of 30 s for major and trace elements. Standards included quartz (Si), Th metal (Th), U metal (U), Y-Al garnet (Y and Al), Smithsonian $LaPO_4$ (La), Smithsonian $CePO_4$ (Ce), Smithsonian $PrPO_4$ (Pr), Smithsonian $NdPO_4$ (Nd), Smithsonian $SmPO_4$ (Sm), Smithsonian $GdPO_4$ (Gd), Smithsonian $DyPO_4$ (Dy), magnetite (Fe), diopside (Mg), bustamite (Mn), Durango apatite (Ca), jadeite (Na), Durango apatite (P), fluorite (F), and tugtapite (Cl). Appendix K summarizes the chemical composition of fluorapatite. No significant variations in chemical composition between cores, rims, and non-zoned fluorapatites were detected therefore data were discarded.

Fe oxide, Ti oxide, and Fe-Ti oxide

Electron microprobe analysis concentrated on imaging of Fe oxide, Ti oxide, and Fe-Ti oxide from altered porphyry samples collected in 2011. Oxide minerals occur as an accessory mineral in the porphyry samples. Additional quantitative electron microprobe analysis was undertaken for the purpose of determining the chemical composition of oxide minerals. The following operating conditions were used in the analysis of oxides: accelerator voltage of 15 kV, beam current of 50 nA, beam diameter of 10 μm, count times of 30 s for major and trace elements. Standards included quartz (Si), rutile (Ti), Th metal (Th), U metal (U), Al-Y garnet (Al), Al-Y garnet (Y), Smithsonian $LaPO_4$ (La), Smithsonian $CePO_4$ (Ce), Smithsonian $PrPO_4$ (Pr), Smithsonian $NdPO_4$ (Nd), Smithsonian $SmPO_4$ (Sm), Smithsonian $GdPO_4$ (Gd), Smithsonian $DyPO_4$ (Dy), magnetite (Fe), diopside (Mg), and bustamite (Mn). Appendix L summarizes the chemical composition of fluorapatite. Iron oxide Fe wt. % values are between 72.72 to 76.15 wt.%. All other measured elements fall below detection limit. Titanium oxide Ti wt.% values are between 55.4 to 59.17 wt.% and Fe wt.% values are between 0.23 wt.% to 2.08 wt.%. All other measured elements fall below detection limit. Iron-titanium oxide Fe wt.% values are between 69.5 and 73.56 wt.% and Ti wt.% values are between 1.54 and 5.47 wt.%. All other measured elements are below detection limit.

Table B.1 Whole-rock, major-, trace-, and rare earth element geochemical analyses from Hottah porphyry and Conjuror Bay quartz arenite specifically least-altered porphyry, altered porphyry in the zone of leaching, altered porphyry in the zone of oxidation, porphyry clasts, weathering rinds, quartz arenite, and strong altered mafic dyke. Samples were collected during the summer of 2011.

Samples	Description	SiO$_2$	Al$_2$O$_3$	Fe$_2$O$_3$(T)	MnO	MgO	CaO	Na$_2$O	K$_2$O
Unit Symbol		%	%	%	%	%	%	%	%
Detection Limit		0.01	0.01	0.01	0.001	0.01	0.01	0.01	0.01
Analysis Method		FUS-ICP	FUS-ICP	FUS-ICP	FUS-ICP	FUS-ICP	FUS-ICP	FUS-ICP	FUS-ICP
9705-(1)-A-11	Altered porphyry	70.36	13.13	5.08	0.045	2.07	0.31	0.26	5.02
9705-(2)-A-11	Altered porphyry	68.07	13.99	5.45	0.037	2.14	0.28	0.23	4.81
9706-11	Quartz arenite	96.51	1.8	1.06	0.013	0.22	0.04	0.08	0.64
9708-(2)-(A)-11	Porphyry clast	73.39	13.93	2.74	0.013	1	0.25	0.1	4.89
9708-(2)-(B)-11	Quartz arenite	90.09	5.03	1.64	0.009	0.35	0.07	0.07	1.73
9708-(2)-(C)-11	Weathering rind	77.5	11	2.6	0.013	0.76	0.2	0.08	3.72
9708-(1)-A-C-(A)-11	Porphyry clast	74.82	13.4	1.89	0.012	1.73	0.19	0.1	4.23
9708-(1)-A-C-(B)-11	Quartz arenite	91.25	4.3	0.89	0.008	0.35	0.09	0.05	1.54
9710-11	Altered porphyry	69.57	13.24	5.12	0.053	1.49	0.45	2.09	5.08
9715-11	Altered porphyry	69.75	14.11	5.32	0.04	1.66	0.35	3.2	3.08
9716-(A)-11	Altered porphyry	67.18	14.29	6.03	0.019	1.63	0.19	0.13	5.32
9716-(B)-11	Altered porphyry	70.55	13.32	4.55	0.026	1.81	0.26	0.4	4.85
9722-11	Altered porphyry	70.95	12.54	5.09	0.043	3.48	0.23	0.09	3.37
9723-11	Altered porphyry	70.43	13.21	6.04	0.029	2.8	0.34	0.72	3.66
9726-11	Least-altered porphyry	72.6	13.07	3.4	0.029	3.5	0.21	1.77	2.86
9727-A-G-(A)-11	Quartz arenite	93.25	3.98	0.96	0.007	0.26	0.06	0.06	1.42
9727-A-G-(B)-11	Weathering rind	81.25	10.41	2.11	0.013	0.6	0.04	0.08	3.71
9727-A-G-(C)-11	Porphyry clast	73.19	14.5	2.51	0.012	0.79	0.12	0.1	5.11
9728-11	Quartz arenite	95.91	2	0.5	0.01	0.14	0.02	0.05	0.75
9731-(A)-11	Mafic dyke	48.12	18.43	17.18	0.032	1.23	0.61	0.51	6.5
9731-(B)-11	Mafic dyke	60.84	20.7	3.95	0.014	1.38	0.26	0.11	7.52
9731-(C)-11	Mafic dyke	48.01	19.41	18.83	0.016	1.11	0.28	0.12	7.25

Samples	Description	TiO$_2$	P$_2$O$_5$	LOI	Total	Sc (ppm)	Be	V	Ba
Unit Symbol		%	%	%	%	ppm	ppm	Ppm	ppm
Detection Limit		0.001	0.01		0.01	1	1	5	3
Analysis Method		FUS-ICP	FUS-ICP	FUS-ICP	FUS-ICP	FUS-ICP	FUS-ICP	FUS-ICP	FUS-ICP
9705-(1)-A-11	Altered porphyry	0.672	0.16	3.3	100.4	11	4	34	493
9705-(2)-A-11	Altered porphyry	0.73	0.2	3.42	99.37	12	5	36	308
9706-11	Quartz arenite	0.04	< 0.01	0.39	100.8	1	< 1	8	26
9708-(2)-(A)-11	Porphyry clast	0.681	0.2	2.33	99.53	14	5	42	231
9708-(2)-(B)-11	Quartz arenite	0.153	0.04	0.77	99.95	5	2	16	92
9708-(2)-(C)-11	Weathering rind	0.6	0.15	1.75	98.37	10	4	35	189
9708-(1)-A-C-(A)-11	Porphyry clast	0.687	0.13	2.37	99.56	12	3	37	260
9708-(1)-A-C-(B)-11	Quartz arenite	0.051	0.06	0.62	99.2	4	1	15	75
9710-11	Altered porphyry	0.659	0.14	1.77	99.67	12	3	38	974
9715-11	Altered porphyry	0.67	0.16	1.76	100.1	12	3	38	392
9716-(A)-11	Altered porphyry	0.74	0.14	2.53	98.19	14	6	41	300
9716-(B)-11	Altered porphyry	0.686	0.2	2.52	99.17	11	6	33	273
9722-11	Altered porphyry	0.659	0.19	3.16	99.79	11	4	29	226
9723-11	Altered porphyry	0.669	0.17	2.72	100.8	13	4	43	125
9726-11	Least-altered porphyry	0.509	0.12	2.77	100.9	11	3	29	78
9727-A-G-(A)-11	Quartz arenite	0.051	0.03	0.64	100.7	3	< 1	13	62
9727-A-G-(B)-11	Weathering rind	0.701	0.05	1.72	100.7	10	3	44	170
9727-A-G-(C)-11	Porphyry clast	0.73	0.1	2.24	99.41	13	4	48	217
9728-11	Quartz arenite	0.031	< 0.01	0.29	99.69	1	< 1	7	37
9731-(A)-11	Mafic dyke	1.426	0.17	3.98	98.19	43	6	228	215
9731-(B)-11	Mafic dyke	1.599	0.16	3.32	99.85	32	7	135	162
9731-(C)-11	Mafic dyke	1.557	0.17	2.99	99.74	52	7	277	173

Samples	Description	Sr	Y	Zr	Cr	Co	Ni	Cu	Zn
Unit Symbol		ppm	Ppm	ppm	ppm	ppm	ppm	Ppm	ppm
Detection Limit		2	2	4	20	1	20	10	30
Analysis Method		FUS-ICP	FUS-ICP	FUS-ICP	FUS-MS	FUS-MS	FUS-MS	FUS-MS	FUS-MS
9705-(1)-A-11	Altered porphyry	18	45	384	< 20	12	< 20	20	70
9705-(2)-A-11	Altered porphyry	14	49	461	30	21	< 20	10	120
9706-11	Quartz arenite	< 2	3	56	< 20	83	< 20	< 10	< 30
9708-(2)-(A)-11	Porphyry clast	8	50	407	20	19	< 20	10	130
9708-(2)-(B)-11	Quartz arenite	3	12	526	< 20	28	< 20	10	< 30
9708-(2)-(C)-11	Weathering rind	7	43	348	50	34	20	< 10	60
9708-(1)-A-C-(A)-11	Porphyry clast	7	39	391	< 20	7	< 20	< 10	130
9708-(1)-A-C-(B)-11	Quartz arenite	3	6	68	40	50	< 20	20	50
9710-11	Altered porphyry	64	47	365	< 20	50	< 20	< 10	70
9715-11	Altered porphyry	46	41	369	< 20	19	< 20	< 10	50
9716-(A)-11	Altered porphyry	12	54	400	< 20	9	< 20	< 10	40
9716-(B)-11	Altered porphyry	15	43	381	< 20	15	< 20	< 10	60
9722-11	Altered porphyry	7	45	346	< 20	28	< 20	< 10	80
9723-11	Altered porphyry	9	48	381	< 20	15	< 20	< 10	30
9726-11	Least-altered porphyry	20	61	353	< 20	18	< 20	< 10	40
9727-A-G-(A)-11	Quartz arenite	5	5	78	40	94	< 20	< 10	< 30
9727-A-G-(B)-11	Weathering rind	32	64	396	50	35	30	10	60
9727-A-G-(C)-11	Porphyry clast	43	49	414	< 20	8	< 20	< 10	100
9728-11	Quartz arenite	< 2	3	40	< 20	75	< 20	< 10	< 30
9731-(A)-11	Mafic dyke	39	22	121	110	13	70	60	190
9731-(B)-11	Mafic dyke	14	32	107	90	21	90	< 10	50
9731-(C)-11	Mafic dyke	12	17	110	110	19	80	< 10	< 30

Samples	Description	Ga	Ge	As	Rb	Nb	Mo	Ag	In
Unit Symbol		ppm	ppm	ppm	ppm	ppm	ppm	Ppm	ppm
Detection Limit		1	1	5	2	1	2	0.5	0.2
Analysis Method		FUS-MS	FUS-MS	FUS-MS	FUS-MS	FUS-MS	FUS-MS	FUS-MS	FUS-MS
9705-(1)-A-11	Altered porphyry	17	2	< 5	201	23	< 2	2.8	0.3
9705-(2)-A-11	Altered porphyry	18	2	< 5	219	19	< 2	3.5	< 0.2
9706-11	Quartz arenite	2	1	< 5	28	< 1	< 2	< 0.5	< 0.2
9708-(2)-(A)-11	Porphyry clast	18	2	< 5	245	16	< 2	2.9	< 0.2
9708-(2)-(B)-11	Quartz arenite	7	1	< 5	91	13	< 2	4	0.6
9708-(2)-(C)-11	Weathering rind	16	2	< 5	198	14	< 2	2.3	< 0.2
9708-(1)-A-C-(A)-11	Porphyry clast	14	1	< 5	194	17	< 2	2.7	< 0.2
9708-(1)-A-C-(B)-11	Quartz arenite	7	1	< 5	84	8	< 2	0.6	0.3
9710-11	Altered porphyry	18	2	< 5	167	18	< 2	2.3	< 0.2
9715-11	Altered porphyry	16	1	< 5	120	18	< 2	2.6	< 0.2
9716-(A)-11	Altered porphyry	20	2	< 5	226	19	< 2	3.1	< 0.2
9716-(B)-11	Altered porphyry	17	2	< 5	199	15	< 2	2.7	< 0.2
9722-11	Altered porphyry	17	2	< 5	155	15	< 2	2.5	< 0.2
9723-11	Altered porphyry	19	2	< 5	156	18	< 2	3.1	< 0.2
9726-11	Least-altered porphyry	20	2	< 5	102	19	< 2	1.4	< 0.2
9727-A-G-(A)-11	Quartz arenite	5	1	< 5	72	< 1	< 2	< 0.5	< 0.2
9727-A-G-(B)-11	Weathering rind	15	2	< 5	188	19	< 2	3.1	< 0.2
9727-A-G-(C)-11	Porphyry clast	19	2	< 5	289	20	< 2	3.6	< 0.2
9728-11	Quartz arenite	2	< 1	< 5	38	< 1	< 2	< 0.5	< 0.2
9731-(A)-11	Mafic dyke	20	2	26	332	7	< 2	< 0.5	< 0.2
9731-(B)-11	Mafic dyke	18	2	< 5	410	4	< 2	< 0.5	< 0.2
9731-(C)-11	Mafic dyke	20	2	< 5	364	4	< 2	< 0.5	< 0.2

Samples	Description	Sn	Sb	Cs	La	Ce	Pr	Nd	Sm
Unit Symbol		ppm	ppm	ppm	ppm	ppm	ppm	Ppm	ppm
Detection Limit		1	0.5	0.5	0.1	0.1	0.05	0.1	0.1
Analysis Method		FUS-MS	FUS-MS	FUS-MS	FUS-MS	FUS-MS	FUS-MS	FUS-MS	FUS-MS
9705-(1)-A-11	Altered porphyry	423	< 0.5	3.5	75.2	157	17.4	63.1	12.5
9705-(2)-A-11	Altered porphyry	17	< 0.5	4.8	111	234	26.2	95	17.8
9706-11	Quartz arenite	6	< 0.5	< 0.5	2.6	4.9	0.56	1.8	0.5
9708-(2)-(A)-11	Porphyry clast	12	< 0.5	4.7	33.8	74.6	8.8	33.7	7.7
9708-(2)-(B)-11	Quartz arenite	829	< 0.5	1.4	23.9	50.3	5.67	20.8	4.3
9708-(2)-(C)-11	Weathering rind	8	< 0.5	3.5	89.1	187	20.6	74.8	14.2
9708-(1)-A-C-(A)-11	Porphyry clast	7	< 0.5	3	15.2	37.5	4.6	19	5
9708-(1)-A-C-(B)-11	Quartz arenite	448	< 0.5	0.9	14.3	32	3.7	13.6	2.6
9710-11	Altered porphyry	8	< 0.5	1.6	74.3	151	16.3	57.1	10.9
9715-11	Altered porphyry	11	< 0.5	2.4	58	121	13.3	47.6	9.2
9716-(A)-11	Altered porphyry	36	< 0.5	3.8	79.9	164	18	64.3	12.1
9716-(B)-11	Altered porphyry	6	< 0.5	3.6	112	234	25.7	90.8	15.9
9722-11	Altered porphyry	6	< 0.5	3.8	95.8	206	22.8	80.1	14.5
9723-11	Altered porphyry	29	< 0.5	4.1	80.5	162	17.3	61.1	11.7
9726-11	Least-altered porphyry	17	1.4	2.4	72.2	142	15.6	53	10.5
9727-A-G-(A)-11	Quartz arenite	5	< 0.5	1.2	8.5	19.8	2.42	9.1	1.8
9727-A-G-(B)-11	Weathering rind	65	< 0.5	3.6	83.9	167	18.2	66.4	13.8
9727-A-G-(C)-11	Porphyry clast	9	< 0.5	6.7	47.1	114	14.3	58.7	12.9
9728-11	Quartz arenite	4	< 0.5	0.6	3	5.2	0.56	1.8	0.4
9731-(A)-11	Mafic dyke	15	2.6	9.3	23.4	47.5	5.18	19.8	4
9731-(B)-11	Mafic dyke	8	1.1	10.3	6.2	13.2	1.65	7.3	2.8
9731-(C)-11	Mafic dyke	< 1	2.2	10.5	7.3	15.7	1.84	7.8	2.3

Samples	Description	Eu	Gd	Tb	Dy	Ho	Er	Tm	Yb
Unit Symbol		ppm	ppm	ppm	ppm	ppm	ppm	Ppm	ppm
Detection Limit		0.05	0.1	0.1	0.1	0.1	0.1	0.05	0.1
Analysis Method		FUS-MS	FUS-MS	FUS-MS	FUS-MS	FUS-MS	FUS-MS	FUS-MS	FUS-MS
9705-(1)-A-11	Altered porphyry	1.85	10.7	1.5	8.5	1.7	4.8	0.77	4.9
9705-(2)-A-11	Altered porphyry	2.34	13	1.7	8.8	1.8	5.1	0.78	5
9706-11	Quartz arenite	0.07	0.5	< 0.1	0.5	0.1	0.3	0.05	0.4
9708-(2)-(A)-11	Porphyry clast	1.02	8.7	1.6	8.8	1.8	4.9	0.77	5
9708-(2)-(B)-11	Quartz arenite	0.55	3	0.4	2.2	0.4	1.2	0.2	1.4
9708-(2)-(C)-11	Weathering rind	1.94	11.3	1.6	8.6	1.7	4.7	0.71	4.6
9708-(1)-A-C-(A)-11	Porphyry clast	0.54	5.7	1	6.3	1.4	4.3	0.69	4.9
9708-(1)-A-C-(B)-11	Quartz arenite	0.26	1.7	0.2	1.3	0.3	1	0.18	1.4
9710-11	Altered porphyry	1.51	9.4	1.5	8.5	1.7	4.9	0.77	5
9715-11	Altered porphyry	1.3	8.4	1.3	7.3	1.5	4.4	0.67	4.6
9716-(A)-11	Altered porphyry	1.86	11	1.7	9.7	2	5.5	0.84	5.4
9716-(B)-11	Altered porphyry	2.13	11.5	1.5	7.7	1.5	4.5	0.66	4.5
9722-11	Altered porphyry	1.89	11.3	1.6	8.5	1.7	4.8	0.74	4.7
9723-11	Altered porphyry	1.68	10.4	1.6	9	1.8	5.2	0.82	5.4
9726-11	Least-altered porphyry	1.66	10.2	1.8	11.1	2.3	6.1	0.92	6
9727-A-G-(A)-11	Quartz arenite	0.2	1.2	0.1	0.7	0.1	0.4	0.06	0.4
9727-A-G-(B)-11	Weathering rind	1.87	12.5	2.1	12.1	2.4	6.5	0.96	6.3
9727-A-G-(C)-11	Porphyry clast	1.47	10.2	1.6	8.8	1.8	5	0.8	5.2
9728-11	Quartz arenite	0.06	0.4	< 0.1	0.4	< 0.1	0.3	< 0.05	0.3
9731-(A)-11	Mafic dyke	1.2	4.1	0.7	4.2	0.9	2.6	0.42	2.9
9731-(B)-11	Mafic dyke	1.55	5.2	0.9	5.9	1.1	3	0.43	2.8
9731-(C)-11	Mafic dyke	0.83	2.8	0.5	3.4	0.7	2.3	0.37	2.6

Samples	Description	Lu	Hf	Ta	W	Tl	Pb	Bi	Th
Unit Symbol		ppm	ppm	ppm	ppm	ppm	ppm	Ppm	ppm
Detection Limit		0.04	0.2	0.1	1	0.1	5	0.4	0.1
Analysis Method		FUS-MS	FUS-MS	FUS-MS	FUS-MS	FUS-MS	FUS-MS	FUS-MS	FUS-MS
9705-(1)-A-11	Altered porphyry	0.79	9.7	11.1	96	0.9	12	0.5	29.5
9705-(2)-A-11	Altered porphyry	0.83	11.3	2.1	220	0.9	9	< 0.4	30.4
9706-11	Quartz arenite	0.06	1.5	1.1	1420	0.1	< 5	< 0.4	3
9708-(2)-(A)-11	Porphyry clast	0.79	9.5	1.8	181	0.9	10	0.4	29.6
9708-(2)-(B)-11	Quartz arenite	0.23	12.4	19.1	566	0.4	6	< 0.4	13.4
9708-(2)-(C)-11	Weathering rind	0.76	8.3	1.9	606	0.8	10	1	27.3
9708-(1)-A-C-(A)-11	Porphyry clast	0.83	9.7	1.8	115	0.9	10	< 0.4	30.6
9708-(1)-A-C-(B)-11	Quartz arenite	0.24	2	11.6	744	0.2	< 5	< 0.4	4
9710-11	Altered porphyry	0.79	9.3	2	469	0.9	22	< 0.4	28.9
9715-11	Altered porphyry	0.74	9.1	1.7	145	0.7	10	0.5	28.5
9716-(A)-11	Altered porphyry	0.87	9.7	2.4	95	0.9	9	0.8	31.2
9716-(B)-11	Altered porphyry	0.73	9.1	1.8	184	0.8	9	0.6	30
9722-11	Altered porphyry	0.77	8.6	1.7	100	0.6	7	< 0.4	29.3
9723-11	Altered porphyry	0.85	9.6	2.2	146	0.6	7	< 0.4	30.5
9726-11	Least-altered porphyry	0.94	8.6	1.8	196	0.3	9	< 0.4	29.2
9727-A-G-(A)-11	Quartz arenite	0.07	1.8	1.2	1630	0.3	< 5	< 0.4	3.1
9727-A-G-(B)-11	Weathering rind	1	9.8	3.3	615	0.8	14	0.8	33.4
9727-A-G-(C)-11	Porphyry clast	0.84	10.5	1.9	132	1.5	9	< 0.4	32.1
9728-11	Quartz arenite	0.06	1.1	1	1490	0.2	< 5	< 0.4	2.9
9731-(A)-11	Mafic dyke	0.48	3.1	0.6	60	1.2	34	1.7	6
9731-(B)-11	Mafic dyke	0.42	3	0.4	49	1.8	7	2.3	2.6
9731-(C)-11	Mafic dyke	0.43	2.8	0.3	44	1.3	10	3.2	2.8

Samples	Description	U	Ba/Sr	Th/U	$\Sigma LREE_N$[1]	Eu/Eu*[2]	CIA[3]	CIA - K[4]	PIA[5]
Unit Symbol		ppm							
Detection Limit		0.1							
Analysis Method		FUS-MS							
9705-(1)-A-11	Altered porphyry	8.6	27.389	3.430	1005.707	0.489	68.486	95.573	92.676
9705-(2)-A-11	Altered porphyry	8.8	22.000	3.455	1486.608	0.47	71.36	97.162	95.555
9706-11	Quartz arenite	1.8							
9708-(2)-(A)-11	Porphyry clast	10.4	28.875	2.846	497.219				
9708-(2)-(B)-11	Quartz arenite	3.6							
9708-(2)-(C)-11	Weathering rind	10.9	27.000	2.505	1184.777				
9708-(1)-A-C-(A)-11	Porphyry clast	11.2	37.143	2.732	256.506				
9708-(1)-A-C-(B)-11	Quartz arenite	1.8							
9710-11	Altered porphyry	8	15.219	3.613	951.359	0.456	58.43	77.151	66.379
9715-11	Altered porphyry	7.8	8.522	3.654	766.91	0.452	61.452	71.889	66.138
9716-(A)-11	Altered porphyry	9.8	25.000	3.184	1043.42	0.493	70.49	98.456	97.441
9716-(B)-11	Altered porphyry	9.2	18.200	3.261	1460.531	0.482	69.298	95.334	92.526
9722-11	Altered porphyry	10.3	32.286	2.845	1279.699	0.451	76.938	99.12	98.764
9723-11	Altered porphyry	9.5	13.889	3.211	1022.745	0.466	71.147	90.445	86.889
9726-11	Least-altered porphyry	8.9	3.900	3.281	911.617	0.49	68.173	81.3	76.841
9727-A-G-(A)-11	Quartz arenite	1.1							
9727-A-G-(B)-11	Weathering rind	15.5	5.313	2.155	1083.085				
9727-A-G-(C)-11	Porphyry clast	14.4	5.047	2.229	770.889				
9728-11	Quartz arenite	1.2							
9731-(A)-11	Mafic dyke	1.5	5.513	4.000					
9731-(B)-11	Mafic dyke	0.9	11.571	2.889					
9731-(C)-11	Mafic dyke	1	14.417	2.800					

[1] $\Sigma LREE_N = La_N$ to Eu_N

[2] $Eu/Eu* = Eu_N /(Sm_N + Gd_N)^{0.5}$

[3] $CIA = ((Al_2O_3)/(Al_2O_3 + CaO* + Na_2O + K_2O)) \times 100$

[4] $CIA - K = ((Al_2O_3)/(Al_2O_3 + CaO* + Na_2O)) \times 100$

[5] $PIA = ((Al_2O_3 - K_2O)/(Al_2O_3 + CaO* + Na_2O - K_2O)) \times 100$

Table B.2 Summary of Petrographic observations from altered and least-altered porphyry samples. Samples were collected during the summer of 2011.

Sample	Unit	Description	
BLU 9726-11	Hottah porphyry	Groundmass 70% Plagioclase Feldspar phenocrysts 20% Quartz phenocrysts 5% Opaques 5%	• Least-altered sample • Minor sericitic alteration of plagioclase phenocrysts • Minor sericitc alteration of groundmass
BLU 9728-11	Quartz arenite of the Conjuror Bay Formation	>98% detrital Quartz	• Heavily fractured quartz arenite filled with late quartz veins • Minor amounts of altered feldspars, sericite, and zircon
BLU 9722-11	Hottah porphyry	Groundmass 70% Plagioclase Feldspar phenocrysts 20% Quartz phenocrysts 5% Opaques 5%	• Alteration of plagioclase phenocrysts replaced by sericite • Quartz phenocrysts look unaltered • Groundmass is altered but not to the same extent as phenocrysts • Multiple generations of opaques • Alteration in concentrated along fractures
BLU 9716-II-11	Hottah porphyry	Groundmass 70% Plagioclase Feldspar phenocrysts 20% Quartz phenocrysts 5% Opaques 5%	• Some clay alteration feldspar phenocrysts • Phenocrysts completely replaced by sericite • Multiple generatons of opaques • Chlorite replacing Fe-Mg minerals
BLU 9716-I-11	Hottah porphyry	Groundmass 80% Plagioclase Feldspar phenocrysts 10% Quartz phenocrysts 5% Opaques 5%	• Feldspar relicts replaced by sericite and clay • Abundant quartz veins • Chlorite and hematite in the groundmass • Groundmass heavily altered but still visible

			unlike phenocrysts
BLU 9708-B-11	Hottah porphyry	Groundmass 65% Plagioclase Feldspar phenocrysts 25% Quartz phenocrysts 5% Opaques 5%	• Feldspar phenocrusts completely replaced by sericite • Quartz phenocrysts appear unaltered • Not as much clay alteration compared to previous sample • Quartz and chlorite veins • Accessory apatite and zircon
BLU 9708-A-11	Hottah porphyry	Quartz arenite Weathering Rind Altered Porphyry	• Quartz arenite has sercite, opaques, and altered feldspars between grains • Weathering rind is heavily altered with feldspar completely replaced by sericite. Abundant opaques and quartz and chlorite veins.
BLU 9706-11	Quartz arenite of the Conjuror Bay Formation	>98% detrital Quartz	• Pure quartz arenite with accessory sericite, opaques, and zircon
BLU 9705-B-II-11	Hottah porphyry	Groundmass 65% Plagioclase Feldspar phenocrysts 20% Quartz phenocrysts 5% Opaques 10%	• Less altered but still heavily altered porphyry surrounding oxidized porphyry • Feldspar phenocrysts replaced by sericite • A lot of opaques • Quartz, chlorite, and opaque veins
BLU 9705-B-I-11	Hottah porphyry	Groundmass 70% Plagioclase Feldspar phenocrysts 20% Quartz phenocrysts 5% Opaques 5%	• Heavily altered porphyry • Plagioclase phenocrysts completely replaced by sericite • Groundmass recognizable is mostly quartz, alkali feldspar, and chlorite • Oxide veins
BLU 9705-A-1-II-11	Hottah porphyry	Groundmass 70% Plagioclase Feldspar	• Heavily oxidized

		phenocrysts 20% Quartz phenocrysts 5% Opaques 5%	porphyry • Groundmass not recognizable • Abundant quartz veins • Feldspars phenocrysts altered to clay + sericite
BLU 9705-A-1-I-11	Hottah porphyry	Groundmass 75% Plagioclase Feldspar phenocrysts 15% Quartz phenocrysts 5% Opaques 5%	• Heavily oxidized porphyry plus less altered but still altered porphyry • Alteration rim consists of quartz • Oxidized porphyry phenocrysts altered to clay plus sericite and groundmass is barely recognizable • Less altered porphyry has phenocyrsts of plagioclase replaced by sericite
BLU 9729-11	Siltstone of the Conjuror Bay Formation	Groundmass 70% Plagioclase Feldspar phenocrysts 20% Quartz phenocrysts 5% Opaques 5%	• Some large quartz and opaque grains followed by very fine-grained material. • Abundant chlorite and illite in groundmass
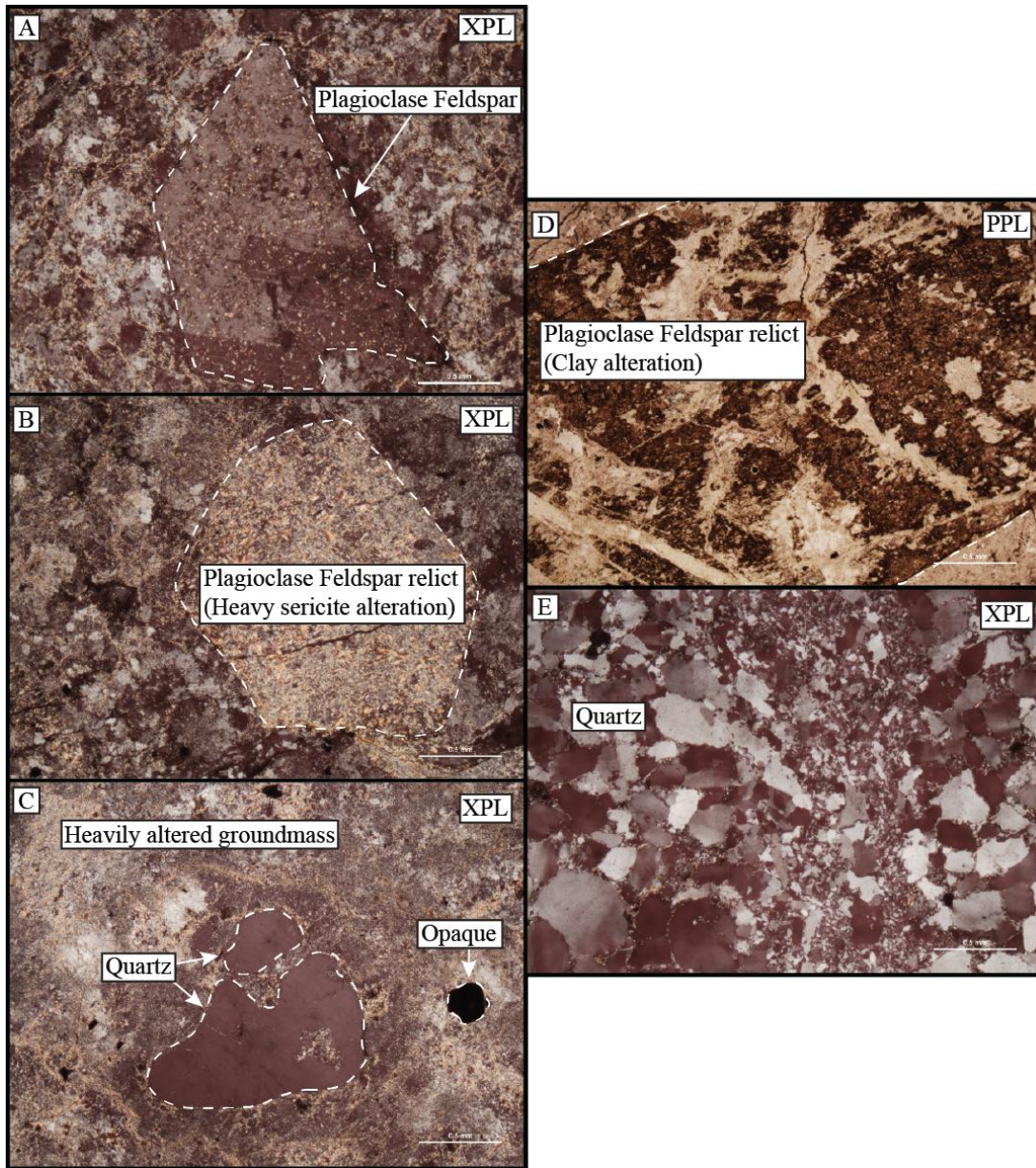
Figure B.2 Photomicrograph images from least-altered and heavily altered porphyry samples. Samples collected during the summer of 2011. (A) Least-altered porphyry sample (Sample BLU 9726-11) showing phenocrysts of plagioclase feldspar showing minor sericite alteration. Groundmass is composed of altered K-feldspar and quartz. (B) Highly altered plagioclase feldspar relict completely replaced by sericite (Sample BLU 9722-11). (C) Quartz phenocrysts altered porphyry sample. Quartz appears unaltered while groundmass is heavily altered and not recognizable (Sample BLU 9709-B-11). (D) Plagioclase feldspar in the "zone of oxidation." Feldspar phencorysts have been altered to clay minerals (Sample BLU 9705-A-1-I-11). (E) Heavily fractured quartz arenite of the Conjuror Bay Formation. Fractures filled with quartz (Sample BLU 9728-11).

Table B.3 Summary of percent changes of $\Sigma LREE_N$, $\Sigma MREE_N$, and $\Sigma HREE_N$ relative to the least-altered porphyry sample. Rare earth elements normalized to C1 chondrites from Sun and McDonough, 1984

Description	Percent Change in $\Sigma LREE_N$ relative to least-altered porphyry	Percent Change in $\Sigma MREE_N$ relative to least-altered porphyry	Percent Change in $\Sigma HREE_N$ relative to least-altered porphyry
Altered Porphyry	14.8%	-0.5%	-15.9%
Porphyry Clast	-46.6%	-23.8%	-17.4%
Weathering Rind	24.0%	14.1%	-8.2%

Table B.4 Possible combinations of $\varepsilon_{i,w}$ vs. $\tau_{j,w}$ to determine the most appropriate immobile element of Al_2O_3, TiO_2, and Zr

$\varepsilon(i,w)$	$\varepsilon(i,w)$	$\varepsilon(i,w)$	$\tau(j,w)$	$\tau(j,w)$	$\tau(j,w)$	$\tau(j,w)$	$\tau(j,w)$	$\tau(j,w)$
Al	Ti	Zr	Ti	Ti	Al	Al	Zr	Zr
			$\varepsilon(Al)$	$\varepsilon(Zr)$	$\varepsilon(Zr)$	$\varepsilon(Ti)$	$\varepsilon(Ti)$	$\varepsilon(Al)$
-0.030	-0.266	-0.084	0.322	0.249	-0.056	-0.244	-0.199	0.059
-0.038	-0.277	-0.072	0.330	0.283	-0.035	-0.248	-0.221	0.036
0.0363	-0.227	-0.151	0.340	0.098	-0.180	-0.254	-0.089	0.220
0.114	-0.153	0.028	0.314	0.214	-0.077	-0.239	-0.176	0.083
0.046	-0.225	0.024	0.349	0.321	-0.021	-0.259	-0.243	0.022
-0.007	-0.236	-0.070	0.300	0.218	-0.064	-0.231	-0.179	0.068
0	0	0	0	0	0	0	0	0

Table B.5 Mass Balance Calculations for Major-, Trace-, and Rare Earth Elements from Hottah Porphyry assuming Zr to be Immobile

Density	ε(I,w)	Distance	τ(j,w)	τ(j,w)	τ(j,w)	τ(j,w)	τ(j,w)	τ(j,w)	τ(j,w)	τ(j,w)	τ(j,w)	τ(j,w)	τ(j,w)	τ(j,w)	τ(j,w)
	Zr	m	SiO_2	$Fe_2O_3(T)$	MgO	CaO	Na_2O	K_2O	Ba	Sr	Rb	La	Ce	Eu	Er
			ε(Zr)	ε(Zr)	ε(Zr)	ε(Zr)	ε(Zr)	ε(Zr)	ε(Zr)	ε(Zr)	ε(Zr)	ε(Zr)	ε(Zr)	ε(Zr)	ε(Zr)
2.67	-0.084	4	-0.100	0.240	-0.521	0.147	-0.791	0.571	2.243	-0.305	0.808	0.437	0.527	0.189	-0.317
2.51	-0.072	5	-0.183	0.565	-0.589	-0.202	-0.935	0.642	2.394	-0.471	0.955	-0.024	0.019	-0.011	-0.204
2.38	-0.151	12	-0.282	0.227	-0.532	0.021	-0.900	0.288	2.024	-0.464	0.644	0.177	0.261	0.079	-0.360
2.36	0.028	12.5	-0.109	0.373	-0.456	0.357	-0.865	0.614	4.810	-0.173	0.812	-0.043	0.016	0.024	-0.277
2.63	0.024	37.1	-0.003	0.527	0.014	0.117	-0.948	0.202	1.956	-0.643	0.550	0.354	0.480	0.161	-0.197
2.63	-0.07	73	-0.101	0.646	-0.259	0.500	-0.623	0.186	0.485	-0.583	0.417	0.033	0.057	-0.062	-0.210
2.64	0	160	0	0	0	0	0	0	0	0	0	0	0	0	0

Table C.1 Summary of 16 Diamond Drill Holes on the Cormac (Tatie) claims from 1955 (Modified from Grady, 1955).

Diamond Drill Hole (D.D.H.) Number	Notes
D.D.H. # C1	Quartz arenite fractured filled with chlorite and hematite Hematite common with uranium minerals
D.D.H. # C2	Quartz arenite fractured and filled with hematite, chlorite and secondary uranium minerals
D.D.H. # C3	Fractured quartz arenite filled with hematite Contact between feldspar porphyry and quartz arenite is fractured and contains hematite and chlorite Feldspar porphyry is highly chloritized
D.D.H. # C4	Quartz feldspar with chlorite Quartz arenite with few fractures Fractured quartz arenite with hematite and pitchblende
D.D.H. # C6	Quartz arenite fractured filled with hematite and silica Massive quartz arenite Heavily fractured quartz arenite at contact with feldspar porphyry Highly chloritized feldspar porphyry with little phenocrysts of quartz
D.D.H. # C7	Highly chloritized feldspar porphyry Massive quartz arenite Brecciated quartz arenite filled with hematite and quartz
D.D.H. # C8	Massive quartz arenite Porphyry inclusions in the quartz arenite Chloritized feldspar porphyry with phenocrysts of quartz and feldspar
D.D.H. # C9	Massive quartz arenite Heavily fractured quartz arenite with hematite and chlorite
D.D.H. # C10	Massive quartz arenite with little fractures Fractured quartz arenite containing disseminated and massive pitchblende with hematite, chlorite, and cobaltite
D.D.H. # C11	Massive quartz arenite Fractured quartz arenite with quartz and minor hematite
D.D.H. # C12	Unfractured quartz arenite Minor fracturing with red hematite in fractures Chlorite with hematite and pitchblende Minor fracturing in quartz arenite
D.D.H. # C13	Feldspar porphyry Fractured quartz arenite filled with hematite, chlorite and minor pitchblende
D.D.H. # C14	Feldspar porphyry Fractured zone with massive pitchblende, hematite, and chlorite
D.D.H. # C15	Fractured zone with porphyry and quartz arenite Massive quartz arenite
D.D.H. # C16	Little fractured quartz arenite Brecciated quartz aenite with chlorite and hematite

Table D.1 Chemical composition data of uranium oxides from the Bee (A1090) and Tatie (A1709) Claims, Beaverlodge Lake, NT, Canada
*concentrations reported as wt.%

Sample	Sample	Si	Th	U	Al	Y	Fe	Mg	Ca	Pb	P	O	Total	Method 1	Method 2	Method 3	Error
A1090-1	Bee	0.10	0.06	79.02	0.03	0.69	0.26	0	1.21	3.97	0.03	11.88	97.26	397	347.99	379.21	19.85
A1090-2	Bee	0.45	0	75.8	0.15	0.58	2.72	0	1.57	3.13	0.04	12.7	97.15	313	287.37	311.76	15.65
A1090-3	Bee	0	0	76.31	0	0.57	0.10	0	0.97	4.19	0.02	11.18	93.35	419	379.38	414.55	20.95
A1090-4	Bee	0.13	0	81.7	0.05	0.55	0.36	0	1.52	3.67	0.02	12.36	100.36	367	312.02	339.15	18.35
A1090-5	Bee	0.17	0	80.12	0	0.47	0.45	0	1.74	3.24	0.03	12.21	98.44	324	281.56	305.32	16.2
A1090-6	Bee	0	0	78.66	0	0.54	0.27	0	1.06	3.81	0.01	11.54	95.91	381	335.81	365.69	19.05
AVG		0.14	0.010	78.60	0.04	0.57	0.69	0	1.350	3.67	0.030	11.978	97.078	366.83	324.02	352.61	18.34
STDEV		0.17	0.024	2.24	0.06	0.07	1.00	0	0.300	0.41	0.010	0.558	2.363	41.39	37.60	41.96	2.07

Sample	Sample	Si	Th	U	Al	Y	Fe	Mg	Ca	Pb	P	O	Total	Method 1	Method 2	Method 3	Error
A1709-1	Tatie	0.10	0	72.75	0	0.77	0.20	0	0.8	18.55	0.01	11.92	105.1	1855	1598.92	1925.12	92.75
A1709-2	Tatie	0.10	0	70.11	0.00	0.67	0.18	0	0.62	16.75	0.01	11.33	99.78	1675	1509.03	1803.77	83.75
A1709-3	Tatie	0.05	0	69.41	0.00	0.61	0.180	0	0.46	15.22	0	10.97	96.92	1522	1397.51	1655.54	76.1
A1709-4	Tatie	0.09	0	70.8	0.00	0.58	0.18	0	0.68	15.1	0.02	11.29	98.74	1510	1363.04	1610.24	75.5
A1709-5	Tatie	0.04	0	71.63	0	0.56	0.14	0	0.4	15.31	0.02	11.24	99.35	1531	1365.69	1613.72	76.55
A1709-6	Tatie	0.07	0	70.85	0.01	0.59	0.12	0	0.45	15.26	0.03	11.21	98.59	1526	1375.17	1626.15	76.3
A1709-7	Tatie	0.10	0.04	71.59	0.01	0.71	0.15	0	0.42	15.86	0.02	11.41	100.33	1586	1410.46	1672.24	79.3
A1709-8	Tatie	0.06	0.00	68.01	0.12	0.62	0.1	0.06	0.52	14.71	0.02	10.94	95.19	1471	1380.38	1633.00	73.55
AVG		0.08	0.01	70.64	0.02	0.64	0.16	0.008	0.540	15.845	0.010	11.289	99.250	1584.50	1425.03	1692.47	79.23
STDEV		0.03	0.02	1.47	0.04	0.07	0.04	0.023	0.140	1.253	0.010	0.304	2.886	125.349	84.606	112.88	6.267

Table E.1 Chemical composition data of uranium silicate (coffinite) from the Tatie (A1709) Claim, Beaverlodge Lake, NT, Canada
*concentrations reported as wt.%

Sample	Sample	Si	Ti	Th	U	Al	Y	Fe	Mg	Ca	Pb	Na	K	O	Total
A1709-1	Tatie	0	0	0	87.99	0.01	0.01	0	0.02	0	0	0.03	0	11.86	99.92
A1709-2	Tatie	0	0	89.01	0	0	0	0	0.01	0.00	0.18	0.05	0.07	12.32	101.64
A1709-3	Tatie	4.02	0	0.02	58.2	0.05	0.09	0.35	0	1.91	3.96	0.03	0.12	13.68	82.43
A1709-4	Tatie	2.94	0.03	0.01	68.55	0.08	0	0.80	0.06	1.44	3.16	0	0	13.75	90.83
A1709-5	Tatie	2.96	0.05	0	67.42	0.14	0.10	1.10	0	1.59	3.74	0	0.08	13.88	91.06
A1709-6	Tatie	4.61	0.03	0.02	67.1	0.07	0.06	0.56	0.05	1.93	2.85	0.03	0	15.56	92.85
A1709-7	Tatie	2.82	0	0	65.34	0.07	0.06	1.08	0	2.10	7.69	0.07	0.50	13.95	93.68
A1709-8	Tatie	3.14	0	0	67.91	0.06	0.06	0.30	0	1.19	4.19	0.06	0.07	13.69	90.66
A1709-9	Tatie	4.77	0	0	65.87	0.03	0.66	0.57	0.08	3.43	1.82	0.02	0	16.23	93.49
A1709-10	Tatie	4.66	0	0.03	65.04	0.02	0.40	0.83	0.03	2.92	1.05	0.08	0.06	15.72	90.82
A1709-11	Tatie	2.64	0	0	67.21	0.03	0.06	0.75	0.04	2.98	3.62	0.04	0.06	13.82	91.25
A1709-12	Tatie	4.37	0	0.01	62.73	0.13	0.67	1.30	0.03	1.61	1.37	0	0.03	14.86	87.12
A1709-13	Tatie	5.32	0	0	64.92	0.06	0.03	0.66	0.02	1.70	4.89	0.03	0.04	16.13	93.8
A1709-14	Tatie	3.43	0	0	65.4	0.06	0.03	0.65	0.02	1.69	4.81	0.03	0.04	14.03	90.19
A1709-15	Tatie	5.32	0.01	0.02	61.05	0.19	0.29	0.39	0.03	0.98	4.26	0	0	15.37	87.91
A1709-16	Tatie	5.36	0.04	0.04	62.73	0.14	0.42	0.83	0.11	0.88	3.97	0	0.03	15.79	90.35
A1709-17	Tatie	0.97	0.25	0.01	60.59	0.17	0.44	14.50	0.01	2.25	0.81	0.13	0.08	14.88	95.1
A1709-18	Tatie	0.6	0.13	0.05	80.77	0.06	0.54	2.36	0	2.23	2.29	0.18	0.00	13.65	102.86
A1709-19	Tatie	1.54	0.23	0	71.71	0.42	0.42	8.69	0.10	1.75	1.16	0.07	0.07	15.45	101.64
A1709-20	Tatie	1.47	0.18	0	74.67	0.09	0.17	1.96	0	1.47	4.72	0.06	0.03	13.5	98.32
A1709-21	Tatie	4.85	0.15	0	63.5	0.2	2.05	2.39	0.02	1.76	0.24	0	0.01	16.33	91.52
A1709-22	Tatie	3.84	0.01	0	70.4	0.09	0.05	2.16	0.01	1.64	3.57	0	0.03	15.51	97.31
A1709-23	Tatie	6.14	0	0	68.27	0.06	0.05	0.54	0.06	3.03	0.95	0.00	0.09	17.73	96.92
A1709-24	Tatie	4.19	0.03	0.05	69.28	0.10	0.14	0.74	0.01	1.84	4.71	0.01	0.07	15.58	96.75
AVG		3.33	0.05	3.72	64.86	0.10	0.28	1.81	0.03	1.76	2.92	0.04	0.06	14.72	93.68
STDEV		1.78	0.08	18.17	15.22	0.09	0.43	3.20	0.03	0.83	1.93	0.04	0.10	1.373	5.006

Table F.1 Chemical composition data of carbonates specifically: calcite and iron-rich magnesite from the Tatie (A1709) Claim, Beaverlodge Lake, NT, Canada
*concentrations reported as wt.%

Sample	Sample	Ca	Mg	Fe	Mn	Sr	C	O	Total
A1709-1	Tatie	0.28	20.66	10.78	0.81	0.02	13.6	53.28	99.42
A1709-2	Tatie	0.27	18.84	13.96	1.23	0	11.14	46.54	91.98
A1709-3	Tatie	0.26	17.93	14.11	1.23	0	12.93	50.74	97.19
A1709-4	Tatie	0.16	22.43	8.82	0.74	0.02	11.79	48.98	92.93
A1709-5	Tatie	0.28	18.98	13.66	1.39	0	12.68	50.72	97.72
A1709-6	Tatie	0.40	20.23	10.5	1.46	0	13.25	52.21	98.06
A1709-7	Tatie	0.33	19.09	14.1	1.37	0	12.24	49.72	96.84
A1709-8	Tatie	0.32	16.54	16.9	1.57	0	13.25	51.62	100.2
A1709-9	Tatie	0.29	16.13	17.66	1.82	0	11.7	47.49	95.08
A1709-10	Tatie	0.07	20.33	12.5	0.80	0.03	13.28	52.61	99.62
A1709-11	Tatie	0.17	19.92	11.92	0.72	0	14.35	55.04	102.13
A1709-12	Tatie	0.05	20.65	12.12	0.84	0.02	12.98	51.93	98.6
A1709-13	Tatie	0.28	20.51	8.77	1.95	0	14.08	54.2	99.79
A1709-14	Tatie	0.18	20.56	9.26	0.77	0.01	13.42	52.23	96.44
A1709-15	Tatie	0.27	18.42	12.89	1.12	0	13.36	51.84	97.9
AVG		0.24	19.41	12.53	1.19	0.01	12.94	51.28	97.59
STDEV		0.10	1.68	2.67	0.40	0.01	0.89	2.33	2.71

Sample	Sample	Ca	Mg	Fe	Mn	Sr	C	O	Total
A1709-1	Tatie	32.84	0.97	2.65	6.24	0	11.31	46.45	100.47
A1709-2	Tatie	33.13	1.63	2.87	6.34	0	11.67	48.05	103.69
A1709-3	Tatie	33.04	0.82	3.02	6.77	0	10.98	45.83	100.46
A1709-4	Tatie	33.19	0.77	2.93	6.12	0	10.38	44.03	97.43
A1709-5	Tatie	31.74	1.08	3.53	6.36	0.02	10.95	45.41	99.09
A1709-6	Tatie	32.35	1.02	2.62	6.53	0	11.49	46.86	100.87
A1709-7	Tatie	32.28	0.92	3.43	6.41	0	10.77	45.03	98.85
A1709-8	Tatie	32.7	1.22	2.76	6.24	0.01	10.89	45.46	99.27
A1709-9	Tatie	32.29	1.12	3.59	7.09	0	11.68	47.85	103.63
A1709-10	Tatie	32.44	0.66	3.4	5.87	0	12.81	50.19	105.37
AVG		32.60	1.02	3.08	6.40	0.00	11.29	46.52	100.91
STDEV		0.46	0.27	0.37	0.34	0.01	0.68	1.79	2.53

Table G.1 U and Pb isotopic values for uranium oxides from the Bee (A1090) and Tatie (A1709) Claims, Beaverlodge Lake, NT, Canada measured by Secondary Ion Mass Spectrometry.

Samples	$^{207}Pb/^{206}Pb$	"True" $^{207}Pb/^{206}Pb$	% Error	$^{207}Pb/^{235}U$	"True" $^{207}Pb/^{235}U$	% Error	$^{206}Pb/^{238}U$	"True" $^{206}Pb/^{238}U$	% Error
02-05U-A1090-1	6.26E-02	0.0598764	1.30	2.70E+00	0.2801081	2.20	3.16E-01	0.0314376	2.20
02-05U-A1090-2	5.97E-02	0.0571600	0.78	2.13E+00	0.2215301	4.00	3.03E-01	0.0301524	0.40
02-05U-A1090-3	5.66E-02	0.0541649	0.46	2.62E+00	0.2722096	2.80	3.59E-01	0.0357083	3.50
02-05U-A1090-4	5.59E-02	0.0535184	0.90	2.93E+00	0.3045580	3.10	3.92E-01	0.0390078	3.90
02-05U-A1090-5	5.68E-02	0.0543445	1.00	2.85E+00	0.2959903	2.80	3.82E-01	0.0379778	4.00
02-05U-A1090-6	5.76E-02	0.0550956	1.30	2.48E+00	0.2570668	0.90	3.33E-01	0.0331616	1.10
02-05U-A1090-7	5.64E-02	0.0540310	0.46	2.13E+00	0.2205671	0.70	2.96E-01	0.0294103	0.93
02-05U-A1090-8	5.99E-02	0.0573357	1.10	1.98E+00	0.2053762	0.46	2.51E-01	0.0250122	1.20
02-05U-A1090-9	5.96E-02	0.0570175	0.77	1.43E+00	0.1480884	2.30	1.84E-01	0.0182978	1.20
02-05U-A1090-10	5.80E-02	0.0554880	0.83	2.40E+00	0.2494698	0.90	3.11E-01	0.0308937	2.90
02-06U-A1090-1	6.07E-02	0.0602245	0.60	2.65E+00	0.2661264	2.60	3.32E-01	0.0319166	1.10
02-06U-A1090-2	5.89E-02	0.0584337	0.99	1.91E+00	0.1915064	3.70	2.52E-01	0.0242419	2.10
02-06U-A1090-3	5.86E-02	0.0580739	0.75	2.35E+00	0.2359581	0.42	3.05E-01	0.0292722	2.33
02-06U-A1090-4	5.98E-02	0.0592676	0.70	2.15E+00	0.2160725	2.93	2.75E-01	0.0264364	0.80
02-06U-A1090-5	5.72E-02	0.0567612	0.95	2.53E+00	0.2542941	3.40	3.37E-01	0.0323801	4.00
02-06U-A1090-6	5.86E-02	0.0581233	0.77	1.93E+00	0.1939626	2.33	2.53E-01	0.0243356	3.00
02-06U-A1090-7	6.02E-02	0.0597064	1.19	1.64E+00	0.1650697	1.15	2.08E-01	0.0199424	0.42
02-06U-A1090-8	6.01E-02	0.0596049	1.01	2.09E+00	0.2102352	1.05	2.59E-01	0.0249283	1.20

Samples	$^{207}Pb/^{206}Pb$	"True" $^{207}Pb/^{206}Pb$	% Error	$^{207}Pb/^{235}U$	"True" $^{207}Pb/^{235}U$	% Error	$^{206}Pb/^{238}U$	"True" $^{206}Pb/^{238}U$	% Error
02-06U-A1709-1	8.60E-02	0.0853148	0.20	1.79E+01	1.7926784	0.40	1.58E+00	0.1515322	0.40
02-06U-A1709-2	8.68E-02	0.0860737	0.30	1.27E+01	1.2743757	0.86	1.10E+00	0.1060935	0.80
02-06U-A1709-3	8.80E-02	0.0872239	0.20	2.08E+01	2.0858255	1.80	1.79E+00	0.1723711	2.50
02-06U-A1709-4	8.87E-02	0.0879064	0.25	2.11E+01	2.1160092	1.20	1.80E+00	0.1732194	1.30
02-06U-A1709-5	8.90E-02	0.0882871	0.10	2.41E+01	2.4142173	0.60	2.08E+00	0.2001108	0.86
02-06U-A1709-6	8.76E-02	0.0868566	0.25	2.15E+01	2.1534514	1.30	1.89E+00	0.1813244	1.25
02-06U-A1709-7	8.93E-02	0.0885767	0.10	2.31E+01	2.3139644	1.40	1.99E+00	0.1910537	2.80
02-06U-A1709-8	8.90E-02	0.0882117	0.05	2.28E+01	2.2907559	1.48	1.96E+00	0.1881563	1.60
02-06U-A1709-9	8.81E-02	0.0873460	0.17	2.06E+01	2.0715938	1.60	1.78E+00	0.1712487	1.40
02-06U-A1709-10	8.92E-02	0.0884109	0.11	2.43E+01	2.4344215	2.30	2.031494	0.1951872	2.96
02-06U-A1709-11	8.90E-02	0.0882105	0.50	2.03E+01	2.0342591	3.90	1.735245	0.1667234	3.90
02-06U-A1709-12	8.79E-02	0.0871556	0.12	1.77E+01	1.7810004	2.40	1.54E+00	0.1478101	3.60
02-06U-A1709-13	8.79E-02	0.0871488	0.20	2.05E+01	2.0616945	2.80	1.77E+00	0.1704664	2.80
02-06U-A1709-14	8.67E-02	0.0859485	0.20	1.40E+01	1.4080727	1.44	1.23E+00	0.1177970	0.70

Table H.1 REE contents for uranium oxides from the Bee (A1090) and Tatie (A1709) Claims, Beaverlodge Lake, NT, Canada measured by Laser Ablation Inductively Coupled Mass Spectrometry. Rare earth elements normalized to C1 chondrites from Sun and McDonough, 1989

Sample #	La	Ce	Pr	Nd	Sm	Eu	Gd	Tb	Dy	Ho	Er	Tm	Yb	Lu
A1709-4	23.62	569.77	231.06	1649.19	1573.65	359.04	2680.14	517.93	2694.88	398.74	945.91	130.50	856.31	106.29
A1709-5	23.74	572.74	239.85	1690.86	1626.29	366.77	2736.30	528.41	2771.38	408.11	978.20	134.19	870.06	107.39
A1709-6	20.89	564.68	237.92	1688.56	1589.57	365.80	2659.10	509.64	2692.09	394.38	935.89	131.30	856.84	106.33
A1709-7	22.77	564.70	236.09	1675.14	1576.91	368.38	2686.17	537.98	2740.21	407.13	971.10	134.37	874.64	107.45
A1709-8	23.25	549.65	230.06	1634.92	1568.44	352.99	2668.86	513.77	2714.79	398.13	970.10	132.30	849.31	106.40
A1709-9	20.53	554.54	231.87	1653.43	1565.42	356.79	2677.45	514.57	2692.11	392.76	932.37	129.79	824.87	102.46
A1090-1	313.22	4166.43	833.00	4504.66	1517.27	235.72	1426.73	217.72	1295.23	235.72	594.41	69.40	367.14	54.16
A1090-2	321.28	4147.17	835.71	4582.14	1561.04	243.62	1482.65	230.26	1343.73	243.46	621.73	71.66	378.71	54.96
A1090-3	332.69	4231.20	853.16	4664.14	1595.64	248.93	1507.86	236.17	1377.05	254.21	635.30	72.86	390.47	57.71
A1090-4	520.31	4474.19	854.34	4629.85	1581.53	246.65	1427.59	229.39	1336.55	242.95	619.41	73.37	389.01	59.26
A1090-5	325.78	4426.01	914.14	5022.28	1721.05	268.40	1555.16	240.77	1401.14	255.17	629.76	74.91	394.89	55.20
A1090-6	340.20	4512.48	916.81	5001.87	1695.78	261.09	1506.98	232.85	1346.32	246.69	608.29	72.71	387.97	54.00
A1090-7	350.16	3998.83	798.48	4371.32	1474.95	231.87	1348.99	213.83	1254.04	228.80	584.10	69.72	377.87	55.08
A1090-8	366.53	3949.61	769.77	4190.19	1433.37	221.38	1256.72	204.65	1200.77	220.55	569.59	68.34	368.58	53.86
A1090-9	468.89	4289.79	807.75	4267.86	1374.09	217.39	1168.13	192.06	1136.89	201.96	520.90	64.51	352.09	49.54
A1090-10	381.23	3912.85	764.35	4075.69	1329.68	207.78	1143.83	183.69	1091.95	195.30	494.65	60.48	329.75	47.61
A1090-11	304.40	4390.71	884.31	4946.95	1696.13	261.15	1540.89	238.67	1382.65	250.46	621.82	73.10	382.74	54.02
A1090-12	431.20	4206.20	776.39	3905.04	1233.23	191.53	963.99	161.66	943.85	166.79	429.67	54.21	293.53	41.11
A1090-13	264.12	4133.04	854.60	4741.01	1641.56	251.38	1506.60	232.38	1338.62	243.46	614.38	72.84	379.26	53.39
A1090-14	297.13	4276.08	871.95	4840.17	1671.09	256.02	1541.15	236.96	1369.13	249.34	627.15	73.88	382.55	55.59
A1090-15	381.86	4014.22	790.05	4193.80	1423.19	219.75	1233.35	203.14	1186.03	215.36	540.79	66.77	356.45	52.13

Sample #	La$_N$	Ce$_N$	Pr$_N$	Nd$_N$	Sm$_N$	Eu$_N$	Gd$_N$	Tb$_N$	Dy$_N$	Ho$_N$	Er$_N$	Tm$_N$	Yb$_N$	Lu$_N$
A1709-4	99.66	931.00	2432.26	3531.45	10285.30	6190.43	13042.05	13848.52	10609.76	7044.84	5715.48	5117.48	5037.10	4184.52
A1709-5	100.16	935.85	2524.71	3620.69	10629.37	6323.57	13315.34	14128.56	10910.93	7210.44	5910.55	5262.35	5118.02	4227.84
A1709-6	88.13	922.68	2504.44	3615.77	10389.33	6306.97	12939.64	13626.80	10598.78	6967.77	5654.93	5149.07	5040.23	4186.07
A1709-7	96.09	922.72	2485.21	3587.03	10306.62	6351.35	13071.41	14384.43	10788.24	7193.08	5867.69	5269.28	5144.95	4230.17
A1709-8	98.08	898.12	2421.71	3500.90	10251.26	6086.08	12987.17	13737.14	10688.13	7034.08	5861.64	5188.37	4995.95	4189.16
A1709-9	86.64	906.12	2440.74	3540.53	10231.49	6151.47	13028.95	13758.68	10598.85	6939.30	5633.67	5089.74	4852.16	4033.67
A1090-1	1321.61	6807.89	8768.45	9645.96	9916.83	4064.16	6942.71	5821.44	5099.33	4164.69	3591.62	2721.72	2159.65	2132.10
A1090-2	1355.60	6776.42	8796.99	9811.87	10202.85	4200.36	7214.85	6156.65	5290.26	4301.48	3756.65	2810.34	2227.73	2163.82
A1090-3	1403.77	6913.72	8980.67	9987.46	10429.01	4291.83	7337.53	6314.80	5421.47	4491.38	3838.70	2857.34	2296.85	2272.13
A1090-4	2195.41	7310.76	8993.08	9914.04	10336.80	4252.53	6946.92	6133.53	5262.02	4292.45	3742.64	2877.38	2288.30	2333.24
A1090-5	1374.59	7232.03	9622.50	10754.36	11248.66	4627.58	7567.69	6437.74	5516.31	4508.39	3805.21	2937.48	2322.86	2173.10
A1090-6	1435.44	7373.34	9650.63	10710.64	11083.50	4501.54	7333.23	6226.00	5300.47	4358.41	3675.44	2851.18	2282.17	2125.91
A1090-7	1477.48	6534.04	8405.03	9360.43	9640.19	3997.76	6564.44	5717.41	4937.18	4042.48	3529.28	2734.05	2222.76	2168.46
A1090-8	1546.55	6453.61	8102.83	8972.56	9368.43	3816.84	6115.41	5472.05	4727.45	3896.67	3441.66	2680.11	2168.09	2120.50
A1090-9	1978.43	7009.46	8502.66	9138.89	8980.95	3748.07	5684.35	5135.27	4475.95	3568.25	3147.44	2529.84	2071.11	1950.30
A1090-10	1608.56	6393.54	8045.74	8727.38	8690.69	3582.40	5566.07	4911.45	4299.02	3450.55	2988.82	2371.87	1939.69	1874.49
A1090-11	1284.38	7174.37	9308.52	10593.03	11085.81	4502.56	7498.27	6381.52	5443.51	4425.07	3757.25	2866.59	2251.43	2126.69
A1090-12	1819.41	6872.88	8172.54	8361.98	8060.35	3302.22	4690.95	4322.47	3715.94	2946.81	2596.17	2126.05	1726.66	1618.42
A1090-13	1114.41	6753.34	8995.77	10152.07	10729.16	4334.18	7331.41	6213.39	5270.15	4301.48	3712.25	2856.57	2230.97	2101.93
A1090-14	1253.70	6987.05	9178.41	10364.39	10922.19	4414.14	7499.51	6335.81	5390.29	4405.28	3789.42	2897.41	2250.27	2188.58
A1090-15	1611.22	6559.18	8316.29	8980.30	9301.90	3788.72	6001.71	5431.60	4669.43	3805.02	3267.60	2618.46	2096.77	2052.42

Sample #	$\Sigma LREE_N$[1]	$\Sigma HREE_N$[2]	$\Sigma LREE_N/\Sigma HREE_N$	La_N/Yb_N	La_N/Sm_N	Dy_N/Yb_N	Eu/Eu*[3]
A1709-4	23470.09	64599.76	0.36	0.02	0.01	2.11	0.53
A1709-5	24134.35	66084.03	0.37	0.02	0.01	2.13	0.53
A1709-6	23827.33	64163.28	0.37	0.02	0.01	2.10	0.54
A1709-7	23749.02	65949.24	0.36	0.02	0.01	2.10	0.55
A1709-8	23256.15	64681.63	0.36	0.02	0.01	2.14	0.53
A1709-9	23356.98	63935.02	0.37	0.02	0.01	2.18	0.53
A1090-1	40524.90	32633.26	1.24	0.61	0.13	2.36	0.49
A1090-2	41144.09	33921.77	1.21	0.61	0.13	2.37	0.49
A1090-3	42006.46	34830.19	1.21	0.61	0.13	2.36	0.49
A1090-4	43002.62	33876.49	1.27	0.96	0.21	2.30	0.50
A1090-5	44859.72	35268.79	1.27	0.59	0.12	2.37	0.50
A1090-6	44755.10	34152.82	1.31	0.63	0.13	2.32	0.50
A1090-7	39414.93	31916.07	1.23	0.66	0.15	2.22	0.50
A1090-8	38260.82	30621.93	1.25	0.71	0.17	2.18	0.50
A1090-9	39358.46	28562.50	1.38	0.96	0.22	2.16	0.52
A1090-10	37048.32	27401.95	1.35	0.83	0.19	2.22	0.52
A1090-11	43948.67	34750.32	1.26	0.57	0.12	2.42	0.49
A1090-12	36589.37	23743.47	1.54	1.05	0.23	2.15	0.54
A1090-13	42078.92	34018.14	1.24	0.50	0.10	2.36	0.49
A1090-14	43119.88	34756.57	1.24	0.56	0.11	2.40	0.49
A1090-15	38557.62	29943.00	1.29	0.77	0.17	2.23	0.51

[1] $\sum LREE_N = La_N$ to Eu_N
[2] $\sum HREE_N = Gd_N$ to Lu_N
[3] $Eu/Eu* = Eu_N / (Sm_N \times Gd_N)^{0.5}$

Table I.1 Whole-Rock, Major-, Trace-, and Rare Earth Geochemical Analyses from the Zebulon Formation specifically strongly altered basalts and rhyolites. Samples were collected during the summer of 2012.

Sample Number	Lithology	SiO_2	Al_2O_3	$Fe_2O_3(T)$	MnO	MgO	CaO	Na_2O	K_2O	TiO_2
Unit Symbol		%	%	%	%	%	%	%	%	%
Detection Limit		0.01	0.01	0.01	0.001	0.01	0.01	0.01	0.01	0.001
Analysis Method		FUS-ICP	FUS-ICP	FUS-ICP	FUS-ICP	FUS-ICP	FUS-ICP	FUS-ICP	FUS-ICP	FUS-ICP
12PS 2	Zebulon Basalt	49.29	16.39	13.09	0.096	11.9	0.15	1.03	1.7	0.751
12PS 3A	Zebulon Basalt	58.08	11.87	15.66	0.073	6.64	0.29	1.05	1.82	0.818
12PS 3B	Zebulon Basalt	50.32	16.3	15.37	0.054	7.35	0.39	2.12	2.45	1.283
12PS 3C	Zebulon Basalt	46.08	23.41	15.8	0.012	1.49	0.04	0.16	8.69	1.209
12PS 5	Zebulon Rhyolite	78.38	9.75	4.61	0.01	0.32	0.03	0.09	6.07	0.139
12PS 6	Zebulon Rhyolite	83.6	8.15	3.31	0.009	0.32	0.02	0.06	4.36	0.118
12PS 7	Zebulon Rhyolite	85.1	6.94	3.8	0.012	0.24	0.02	0.07	3.74	0.142
12PS 8A	Zebulon Rhyolite	80.5	9.51	2.67	0.017	0.33	0.03	0.08	5.75	0.19
12PS 8B	Zebulon Rhyolite	84.15	7.52	2.7	0.017	0.37	0.04	0.07	4.38	0.106
12PS 9	Zebulon Rhyolite	81.52	9.61	2.19	0.008	0.26	0.06	0.09	5.41	0.068
12PS 10	Zebulon Rhyolite	67.61	13.54	6.04	0.007	0.06	0.06	0.17	11.54	0.431
12PS 11	Zebulon Rhyolite	79.63	10.43	2.34	0.023	0.42	0.02	0.08	5.34	0.135

Sample Number	Lithology	P$_2$O$_5$	LOI	Total	Sc	Be	V	Ba	Sr	Y	Zr
Unit Symbol		%	%	%	ppm	ppm	ppm	ppm	ppm	ppm	ppm
Detection Limit		0.01		0.01	1	1	5	3	2	2	4
Analysis Method		FUS-ICP	FUS-ICP	FUS-ICP	FUS-ICP	FUS-ICP	FUS-ICP	FUS-ICP	FUS-ICP	FUS-ICP	FUS-ICP
12PS 2	Zebulon Basalt	0.08	6.43	100.9	21	14	138	54	4	17	66
12PS 3A	Zebulon Basalt	0.19	3.92	100.4	19	3	152	175	7	29	80
12PS 3B	Zebulon Basalt	0.28	4.67	100.6	29	6	223	313	17	26	118
12PS 3C	Zebulon Basalt	0.02	3.59	100.5	50	9	254	242	6	25	157
12PS 5	Zebulon Rhyolite	0.01	0.89	100.3	4	2	< 5	564	14	24	189
12PS 6	Zebulon Rhyolite	0.01	0.9	100.9	4	2	< 5	301	7	26	161
12PS 7	Zebulon Rhyolite	0.03	0.76	100.9	4	2	< 5	302	8	20	181
12PS 8A	Zebulon Rhyolite	0.01	0.91	100	7	2	5	462	15	29	252
12PS 8B	Zebulon Rhyolite	0.03	0.84	100.2	4	2	5	322	10	23	141
12PS 9	Zebulon Rhyolite	0.05	0.97	100.2	3	2	11	331	12	28	224
12PS 10	Zebulon Rhyolite	0.04	0.3	99.8	9	1	9	1141	18	22	385
12PS 11	Zebulon Rhyolite	0.02	1.21	99.65	5	2	6	411	12	29	178

Sample Number	Lithology	Cr	Co	Ni	Cu	Zn	Ga	Ge	As	Rb	Nb
Unit Symbol		ppm	ppm	ppm	ppm	ppm	ppm	ppm	ppm	ppm	ppm
Detection Limit		20	1	20	10	30	1	1	5	2	1
Analysis Method		FUS-MS	FUS-MS	FUS-MS	FUS-MS	FUS-MS	FUS-MS	FUS-MS	FUS-MS	FUS-MS	FUS-MS
12PS 2	Zebulon Basalt	80	55	120	< 10	120	18	2	< 5	25	3
12PS 3A	Zebulon Basalt	< 20	36	50	< 10	100	14	2	< 5	42	4
12PS 3B	Zebulon Basalt	< 20	35	50	< 10	60	19	2	< 5	61	6
12PS 3C	Zebulon Basalt	100	7	< 20	< 10	< 30	27	2	< 5	334	7
12PS 5	Zebulon Rhyolite	< 20	24	< 20	< 10	< 30	12	2	< 5	240	7
12PS 6	Zebulon Rhyolite	< 20	22	< 20	< 10	< 30	13	3	< 5	191	8
12PS 7	Zebulon Rhyolite	< 20	22	< 20	< 10	< 30	10	3	< 5	170	7
12PS 8A	Zebulon Rhyolite	< 20	16	< 20	< 10	< 30	14	2	< 5	228	10
12PS 8B	Zebulon Rhyolite	< 20	24	< 20	< 10	< 30	11	3	< 5	175	6
12PS 9	Zebulon Rhyolite	< 20	17	< 20	< 10	< 30	14	3	< 5	197	24
12PS 10	Zebulon Rhyolite	< 20	35	< 20	< 10	< 30	10	2	< 5	261	16
12PS 11	Zebulon Rhyolite	< 20	25	< 20	< 10	40	17	3	< 5	223	9

Sample Number	Lithology	Mo	Ag	In	Sn	Sb	Cs	La	Ce	Pr	Nd
Unit Symbol		ppm	ppm	ppm	ppm	ppm	ppm	ppm	ppm	ppm	ppm
Detection Limit		2	0.5	0.2	1	0.5	0.5	0.1	0.1	0.05	0.1
Analysis Method		FUS-MS	FUS-MS	FUS-MS	FUS-MS	FUS-MS	FUS-MS	FUS-MS	FUS-MS	FUS-MS	FUS-MS
12PS 2	Zebulon Basalt	< 2	< 0.5	< 0.2	< 1	< 0.5	1.1	14.7	31.6	3.56	14.3
12PS 3A	Zebulon Basalt	< 2	0.5	< 0.2	1	0.6	< 0.5	12.1	29.8	3.78	17.8
12PS 3B	Zebulon Basalt	< 2	0.7	< 0.2	< 1	0.7	1.3	19.6	44.7	5.55	24.5
12PS 3C	Zebulon Basalt	< 2	1.1	< 0.2	1	0.8	4.6	2.4	6.1	0.78	4.2
12PS 5	Zebulon Rhyolite	< 2	1	< 0.2	1	2.9	7.5	22.7	50.1	5.31	20.4
12PS 6	Zebulon Rhyolite	< 2	0.9	< 0.2	2	2.6	5.7	35	76.2	8.1	31
12PS 7	Zebulon Rhyolite	< 2	1	< 0.2	1	4.5	4.8	27.6	59	6.44	24.3
12PS 8A	Zebulon Rhyolite	< 2	1.7	< 0.2	2	0.9	5.8	41.3	90.6	9.49	36.5
12PS 8B	Zebulon Rhyolite	< 2	0.7	< 0.2	1	0.8	3.7	57.3	127	13.2	49.8
12PS 9	Zebulon Rhyolite	3	1.3	< 0.2	5	1.2	5	14.8	38.4	4.59	18.2
12PS 10	Zebulon Rhyolite	< 2	2.5	< 0.2	2	2.4	3	14.4	26	2.73	10.1
12PS 11	Zebulon Rhyolite	< 2	0.9	< 0.2	2	< 0.5	3.9	39.6	94.4	9.91	37.4

Sample Number	Lithology	Sm	Eu	Gd	Tb	Dy	Ho	Er	Tm	Yb	Lu
Unit Symbol		ppm	ppm	ppm	ppm	ppm	ppm	ppm	ppm	ppm	ppm
Detection Limit		0.1	0.05	0.1	0.1	0.1	0.1	0.1	0.05	0.1	0.04
Analysis Method		FUS-MS	FUS-MS	FUS-MS	FUS-MS	FUS-MS	FUS-MS	FUS-MS	FUS-MS	FUS-MS	FUS-MS
12PS 2	Zebulon Basalt	3.2	0.93	3.3	0.5	3.2	0.6	1.8	0.27	1.8	0.27
12PS 3A	Zebulon Basalt	5.3	1.89	6.1	1	5.9	1.1	3	0.4	2.4	0.35
12PS 3B	Zebulon Basalt	5.3	1.74	5.3	0.9	4.8	1	2.7	0.39	2.5	0.4
12PS 3C	Zebulon Basalt	2.1	0.43	3.5	0.7	4.5	0.9	2.8	0.43	3	0.5
12PS 5	Zebulon Rhyolite	4.1	0.78	3.6	0.6	3.7	0.8	2.5	0.4	2.8	0.45
12PS 6	Zebulon Rhyolite	6.4	1.09	5.2	0.8	4.6	0.9	2.8	0.43	2.8	0.43
12PS 7	Zebulon Rhyolite	4.3	0.82	3.5	0.5	3.1	0.7	2	0.3	2.1	0.33
12PS 8A	Zebulon Rhyolite	7.5	1.23	5.6	0.8	4.9	1	3.2	0.5	3.3	0.54
12PS 8B	Zebulon Rhyolite	9.4	1.2	7.1	0.8	4.2	0.8	2.5	0.4	2.7	0.44
12PS 9	Zebulon Rhyolite	3.8	0.56	4.2	0.9	5.6	1.2	3.6	0.58	3.9	0.63
12PS 10	Zebulon Rhyolite	2.2	0.5	2.5	0.5	3.5	0.8	2.5	0.4	2.8	0.47
12PS 11	Zebulon Rhyolite	8	1.09	6.2	0.9	5.1	1	3.2	0.48	3.2	0.51

Sample Number	Lithology	Hf	Ta	W	Tl	Pb	Bi	Th	U
Unit Symbol		ppm	ppm	ppm	ppm	ppm	ppm	ppm	ppm
Detection Limit		0.2	0.1	1	0.1	5	0.4	0.1	0.1
Analysis Method		FUS-MS	FUS-MS	FUS-MS	FUS-MS	FUS-MS	FUS-MS	FUS-MS	FUS-MS
12PS 2	Zebulon Basalt	1.5	0.2	52	< 0.1	< 5	1.4	2.3	1.8
12PS 3A	Zebulon Basalt	2	0.3	105	0.2	6	< 0.4	1.4	0.8
12PS 3B	Zebulon Basalt	2.5	0.3	40	0.2	< 5	< 0.4	1.5	0.6
12PS 3C	Zebulon Basalt	3.6	0.4	26	0.7	8	0.6	3	4
12PS 5	Zebulon Rhyolite	4.2	0.9	311	1.5	7	< 0.4	6.8	2.9
12PS 6	Zebulon Rhyolite	3.8	0.8	261	1	< 5	< 0.4	6.4	2.4
12PS 7	Zebulon Rhyolite	3.8	0.8	346	1	7	< 0.4	5	2.4
12PS 8A	Zebulon Rhyolite	5.3	0.9	235	1.1	< 5	0.5	7.1	2.4
12PS 8B	Zebulon Rhyolite	3.2	0.9	361	0.9	< 5	0.6	5.6	2.7
12PS 9	Zebulon Rhyolite	7.9	2.6	243	0.8	7	< 0.4	19	5.3
12PS 10	Zebulon Rhyolite	8.2	1.4	370	1.2	9	< 0.4	10.5	3.2
12PS 11	Zebulon Rhyolite	4.3	1	281	1.1	< 5	< 0.4	7.7	3.2

Table I.2 Summary of Petrographic observations from altered basalt and rhyolite samples from the Zebulon Formation. Samples were collected during the summer of 2012.

Samples	Unit	Description
12ps2	Zebulon Basalt	• Amygdaloidal basalt filled with quartz • Chloritization of Mafic minerals • Few quartz veins
12ps3a	Zebulon Basalt	• Plagioclase microlites show felty texture • Amygdules filled with quartz and chlorite (?)
12sps3b	Zebulon Basalt	• Heavily altered basalt • Plagioclase microlites completely replaced with illite • Groundmass filled with hematite
12ps3c	Zebulon Basalt	• Heavily altered basalt • Plagioclase microlites replaced with illite • Abundant hematite in the groundmass • Quartz in the fractures • Hematite / Fe oxide replacing Fe-Mg minerals
12ps5	Zebulon Rhyolite	• Groundmass: Quartz, illite, and plagioclase • Phenocrysts of quartz, orthoclase and plagioclase • Fragmental rhyolite • Fragmental components are angular and contain abundant hematite
12ps6	Zebulon Rhyolite	• Groundmass: Quartz, illite, and plagioclase • Phenocrysts of quartz, orthoclase and plagioclase Fragmental rhyolite • Fragmental components are angular and contain abundant hematite
12ps7	Zebulon Rhyolite	• Groundmass 90% • Phenocrysts 10% • Groundmass: Quartz, illite, and plagioclase • Phenocrysts of quartz, orthoclase and plagioclase • Fragmental rhyolite • Fragmental components are angular and contain abundant hematite • Not as fragmental as previous samples examined
12ps8a	Zebulon Rhyolite	• Groundmass 80% • Phenocrysts 20% • Groundmass: Quartz, illite, and plagioclase • Phenocrysts of quartz, orthoclase and plagioclase Fragmental rhyolite • Fragmental components are angular and contain abundant hematite
12ps8b	Zebulon Rhyolite	• Groundmass 90% • Phenocrysts 10% • Groundmass: Quartz, illite, and plagioclase • Phenocrysts of quartz • Fragmental rhyolite • Fragmental components are angular and contain abundant hematite
12ps9	Zebulon Rhyolite	• Groundmass 80%

		- Phenocrysts 20% - Groundmass: Quartz, illite, and plagioclase - Phenocrysts of quartz, orthoclase and plagioclase - Fragmental rhyolite - Fragmental components are angular and contain abundant hematite
12ps10	Zebulon Rhyolite	- Groundmass 80% - Phenocrysts 20% - Groundmass: Quartz, illite, and plagioclase - Phenocrysts of quartz, orthoclase and plagioclase - Fragmental rhyolite - Fragmental components are angular and contain abundant hematite - Late veins of chlorite and hematite
12ps11	Zebulon Rhyolite	- Groundmass 90% - Phenocrysts 10% - Groundmass: Quartz, illite, and plagioclase - Phenocrysts of quartz and orthoclase - Fragmental rhyolite - Fragmental components are angular and contain abundant hematite
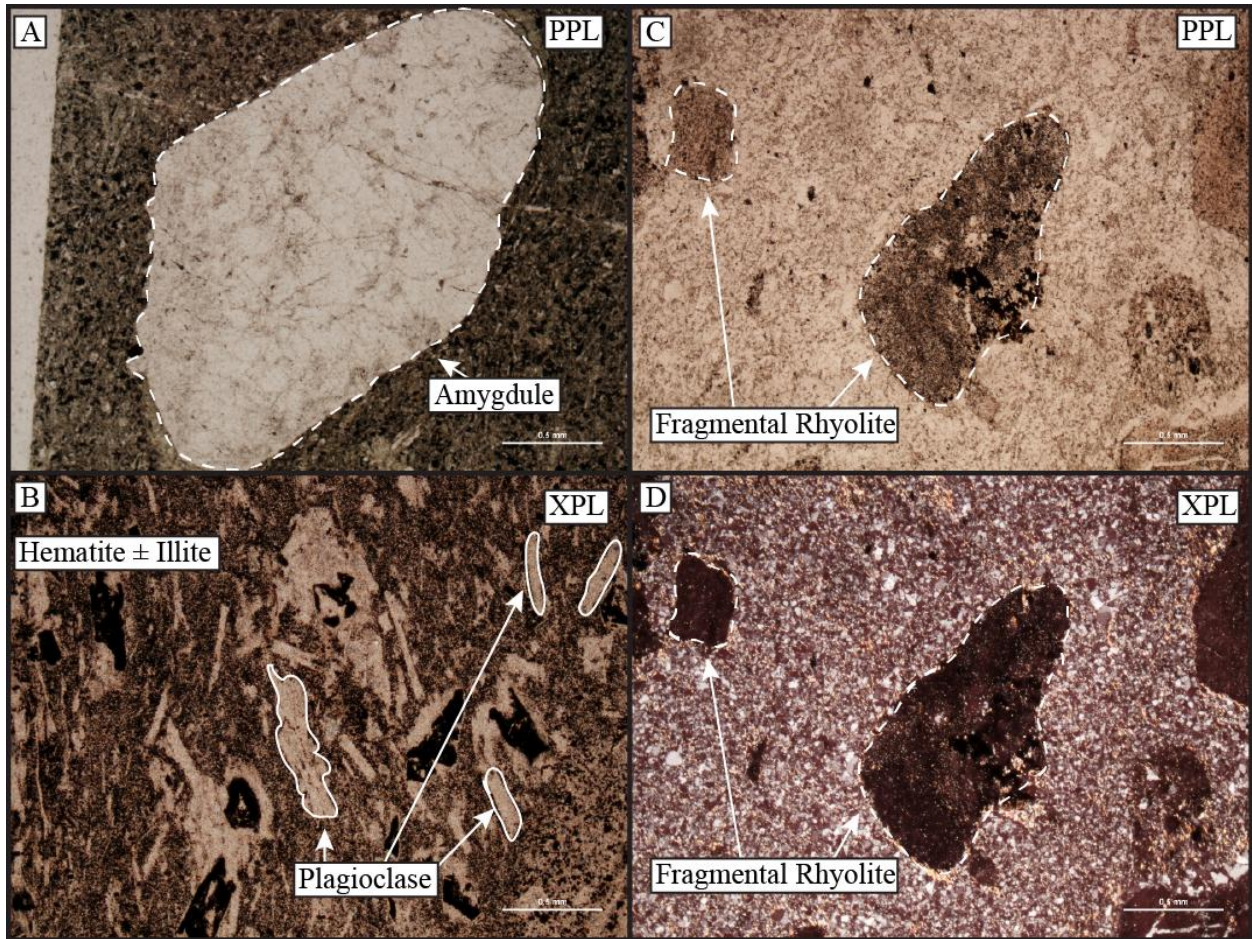
Figure I.2 Photomicrograph image of altered volcanic rock of the Zebulon Formation. (A) Amugdule from the Zebulon Formation basalt and consist of quartz. (B) Heavily altered basalt from the Zebulon Formation. The groundmass has been completely replaced by illite and hematite. Relict plagioclase laths are visible in the groundmass. (C) and (D) Fragmental rhyolite with heavily oxidized brecciated rhyolite.

APPENDIX J

Table J.1 Composition Data of Fe-Mg chlorites from altered porphyry samples

Pt#	SiO$_2$	TiO$_2$	Al$_2$O$_3$	Cr$_2$O$_3$	FeO	MgO	MnO	CaO	Na$_2$O	K$_2$O	Cl	Total
12	31.54	0.12	20.16	0.07	15.09	21.41	0.17	0.01	0.05	0.03	0.01	88.67
23	28.25	0.07	20.96	0.02	15.27	22.82	0.13	0.01	0.02	0.05	0.01	87.63
26	31.99	0.03	20.63	0.04	22.73	11.38	0.63	0.06	0.16	0.68	0.02	88.34
27	26.32	0.02	20.63	0	26.02	12.83	0.55	0.04	0.01	0.06	0.02	86.50
33	29.29	0.04	18.17	0.06	19.42	19.53	0.50	0	0.01	0.03	0	87.06
34	30.43	0.07	18.20	0	18.71	17.95	0.33	0.08	0.02	0.23	0.01	86.02
36	26.19	0.02	20.89	0	25.11	13.20	0.68	0	0	0.02	0.01	86.12
38	28.94	0.02	19.32	0	23.62	11.97	1.25	0.05	0.01	0.03	0.01	85.22
39	30.06	0.09	18.32	0.03	18.93	19.24	0.44	0	0	0.03	0	87.14
45	30.30	0.04	18.38	0.02	19.72	19.97	0.39	0.02	0	0.02	0.03	88.90
48	28.98	0.09	22.63	0.03	18.35	18.96	0.23	0.01	0.01	0.02	0.01	89.31
2	29.00	0.06	21.16	0.03	13.96	23.95	0.10	0.01	0.01	0	0.01	88.29
3	27.23	0.18	20.33	0.01	14.05	21.54	0.09	0.02	0.11	0.07	0.02	83.66
5	27.83	0.07	20.97	0	13.79	22.96	0.14	0.05	0.11	0.04	0.02	85.98
6	28.43	0.08	20.14	0.03	13.75	22.89	0.13	0.01	0.08	0.07	0.02	85.63
7	27.88	0.05	22.31	0	14.36	21.36	0.13	0.03	0.02	0.12	0.01	86.27
8	27.58	0.07	18.85	0.03	13.30	21.94	0.10	0.01	0	0.02	0.01	81.90
10	27.77	0.08	19.23	0.02	17.39	19.85	0.18	0.01	0	0	0.01	84.53
11	30.06	0.10	19.45	0	12.83	24.69	0.09	0	0	0.01	0	87.22
12	29.03	0.08	19.99	0.07	13.09	23.57	0.13	0.02	0	0	0.01	86.00
15	27.57	0.08	20.59	0.04	13.43	21.54	0.13	0.02	0	0.08	0	83.48
16	27.37	0.06	20.35	0	14.16	20.33	0.22	0.03	0.03	0.02	0.02	82.59
18	27.20	0.07	20.75	0	13.93	21.70	0.14	0	0.02	0.02	0.02	83.86
19	28.77	0.07	20.97	0.01	13.59	22.02	0.15	0.02	0	0.09	0	85.70
20	26.87	0.09	20.70	0.02	12.84	21.70	0.15	0.02	0	0.12	0.01	82.52
21	26.04	0.08	19.67	0	12.98	20.81	0.12	0	0	0.07	0.01	79.78
23	30.99	0.08	18.45	0.06	17.93	19.57	0.30	0.01	0	0.16	0.01	87.56
25	27.79	0.01	17.98	0	18.77	16.89	0.58	0	0.04	0.00	0.02	82.09
26	27.24	0.30	19.00	0	20.73	13.14	1.10	0.04	0.02	0.05	0	81.63
27	26.74	0.64	19.55	0.10	22.33	10.89	1.20	0.05	0	0.00	0	81.49
28	26.00	0.02	20.69	0.01	22.63	13.71	0.61	0.05	0.03	0.09	0.02	83.86
29	26.42	0.04	20.56	0.02	22.00	14.35	0.60	0.01	0	0.09	0.01	84.11
41	28.68	0.03	18.14	0	18.22	19.38	0.37	0	0	0.05	0.01	84.89
42	28.13	0.02	17.64	0	20.34	16.74	0.50	0.02	0	0.01	0.01	83.41

Pt#	Si	Al(IV)	Si+Al(IV) = 8	Al (VI)	Ti	Cr	Fe	Mg	Mn	Ca	Na	K	SUM = 12	T₁
12	6.14	1.86	8	2.77	0.02	0.01	2.46	6.22	0.03	0	0.02	0.01	11.53	235.80
23	5.62	2.38	8	2.54	0.01	0	2.54	6.77	0.02	0	0.01	0.01	11.92	290.09
26	6.50	1.50	8	3.45	0	0.01	3.87	3.45	0.11	0.01	0.06	0.18	11.14	215.68
27	5.64	2.36	8	2.86	0	0	4.67	4.10	0.10	0.01	0	0.02	11.76	307.29
33	6.00	2.00	8	2.39	0.01	0.01	3.33	5.97	0.09	0	0.01	0.01	11.80	256.40
34	6.26	1.74	8	2.67	0.01	0	3.22	5.51	0.06	0.02	0.01	0.06	11.56	229.68
36	5.61	2.39	8	2.89	0	0	4.50	4.22	0.12	0	0	0.01	11.75	309.15
38	6.19	1.81	8	3.07	0	0	4.23	3.82	0.23	0.01	0	0.01	11.37	248.32
39	6.12	1.88	8	2.51	0.01	0.01	3.22	5.84	0.08	0	0	0.01	11.67	243.97
45	6.07	1.93	8	2.41	0.01	0	3.30	5.96	0.07	0	0	0.01	11.76	249.21
48	5.72	2.28	8	2.98	0.01	0	3.03	5.57	0.04	0	0	0	11.64	286.27
2	5.68	2.32	8	2.56	0.01	0	2.29	6.99	0.02	0	0	0	11.87	282.46
3	5.66	2.34	8	2.63	0.03	0	2.44	6.67	0.02	0	0.05	0.02	11.86	286.31
5	5.61	2.39	8	2.59	0.01	0	2.32	6.90	0.02	0.01	0.04	0.01	11.92	290.03
6	5.75	2.25	8	2.55	0.01	0.01	2.32	6.90	0.02	0	0.03	0.02	11.86	275.43
7	5.60	2.40	8	2.88	0.01	0	2.41	6.40	0.02	0.01	0.01	0.03	11.77	292.56
8	5.83	2.17	8	2.52	0.01	0	2.35	6.91	0.02	0	0	0.01	11.82	267.30
10	5.80	2.20	8	2.54	0.01	0	3.04	6.18	0.03	0	0	0	11.81	275.29
11	5.92	2.08	8	2.43	0.01	0	2.11	7.24	0.01	0	0	0	11.82	255.64
12	5.81	2.19	8	2.53	0.01	0.01	2.19	7.04	0.02	0	0	0	11.81	267.43
15	5.71	2.29	8	2.73	0.01	0.01	2.33	6.65	0.02	0.01	0	0.02	11.77	280.12
16	5.75	2.25	8	2.79	0.01	0	2.49	6.37	0.04	0.01	0.01	0	11.73	277.09
18	5.63	2.37	8	2.69	0.01	0	2.41	6.69	0.02	0	0.01	0	11.84	289.15
19	5.79	2.21	8	2.76	0.01	0	2.29	6.61	0.03	0	0	0.02	11.72	271.33
20	5.62	2.38	8	2.73	0.01	0	2.25	6.77	0.03	0	0	0.03	11.83	288.48
21	5.65	2.35	8	2.68	0.01	0	2.36	6.73	0.02	0	0	0.02	11.83	286.12
23	6.23	1.77	8	2.60	0.01	0.01	3.01	5.86	0.05	0	0	0.04	11.59	230.97
25	6.04	1.96	8	2.65	0	0	3.41	5.47	0.11	0	0.02	0	11.66	254.09
26	6.03	1.97	8	2.99	0.05	0	3.84	4.34	0.21	0.01	0.01	0.01	11.45	261.62
27	5.99	2.01	8	3.14	0.11	0.02	4.18	3.63	0.23	0.01	0.00	0	11.32	271.25
28	5.66	2.34	8	2.97	0	0	4.12	4.45	0.11	0.01	0.01	0.03	11.70	301.80
29	5.71	2.29	8	2.94	0.01	0	3.97	4.62	0.11	0	0	0.03	11.68	295.49
41	5.99	2.01	8	2.46	0.01	0	3.18	6.04	0.07	0	0	0.01	11.77	256.18
42	6.06	1.94	8	2.55	0	0	3.67	5.38	0.09	0	0	0	11.69	253.33

Pt#	SiO$_2$	TiO$_2$	Al$_2$O$_3$	Cr$_2$O$_3$	FeO	MgO	MnO	CaO	Na$_2$O	K$_2$O	Cl	Total
43	28.23	0.07	17.12	0.03	17.72	18.33	0.38	0.04	0.01	0.05	0.01	81.99
44	26.96	0.03	20.04	0	22.11	13.83	0.66	0.01	0.01	0.01	0.01	83.66
45	27.71	0.10	17.20	0.05	18.74	18.37	0.33	0	0.02	0.08	0.02	82.63
47	29.63	0.06	18.09	0.03	17.87	19.49	0.38	0	0	0.12	0.02	85.69
48	26.94	0.05	19.59	0.04	25.23	11.66	0.86	0.04	0.01	0	0.02	84.44
49	28.24	0.06	20.15	0	13.78	22.09	0.16	0.05	0.01	0	0	84.54
1	26.43	0.05	18.72	0.06	23.10	13.34	0.65	0.03	0.04	0	0	82.43
2	27.80	0.06	17.72	0.03	19.99	17.98	0.59	0	0.02	0.02	0.01	84.21
3	28.04	0.24	18.12	0	21.28	15.46	0.75	0	0.01	0.06	0	83.95
6	28.92	0.36	19.14	0.03	19.75	16.33	0.57	0.03	0.01	0.11	0.01	85.26
8	30.71	0.35	17.91	0	19.46	16.19	0.50	0.02	0.04	0.10	0.01	85.28
9	30.18	0.15	17.83	0	18.06	15.82	0.40	0.07	0.05	0.12	0.01	82.69
11	28.47	0.05	17.51	0	19.59	18.40	0.66	0.02	0	0	0	84.70
12	28.69	0.05	17.89	0.01	19.99	17.21	0.57	0.09	0.02	0.02	0	84.53
13	28.83	0.10	17.97	0	19.80	17.11	0.41	0.04	0.01	0.07	0	84.34
14	28.55	0.10	17.44	0.05	18.67	16.51	0.40	0.07	0.04	0.05	0.02	81.90
15	27.50	0.05	17.57	0	19.06	16.77	0.72	0.05	0.02	0.02	0	81.77
1	28.49	0.05	17.45	0.03	19.75	18.20	0.46	0.03	0.01	0.01	0.01	84.47
2	28.13	0.13	17.08	0	18.99	17.82	0.40	0.01	0.01	0	0	82.58
3	28.16	0.11	17.52	0.10	20.33	17.06	0.38	0.03	0.02	0.03	0.01	83.76
1	26.37	0	18.52	0.01	23.20	11.80	0.85	0.01	0	0	0	80.75
2	29.30	0.03	19.09	0	16.46	19.74	0.19	0.05	0	0.05	0	84.91
3	29.95	0.08	18.73	0.01	15.95	19.94	0.19	0.06	0.03	0.09	0	85.02
4	29.62	0.00	18.66	0.02	16.77	20.07	0.23	0.04	0.02	0	0	85.43
5	29.94	0.04	19.35	0	16.32	20.00	0.17	0.04	0.02	0.08	0	85.95
6	26.18	0.01	20.63	0	22.32	14.21	0.78	0.02	0.02	0	0	84.16
7	26.46	0	20.70	0	20.57	14.50	0.87	0	0	0	0	83.10
8	29.41	0.05	18.86	0	15.34	19.59	0.24	0.01	0.01	0.05	0	83.58
9	24.83	0.09	19.39	0	24.63	13.68	0.69	0.04	0.04	0	0	83.39
10	26.57	0.02	20.56	0.01	22.03	14.34	0.47	0.01	0.01	0	0	84.03
AVG	28.25	0.09	19.25	0.02	18.44	17.98	0.43	0.03	0.02	0.06	0.01	84.57
STDEV	1.48	0.10	1.35	0.02	3.59	3.55	0.28	0.02	0.03	0.09	0.01	2.08

Pt#	Si	Al(IV)	Si+Al(IV) = 8	Al (VI)	Ti	Cr	Fe	Mg	Mn	Ca	Na	K	SUM = 12	T_1
43	6.11	1.89	8	2.47	0.01	0	3.21	5.91	0.07	0.01	0.01	0.01	11.70	244.66
44	5.85	2.15	8	2.97	0.01	0	4.01	4.47	0.12	0	0	0	11.59	281.22
45	5.99	2.01	8	2.38	0.02	0.01	3.39	5.92	0.06	0	0.01	0.02	11.81	257.69
47	6.11	1.89	8	2.51	0.01	0	3.08	5.99	0.07	0	0	0.03	11.70	243.43
48	5.90	2.10	8	2.95	0.01	0.01	4.62	3.81	0.16	0.01	0	0	11.57	281.51
49	5.78	2.22	8	2.64	0.01	0	2.36	6.74	0.03	0.01	0	0	11.78	272.73
1	5.88	2.12	8	2.78	0.01	0.01	4.30	4.42	0.12	0.01	0.02	0	11.66	279.64
2	5.94	2.06	8	2.40	0.01	0	3.57	5.72	0.11	0	0.01	0.01	11.83	265.14
3	6.04	1.96	8	2.64	0.04	0	3.83	4.96	0.14	0	0	0.02	11.63	258.11
6	6.06	1.94	8	2.78	0.06	0	3.46	5.10	0.10	0.01	0	0.03	11.54	254.04
8	6.39	1.61	8	2.78	0.06	0	3.39	5.02	0.09	0.00	0.02	0.03	11.38	218.56
9	6.43	1.57	8	2.91	0.02	0	3.22	5.03	0.07	0.02	0.02	0.03	11.33	212.93
11	6.02	1.98	8	2.39	0.01	0	3.47	5.80	0.12	0	0	0	11.79	255.30
12	6.08	1.92	8	2.55	0.01	0	3.54	5.44	0.10	0.02	0.01	0.01	11.68	250.54
13	6.11	1.89	8	2.60	0.02	0	3.51	5.41	0.07	0.01	0	0.02	11.64	247.39
14	6.20	1.80	8	2.67	0.02	0.01	3.39	5.35	0.07	0.02	0.02	0.01	11.56	237.10
15	6.03	1.97	8	2.56	0.01	0	3.49	5.48	0.13	0.01	0.01	0.01	11.70	256.10
1	6.04	1.96	8	2.40	0.01	0.01	3.50	5.75	0.08	0.01	0	0	11.77	253.59
2	6.08	1.92	8	2.44	0.02	0	3.43	5.75	0.07	0	0	0	11.72	248.84
3	6.05	1.95	8	2.48	0.02	0.02	3.65	5.46	0.07	0.01	0.01	0.01	11.72	254.87
1	5.99	2.01	8	2.95	0	0	4.41	4.00	0.16	0	0	0	11.53	269.67
2	6.04	1.96	8	2.68	0.01	0	2.84	6.07	0.03	0.01	0	0.01	11.64	249.44
3	6.14	1.86	8	2.67	0.01	0	2.74	6.10	0.03	0.01	0.01	0.02	11.60	237.83
4	6.08	1.92	8	2.59	0	0	2.88	6.14	0.04	0.01	0.01	0	11.67	245.45
5	6.08	1.92	8	2.71	0.01	0	2.77	6.06	0.03	0.01	0.01	0.02	11.61	244.74
6	5.67	2.33	8	2.93	0	0	4.04	4.58	0.14	0	0.01	0	11.71	300.25
7	5.74	2.26	8	3.03	0	0	3.73	4.69	0.16	0	0	0	11.61	290.42
8	6.12	1.88	8	2.75	0.01	0	2.67	6.08	0.04	0	0.01	0.01	11.57	239.87
9	5.53	2.47	8	2.62	0.02	0	4.59	4.54	0.13	0.01	0.02	0	11.92	317.18
10	5.73	2.27	8	2.96	0	0	3.98	4.61	0.09	0	0	0	11.65	292.62
AVG	5.93	2.07	8	2.70	0.01	0	3.26	5.60	0.08	0.01	0.01	0.01	11.68	264.72
STDEV	0.23	0.23	0	0.22	0.02	0	0.71	0.97	0.05	0.01	0.01	0.02	0.15	23.64
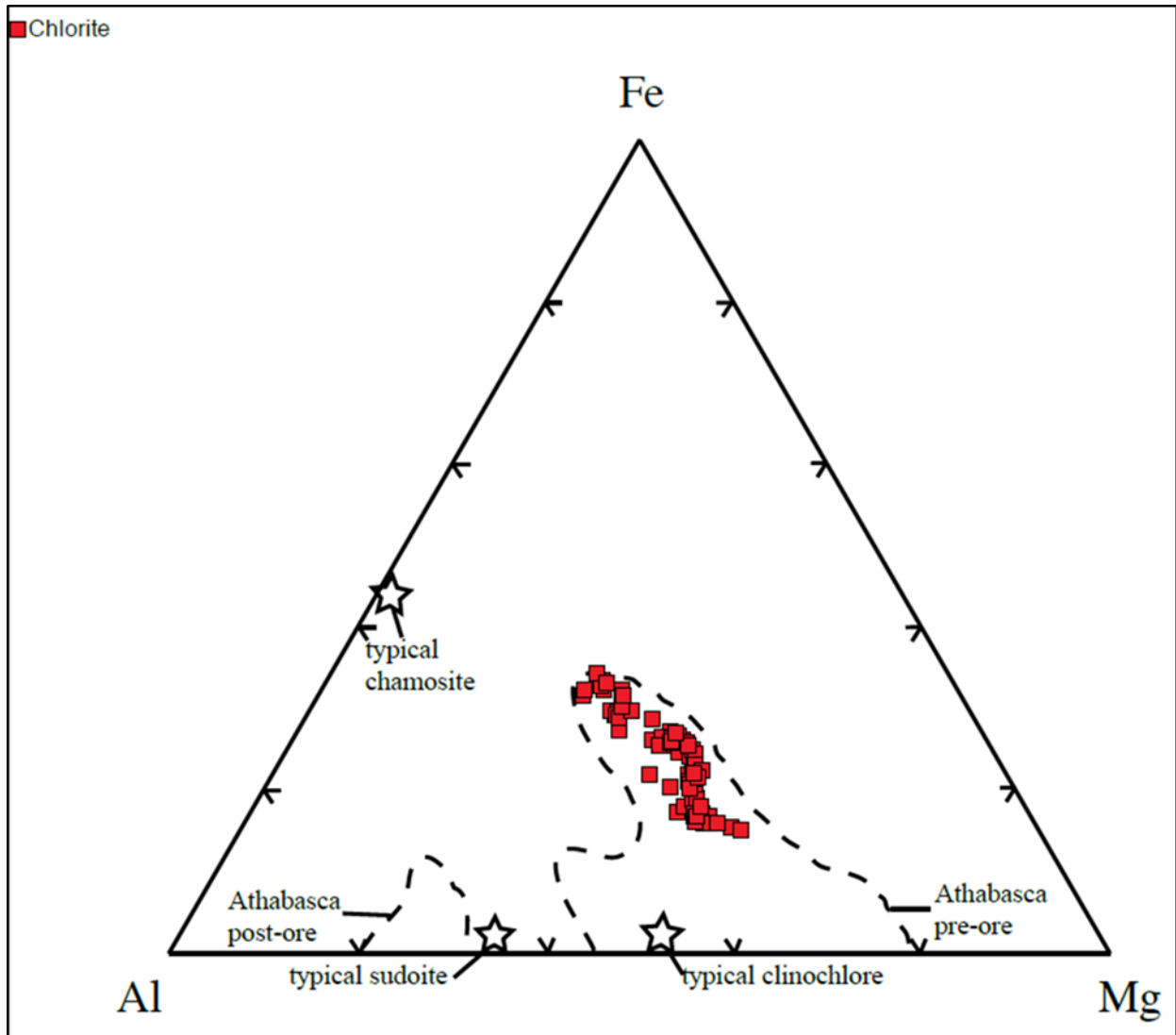
Figure J.1 Al-Mg-Fe ternary diagram for cholorites from altered porphyry samples, plotted as a function of molar proportions. Dashed lines represent the fields of pre-ore and post-ore chlorites from basement-hosted deposits within the Athabasca basin (Alexandre et al., 2005; Cloutier et al., 2009). All chlorites from altered porphyry samples plot within the Athabasca pre-ore field. Typical compositions of chamosite and clinochlore reported by Deer et al. (1992) and sudoite as reported by Lin and Bailey (1985) are plotted. Modified after Beyer et al. (2012).

Table K.1 Composition data of fluorapatites from altered porphyry samples. These analyses represent chemical compositions of fluorapatite rims going along the unconformity.
*compositions expressed as wt.%

Pt#	Si	Th	U	Al	Y	La	Ce	Pr	Nd	Sm	Gd	Dy
1	0	0	0	0	0	0.10	0.09	0	0.03	0	0.12	0
3	0.42	0	0.34	0	0	0.46	0.79	0.10	0.43	0.14	0.08	0
9	0.32	0	0.38	0	0	0.30	0.79	0	0.41	0.07	0.08	0
20	0.25	0	0.46	0	0	0.21	0.57	0.02	0.35	0.12	0.25	0.13
22	0.29	0	0	0	0.06	0.28	0.56	0	0.32	0.14	0.16	0
24	0.24	0	0.50	0	0	0.28	0.63	0	0.17	0.05	0.12	0.03
29	0.32	0	0.65	0	0.18	0.23	0.90	0	0.28	0.29	0.03	0.01
32	0.53	0.05	0	0	0.32	0.30	1.06	0	0.28	0.03	0.13	0
33	0.30	0.22	0.24	0	0.29	0.34	0.69	0.08	0.16	0	0.01	0
37	0.27	0.08	0.24	0	0.09	0.17	0.50	0.08	0.13	0	0.06	0.04
39	0.30	0.07	0.27	0	0.07	0.09	0.75	0.15	0.15	0.02	0.02	0.19
44	0.35	0.01	0.27	0	0.08	0.13	0.72	0.04	0.26	0.03	0.02	0
54	0.26	0	0.50	0	0.13	0.17	0.79	0.17	0.23	0.09	0.12	0
57	0.28	0	0	0	0.21	0.17	0.71	0	0.19	0.09	0.02	0
5	0.67	0	0.22	0	0	0	0	0	0	0	0	0
6	0.04	0	0.24	0	0	0	0	0	0	0	0	0
7	0.35	0.24	0	0	0	0	0	0	0	0	0	0
8	0.35	0.0	0	0	0	0	0	0	0	0	0	0
15	0.37	0.20	0	0	0.28	0.15	0.56	0.34	0.25	0	0	0.02
16	0.03	0.27	0.27	0	0	0.19	0	0	0.16	0	0.08	0
AVG	0.30	0.06	0.23	0.00	0.09	0.18	0.51	0.05	0.19	0.05	0.07	0.02
STDEV	0.15	0.09	0.20	0.00	0.11	0.13	0.35	0.09	0.14	0.07	0.07	0.05

Pt#	Fe	Mg	Mn	Ca	Na	P	F	Cl	O	Total	Notes
1	0.05	0.04	0	37.62	0	18.15	4.1	0.2675	38.56	99.15	9716-1 rim
3	0.35	0	0	36.46	0.16	17.36	3.94	0.5771	37.99	99.61	apatite 2 inner rim
9	0.30	0	0	36.92	0.22	17.81	3.96	1.1442	38.58	101.27	9708A apat #10 rim
20	0.20	0	0.04	35.84	0.27	18.29	3.65	0.8626	38.82	101.21	inner rim
22	0.01	0	0	37.11	0.17	18.22	3.79	0	39	100.13	rim
24	0.23	0	0	38.61	0.13	18.13	3.8	0.9902	39.57	103.98	rim
29	0.20	0.01	0	36.48	0.10	18.13	3.71	0.1233	38.88	100.54	light rim
32	0.04	0.04	0	35.43	0.07	17.59	3.17	0	37.92	96.95	bright rim
33	0.28	0.03	0	35.26	0.11	18.2	3.13	0.1692	38.43	97.95	med rim
37	0.26	0.04	0	35.37	0.10	18.3	3.35	0.1788	38.43	97.7	inner rim
39	0.26	0.04	0.02	36.02	0.11	18.24	3.39	0.0608	38.71	98.94	inner rim
44	0.17	0.04	0	36.91	0.08	17.29	3.34	0.0822	37.83	97.65	rim
54	0.25	0.02	0	36.72	0.10	15.06	3.49	0.0178	34.89	93.01	med rim
57	0.17	0.03	0	36.43	0.08	18.39	3.59	0.0802	38.96	99.4	light rim
5	0.11	0	0.02	38.31	0.02	17.81	4.1	0.3958	39.13	100.77	#5 rim
6	0.13	0	0.02	38.83	0	18.46	3.9	0.3956	39.47	101.51	#6 rim
7	0.28	0	0	37.34	0	14.62	2.257	0.0967	34.29	89.47	#7 rim
8	0.28	0	0	37.38	0	17.86	2.2416	0.0978	38.46	96.66	#7 rim
15	0.34	0.06	0	37.66	0.01	17.67	3.88	0.155	38.74	100.69	inner rim
16	0.15	0	0.01	38.75	0.07	18.39	3.16	0	39.46	100.96	outer rim
AVG	0.20	0.02	0.01	36.97	0.09	17.70	3.50	0.285	38.306	98.88	
STDEV	0.10	0.02	0.01	1.11	0.08	1.04	0.52	0.345	1.363	3.21	

Table K.2 Composition data of fluorapatites from altered porphyry samples. These analyses represent chemical compositions of fluorapatite cores going along the unconformity.
*compositions expressed as wt.%

Pt#	Si	Th	U	Al	Y	La	Ce	Pr	Nd	Sm	Gd	Dy
2	0.22	0	0.31	0	0	0.32	0.77	0	0.38	0	0.09	0
4	0.29	0	0.25	0	0	0.28	0.75	0.12	0.40	0	0.08	0
6	0.26	0	0.35	0	0	0.27	0.52	0.16	0.36	0	0.07	0
7	0.14	0	0.03	0	0	0.13	0.58	0.16	0.28	0.04	0.16	0
8	0.13	0	0	0	0.24	0.21	0.45	0.21	0.21	0.05	0.17	0
10	0.11	0	0.26	0	0	0.10	0.47	0.12	0.15	0	0.12	0.12
11	0.22	0	0.30	0	0.18	0.26	0.57	0.12	0.19	0.01	0.05	0.05
15	0.22	0	0	0	0.09	0.12	0.42	0.14	0.16	0.13	0.01	0
18	0.26	0	0.37	0	0.09	0.29	0.52	0.18	0.31	0.03	0.18	0.05
19	0.23	0	0.33	0	0.20	0.10	0.62	0	0.36	0.06	0.27	0.09
21	0.03	0	0.25	0	0	0.16	0.31	0.01	0.32	0.02	0.11	0
23	0.01	0	0.35	0	0	0.33	0.29	0.28	0.15	0	0.01	0.03
25	0.07	0	0.60	0	0	0.31	0.39	0	0.40	0.07	0.16	0.01
28	0.50	0	0.29	0.17	0.01	0.13	0.72	0.06	0.37	0.01	0.01	0.05
31	0.12	0	0.35	0	0.03	0.02	0.28	0.10	0.20	0.01	0	0.08
36	0.45	0	0.26	0	0.32	0.36	0.75	0.03	0.43	0.09	0.09	0.21
38	0.16	0	0.33	0	0.10	0.17	0.36	0.01	0.26	0.00	0.10	0.17
40	0.34	0.06	0.08	0.01	0.29	0.26	0.60	0.07	0.29	0.18	0.12	0
41	0.33	0	0.3	0	0.12	0.21	0.72	0	0.28	0.04	0	0.15
43	0.28	0	0.44	0	0.01	0.24	0.73	0.04	0.12	0.10	0.14	0
48	0.27	0	0.27	0.01	0.06	0.21	0.38	0.08	0.12	0	0.09	0.15
49	0.45	0	0.60	0.11	0	0.14	0.60	0.27	0.32	0.05	0.03	0.00
52	0.18	0	0.49	0	0.07	0	0.34	0.20	0.26	0.00	0	0.07
53	0.48	0.14	0.16	0	0.07	0.29	0.93	0.02	0.44	0.16	0	0.07
55	0.33	0	0	0	0	0.29	0.78	0.20	0.38	0.02	0.02	0
56	0.16	0.00	0.41	0	0.12	0.16	0.47	0	0.10	0.12	0.05	0.03
9	0.11	0	0.07	0.08	0.38	0	0.01	0	0.00	0	0	0.02
13	1.26	0.11	0.42	0.74	0.42	0.25	1.96	0.35	0.93	0.19	0	0
14	0.38	0.39	0.31	0	0.23	0.24	0.90	0.25	0.36	0.10	0.06	0
AVG	0.28	0.03	0.28	0.04	0.10	0.20	0.59	0.11	0.30	0.05	0.08	0.05
STDEV	0.23	0.08	0.16	0.14	0.13	0.10	0.34	0.10	0.17	0.06	0.07	0.06

Pt#	Fe	Mg	Mn	Ca	Na	P	F	Cl	O	Total	Notes
2	0.30	0.02	0.04	37.41	0.21	17.84	3.95	0.33	38.71	100.89	core
4	0.26	0	0.02	37.21	0.19	17.99	3.79	0.47	38.97	100.97	core
6	0.30	0	0.02	37.15	0.18	17.82	3.59	0.38	38.58	100.02	apatite 4 core
7	0.37	0	0.01	38.33	0.12	18.43	3.87	0.44	39.65	102.75	apatite 6 core
8	0	0	0.04	38.66	0.24	18.18	3.94	0	39.43	102.16	apatite 7 core
10	0.26	0	0.02	36.70	0.18	17.75	3.93	1.01	38.04	99.34	core
11	0.33	0	0.03	36.57	0.23	17.43	3.87	0.88	37.84	99.14	apatite 13 core
15	0.12	0.09	0	36.44	0.00	17.9	3.67	0.04	38.19	97.74	apatite 15 dk core
18	0.25	0	0	38.59	0.19	17.93	3.43	0.82	39.38	103.31	apatite 18 med core
19	0.20	0	0.02	37.28	0.20	18.12	3.5	0.87	39.14	102.47	9705A-1-1 core
21	0.27	0	0.04	38.82	0.19	18.54	3.71	1.40	39.98	105.46	apatite 21 core
23	0.26	0	0.03	38.27	0.16	18.61	3.65	1.86	39.82	104.99	apatite 22 core
25	0.17	0	0.03	36.15	0.19	18.51	3.28	0.46	38.85	99.67	apatite 24 core
28	0.08	0.01	0	36.39	0.10	17.98	3.7	0.18	38.8	99.56	apatite 28 core
31	0.27	0.01	0.04	37.04	0.14	18.29	3.14	0.30	38.86	99.29	apat 36 core
36	0.27	0.04	0	35.07	0.11	18.11	3.43	0.20	38.49	98.75	apatite 41 core
38	0.24	0.04	0.02	35.19	0.10	18.85	3.19	0.10	38.95	98.35	apatite 42 core
40	0.20	0.04	0	37.95	0.08	15.18	3.54	0.24	35.6	95.13	9708B ap 44 core
41	0.24	0.03	0	36.23	0.10	18.09	3.62	0.07	38.64	99.17	apatite 45 lt core
43	0.23	0.05	0	36.25	0.09	17.69	3.55	0.27	38.06	98.3	apatite 47 core
48	0.12	0.01	0	36.41	0.04	18.24	3.64	0.18	38.67	98.96	dark core
49	0.30	0.01	0	34.55	0.08	18.11	3.79	0.01	38.25	97.68	9716 II ap 54 core
52	0.20	0.03	0.05	36.03	0.13	18.39	3.59	0.25	38.7	98.98	apatite 58 dk core
53	0.21	0.03	0	34.73	0.10	15.41	3.32	0.23	34.8	91.58	apatite 59 lt core
55	0.20	0.04	0	35.03	0.14	14.67	3.43	0.21	33.72	89.47	apatite 60 lt core
56	0.12	0.02	0	37.30	0.10	17.84	3.65	0.17	38.43	99.24	apatite 61 dk core
9	0.09	0.05	0	37.65	0.10	18.62	3.92	0	39.47	100.55	#8 inner core
13	0.44	0.04	0	33.25	0.14	11.98	3.69	0.15	31.85	88.18	9716-1 apatite 8 core
14	0.19	0.03	0	31.94	0.09	17.82	3.03	0.14	36.78	93.23	outer core
AVG	0.22	0.02	0.01	36.50	0.13	17.60	3.60	0.40	38.09	98.80	
STDEV	0.09	0.02	0.02	1.61	0.06	1.47	0.25	0.44	1.87	4.05	

Table K.3 Composition data of fluorapatites from altered porphyry samples. These analyses represent bulk chemical compositions of fluorapatites going along the unconformity.
*compositions expressed as wt.%

Pt#	Si	Th	U	Al	Y	La	Ce	Pr	Nd	Sm	Gd	Dy
5	0.29	0	0.43	0	0.00	0.11	0.76	0.04	0.42	0.15	0.00	0.03
12	0.32	0	0.16	0	0.00	0.30	0.74	0.05	0.34	0.14	0.08	0.03
13	0.32	0	0	0	0.00	0.30	0.74	0.05	0.34	0.14	0.08	0.03
16	0.29	0	0.39	0	0.11	0.17	0.66	0	0.41	0.14	0.29	0.16
27	0.10	0	0.40	0	0.08	0.20	0.34	0	0.25	0.08	0.10	0.02
34	0.22	0	0.42	0	0.16	0.22	0.45	0	0.22	0.07	0.14	0.12
35	0.37	0.21	0.29	0	0.11	0.17	0.82	0	0.29	0	0.03	0.24
45	0.34	0	0.47	0	0.13	0.27	0.52	0	0.23	0.03	0.05	0
46	0.33	0	0.26	0	0.20	0.26	0.75	0.07	0.53	0.08	0.03	0.12
50	0.04	0.10	0.18	0	0.04	0.11	0.28	0.04	0.09	0.02	0	0
51	0.27	0	0.66	0	0.01	0.11	0.67	0	0.26	0.12	0.04	0.19
AVG	0.26	0.03	0.33	0	0.08	0.20	0.61	0.02	0.31	0.09	0.08	0.09
STDEV	0.10	0.07	0.18	0	0.07	0.07	0.18	0.03	0.12	0.05	0.08	0.08

Pt#	Fe	Mg	Mn	Ca	Na	P	F	Cl	O	Total	Notes
5	0.32	0	0.03	36.87	0.06	17.83	3.42	0.43	38.51	99.7	apatite 3
12	0.21	0	0	36.44	0.29	17.59	4.08	2.11	38.09	100.98	apatite 14
13	0.21	0	0	36.43	0.29	17.58	4.11	2.12	38.06	100.81	apatite 14
16	0.31	0	0.03	37.35	0.20	17.96	3.52	1.03	39.16	102.01	apatite 16
27	0.18	0.02	0.03	36.81	0.16	18.58	3.81	0.18	39.18	100.54	apatite 25
34	0.19	0.03	0	36.01	0.10	18.36	3.19	0.09	38.74	98.73	apatite 37
35	0.28	0.05	0.03	35.83	0.11	18.05	3.5	0.16	38.55	99.09	apatite 39
45	0.15	0.02	0	35.65	0.07	18.33	3.63	0	38.66	98.55	apatite 50
46	0.22	0.03	0	35.95	0.09	18.13	3.76	0.13	38.66	99.6	apatite 51
50	0.20	0.05	0.02	36.77	0.09	17.85	3.61	0.11	38.04	97.63	apatite 56
51	0.24	0.03	0.01	35.30	0.13	18.1	3.8	0.48	38.23	98.65	apatite 57
AVG	0.23	0.02	0.01	36.31	0.14	18.03	3.68	0.62	38.53	99.66	
STDEV	0.05	0.02	0.01	0.62	0.08	0.31	0.275	0.79	0.41	1.30	

Table K.4 Composition data of fluorapatites from altered porphyry samples. These analyses represent chemical compositions of fluorapatites rims going away from the unconformity.
*compositions expressed as wt.%

Pt#	Si	Th	U	Al	Y	La	Ce	Pr	Nd	Sm	Gd	Dy
7	0.11	0.02	0	0	0.01	0	0.13	0	0.11	0.02	0	0
9	0.14	0	0.12	0.04	0.01	0.23	0.31	0.16	0.03	0	0	0
11	0.48	0.06	0.03	0	0.33	0.42	0.98	0	0.58	0.14	0.11	0
14	0.12	0	0	0	0.26	0.32	0.45	0	0.08	0.09	0.11	0
16	0.27	0.01	0	0	0.25	0.27	0.66	0.17	0.38	0.03	0.04	0
18	0.41	0	0.02	0	0.32	0.47	0.80	0.23	0.33	0.02	0	0.02
20	0.30	0	0	0	0.17	0.21	0.78	0.08	0.23	0.06	0.22	0.02
21	0.27	0.03	0	0.01	0.31	0.25	0.88	0.06	0.28	0	0	0
23	0.18	0	0	0.01	0.06	0.19	0.50	0.19	0.12	0.07	0.10	0.15
AVG	0.25	0.01	0.02	0.01	0.19	0.26	0.61	0.10	0.24	0.05	0.06	0.02
STDEV	0.13	0.02	0.04	0.01	0.13	0.14	0.28	0.09	0.17	0.05	0.08	0.05

Pt#	Fe	Mg	Mn	Ca	Na	P	F	Cl	O	Total	Notes
7	0.08	0.01	0.03	40.74	0.03	18	3.95	0.04	39.73	103.01	9726 apatite rim
9	0.09	0	0.06	38.64	0.02	17.08	3.87	0	37.87	98.67	9726 apatite rim
11	0.15	0.04	0	38.6	0.06	17.38	3.89	0.03	38.96	102.22	9726 apatite rim
14	0.21	0	0.06	39.57	0.07	18	3.39	0.02	39.56	102.37	9722 apatite rim
16	0.24	0.05	0.03	38.87	0.05	17.87	3.54	0.05	39.36	102.13	9722 apatite rim
18	0.27	0.06	0	38.74	0.07	17.47	3.42	0.04	39.04	101.74	9722 apatite rim
20	0.33	0.06	0.01	37.87	0.09	16.04	3.32	0.04	36.65	96.49	9722 apatite rim
21	0.30	0.03	0.01	37.86	0.06	17.77	3.89	0.04	38.84	100.88	9722 apatite rim
23	0.30	0.04	0.03	40.75	0.06	17.77	3.35	0.07	39.8	103.73	9722 apatite rim
AVG	0.22	0.04	0.03	39.07	0.06	17.49	3.62	0.04	38.87	101.25	
STDEV	0.09	0.02	0.02	1.08	0.02	0.62	0.27	0.02	1.02	2.29	

Table K.5 Composition data of fluorapatites from altered porphyry samples. These analyses represent chemical compositions of fluorapatites cores going away from the unconformity.

*compositions expressed as wt.%

Pt#	Si	Th	U	Al	Y	La	Ce	Pr	Nd	Sm	Gd	Dy
8	0.34	0	0.05	0	0.22	0.27	0.87	0	0.34	0.05	0.06	0
10	0.12	0.05	0	0	0.15	0.37	0.34	0.04	0.24	0	0.10	0.02
12	0.33	0.02	0.21	0	0.16	0.31	0.89	0.04	0.33	0.17	0.09	0.06
13	0.30	0	0.14	0	0.22	0.22	0.65	0.27	0.32	0.01	0.13	0
15	0.14	0	0.01	0	0.10	0.13	0.70	0.10	0.22	0.08	0	0.05
17	0.17	0.01	0	0	0.16	0.26	0.55	0	0.21	0	0	0
19	0.12	0.03	0.01	0	0.02	0.07	0.39	0	0.12	0.06	0.01	0
22	0.33	0	0.04	0.0	0.14	0.38	0.81	0.19	0.42	0	0.06	0.16
AVG	0.23	0.01	0.06	0	0.15	0.25	0.65	0.08	0.28	0.05	0.06	0.04
STDEV	0.10	0.02	0.08	0	0.06	0.11	0.21	0.10	0.10	0.06	0.05	0.05

Pt#	Fe	Mg	Mn	Ca	Na	P	F	Cl	O	Total	Notes
8	0.25	0.04	0.01	38.18	0.04	17.83	4.1	0.04	39.11	101.83	9726 apatite core
10	0.05	0.05	0.02	38.69	0.10	17.91	3.43	0	39.04	100.74	9726 apatite core
12	0.10	0.06	0.02	39.54	0.05	17.24	3.61	0.03	38.91	102.17	9726 apatite core
13	0.12	0.03	0.01	39.24	0.08	16.77	3.67	0.03	38.09	100.29	9726 apatite core
15	0.20	0.03	0.01	38.22	0.10	16.47	3.55	0.06	37.05	97.22	9722 apatite core
17	0.28	0.04	0.01	39.57	0.08	17.84	3.63	0.05	39.39	102.27	9722 apatite core
19	0.20	0.05	0.04	38.72	0.09	17.92	3.29	0.01	38.98	100.11	9722 apatite core
22	0.26	0.05	0	36.5	0.08	17.59	3.26	0.06	38.19	98.53	9722 apatite core
AVG	0.18	0.04	0.02	38.58	0.08	17.45	3.57	0.03	38.60	100.40	
STDEV	0.08	0.01	0.01	1.00	0.02	0.56	0.26	0.02	0.77	1.79	

Table K.6 Composition data of fluorapatites from altered porphyry samples. These analyses represent bulk chemical compositions of fluorapatites going away from the unconformity.

*compositions expressed as wt.%

Pt#	Si	Th	U	Al	Y	La	Ce	Pr	Nd	Sm	Gd	Dy
3	0.30	0	0.01	0	0.11	0.27	0.77	0.13	0.49	0.05	0.11	0.11
4	0.35	0	0	0	0.25	0.34	0.81	0	0.48	0.16	0	0.08
5	0.29	0.04	0	0	0.25	0.13	0.78	0.10	0.40	0.07	0.11	0.04
6	0.31	0	0.04	0	0.29	0.48	0.88	0.02	0.47	0.02	0.05	0
AVG	0.31	0.01	0.01	0	0.23	0.30	0.81	0.06	0.46	0.08	0.07	0.06
STDEV	0.02	0.02	0.02	0	0.08	0.15	0.05	0.06	0.04	0.06	0.05	0.05

Pt#	Fe	Mg	Mn	Ca	Na	P	F	Cl	O	Total	Notes
3	0.19	0.02	0.06	38.65	0.07	17.7	3.91	0.05	39.09	102.1	9726 apatite
4	0.07	0.04	0.04	37.56	0.07	16.81	3.45	0.02	37.55	98.07	9726 apatite
5	0.09	0.01	0	39.58	0.02	18	3.63	0	39.77	103.33	9726 apatite
6	0.12	0.01	0.02	39.83	0.07	14.16	3.62	0.01	35.02	95.43	9726 apatite
AVG	0.12	0.02	0.03	38.91	0.06	16.67	3.65	0.02	37.858	99.73	
STDEV	0.05	0.01	0.03	1.03	0.03	1.75	0.19	0.02	2.107	3.64	

APPENDIX L

Table L.1 Chemical composition data of Fe oxide from altered porphyry samples.
*compositions expressed as wt.%

Pt#	Si	Ti	Th	U	Al	Y	La	Ce	Pr	Nd
3	0.04	0.01	0	0	0	0.01	0	0.01	0	0
4	0.03	0.02	0.00	0	0.01	0.01	0	0.02	0.04	0.08
5	0.02	0	0.02	0	0.02	0	0	0.06	0	0
11	0.03	0	0	0	0.01	0.03	0.07	0.03	0.03	0.01
AVG	0.03	0.01	0.00	0.00	0.01	0.01	0.02	0.03	0.02	0.02
STDEV	0.01	0.01	0.01	0.00	0.01	0.01	0.03	0.02	0.02	0.04

Pt#	Sm	Gd	Dy	Fe	Mg	Mn	O	Total	Notes
3	0.00	0.13	0.03	73.11	0	0.00	21.03	94.38	9722 Fe oxide
4	0.01	0.05	0	72.72	0.01	0.05	20.94	93.99	9722 Fe oxide
5	0	0	0	73.86	0	0.01	21.21	95.2	9722 Fe oxide
11	0	0.03	0	76.15	0	0.01	21.9	98.29	9722 Fe oxide
AVG	0.00	0.05	0.01	73.96	0.00	0.02	21.27	95.47	
STDEV	0.01	0.06	0.02	1.53	0.00	0.02	0.43	1.95	

Table L.2 Chemical composition data of Ti oxide from altered porphyry samples.
*compositions expressed as wt.%

Pt#	Si	Ti	Th	U	Al	Y	La	Ce	Pr	Nd
8	0.07	56.6	0.02	0.05	0.00	0.02	0	0	0	0.02
9	0	56.48	0.02	0	0.01	0.01	0	0	0	0.10
10	0.01	57.94	0.03	0	0	0.01	0.06	0	0	0.08
15	0.22	55.4	0.06	0	0.04	0	0.03	0	0	0.13
16	0.03	56.92	0.01	0.07	0.01	0.13	0.14	0	0	0.03
17	0.09	57.62	0	0.05	0.01	0.13	0.05	0	0	0
18	0.03	58.9	0	0.03	0.01	0	0	0	0.10	0.09
19	0.04	57.54	0	0.01	0	0	0	0	0.05	0
20	0.08	57.75	0	0.01	0.05	0.08	0.04	0	0	0.01
21	0	59.17	0.01	0	0.00	0	0.03	0	0	0.04
AVG	0.06	57.43	0.01	0.02	0.01	0.04	0.04	0.00	0.02	0.05
STDEV	0.07	1.13	0.02	0.03	0.02	0.05	0.04	0.00	0.04	0.05

Pt#	Sm	Gd	Dy	Fe	Mg	Mn	O	Total	Notes
8	0.12	0	0	2.08	0.00	0.00	38.53	97.53	9722 Ti oxide
9	0	0	0	0.89	0.01	0	38.02	95.54	9722 Ti oxide
10	0	0.04	0	0.69	0.01	0.02	38.96	97.86	9722 Ti oxide
15	0.01	0	0.02	1.07	0	0.01	37.65	94.65	9726 Ti oxide
16	0.09	0	0	0.53	0	0	38.3	96.25	9726 Ti oxide
17	0.03	0.02	0	0.46	0.00	0	38.8	97.27	9726 Ti oxide
18	0	0	0	0.23	0.01	0.01	39.5	98.89	9726 Ti oxide
19	0	0.00	0.07	0.46	0.00	0	38.64	96.82	9726 Ti oxide
20	0	0	0	0.43	0.04	0.02	38.9	97.41	9726 Ti oxide
21	0.12	0	0.08	0.40	0.00	0.01	39.69	99.56	9726 Ti oxide
AVG	0.04	0.01	0.02	0.72	0.01	0.01	38.70	97.18	
STDEV	0.05	0.01	0.03	0.54	0.01	0.01	0.62	1.47	

Table L.3 Chemical composition data of Fe-Ti oxide from altered porphyry samples.
*compositions expressed as wt.%

Pt#	Si	Ti	Th	U	Al	Y	La	Ce	Pr	Nd
7	0.05	1.54	0	0	0.03	0.09	0.03	0	0.08	0.00
12	0.02	4.62	0.02	0	0.01	0	0.02	0	0	0
13	0.10	2.48	0.01	0	0.06	0	0	0	0	0.02
14	0.05	5.47	0.01	0	0.03	0	0.03	0	0.03	0.02
6	0.05	2.42	0.02	0	0.00	0	0	0	0	0
AVG	0.06	3.31	0.01	0.00	0.03	0.02	0.02	0.00	0.02	0.01
STDEV	0.03	1.66	0.01	0.00	0.02	0.04	0.02	0.00	0.04	0.01

Pt#	Sm	Gd	Dy	Fe	Mg	Mn	O	Total	Notes
7	0	0	0	72.51	0.01	0.02	21.94	96.32	9722 Fe/Ti oxide
12	0	0	0	71.73	0	0	23.68	100.11	9722 Fe/Ti oxide
13	0	0	0.06	73.56	0.05	0.01	22.95	99.32	9722 Fe/Ti oxide
14	0.09	0.05	0	69.5	0.00	0	23.68	98.97	9722 Fe/Ti oxide
6	0.018	0.04	0	70.92	0	0.03	22.02	95.52	9722 Fe/Ti oxide
AVG	0.02	0.02	0.01	71.64	0.01	0.01	22.85	98.05	
STDEV	0.04	0.03	0.03	1.55	0.02	0.01	0.85	2.01	